Piezoresistive cantilevers with an integrated bimorph actuator

by

Tzvetan Ivanov

A dissertation submitted in partial fulfillment of
requirements for the degree of

Doctor of Philosophy
(Dr. rer. nat.)

Physics Department
of University Kassel
2004

Gedruckt mit Genehmigung des Fachbereichs Physik der
Universität Kassel

Betreuer der Arbeit: Prof. Dr. R. Kassing

Erstgutachter: Prof. Dr. R. Kassing
Zweitgutachter: Prof. Dr. K. Röll

Weitere Mitglieder der Prüfungskommission:

Prof. Dr. B. Fricke
Prof. Dr. R. Matzdorf

Tag der Disputation: 04 März 2004

Contents

Contents I

Chapter 1 Introduction 1

Chapter 2 Characteristic of the piezoresistive medium 7

2.1 Strain and stress tensors 7
2.2 Resistive and piezoresistive tensors 10
2.3 Simplification by crystal symmetry 11
2.4 Coordinate transformation of the coefficients in matrix notation 12

Chapter 3 Quantum mechanical background 15

3.1 Electrons in a perfect crystal 16
3.2 Approximations 16
3.3 Band structure in the presence of strain 18
3.4 Spin-orbit interaction 20
3.5 Crystal symmetry of the Silicon 21

Chapter 4 Calculation of the piezoresistive effect for the bulk piezoresistors-3D case 25

4.1 Conduction band structure-piezoresistive coefficients 26
4.2 Valence band structure - piezoresistive coefficients 29
4.3 Piezoresistive coefficients as a function of temperature and concentration 37

Chapter 5 Piezoresistive effect in quantum wells 41

5.1 Quantum confinement - 2D electron gas 41
5.2 Quantum confinement effect - 2D hole gas 44

Chapter 6 Thermo-Mechanical analysis of the cantilever beams 51

6.1 Quasi - Statical Beam deflection under axial and transverse load 52
6.2 Structural dynamics of the cantilever beam 56
6.3 Multi-modes analysis of the periodic force driven cantilever with damping 66
6.4 Multi-layer cantilever beam with an embedded thermal actuator 71

6.5 Analysis of the thermal actuators 77
6.6 Analysis of the piezoresistive sensor 84
Chapter 7 Fundamental limitation of sensitivity by Noise 88
7.1 Introduction and basic mathematical methods 88
7.2 Thermal Noise 90
7.3 Energy dissipation 92
7.3.1 Air damping 93
7.3.2 Clamping losses 94
7.3.3 Thermoelastic losses 95
7.3.4 Losses connected with the surface 97
7.4 Piezoresistor detection noise 97
7.4.1 Johnson noise 98
7.4.2 1/f noise 99
7.5 Force resolution optimisation 100
Chapter 8 Fabrication process and applications of the cantilever-based sensors 104
8.1 Fabrication process 104
8.2 Cantilever beam with porous silicon element as a sensor 107
8.3 Cantilever beam for high speed AFM in higher eigenmodes 109
8.4 Piezoresistive cantilever as a tool for maskless lithography 113
Conclusions 115
Appendix 121
References 123
List of patents and publications 128
Curriculum vitae 131

Chapter 1
Introduction

The nanotechnology age started with the famous talk ″There′s plenty of room at the bottom: an invitation to enter a new field of physics″ [1] given by Nobel prizewinner Richard Feynman. In this talk Feyman was inspired to explore the nano world of the material structure.

Scanning proximity probes (SPP) are uniquely powerful tools for analysis, manipulation and bottom-up synthesis. They are capable of addressing and engineering surface applications at the atomic level and they are the key for unlocking the full potential of nanotechnology.

Microsized cantilevers as instruments used in nanotechnology earned their claim to fame with the invention of the atomic force microscopy (AFM). The AFM was originally described by Binnig and co-workers [2] as an offspring of the scanning tunnelling microscope (STM) [3].

The following rapid development of scanning probe microscopes (SPM) derives directly from the principles of achieving extraordinary lateral resolution through a precise position of the probe. Additionally, the SPM family of microscope techniques are based on these principles, such as AFM, STM, Scanning Thermal Microscopy (SThM), Friction Force Microscopy (FFM), Magnetic Force Microscopy (MFM) and Scanning Near-Field Optical Microscopy (SNOM). *Figure 1.1* shows a picture of a typical laser beam detection system used in AFMs.

Scanning force microscopy (SFM) as the most widely used variant of the SPP methods exhibited a strikingly successful evolution over the past ten years. This has been based primarily on the development of cantilever sensors for the detection of physical quantities, such as mechanical, magnetic and thermal transport properties, as well as

chemical and biological reactions. Using the SPP in AFM mode, it is possible to image molecules and to measure elastic properties of single molecules in a wide range of environments ranging from ultra high vacuum to liquid. Doing AFM in biological applications for example, it is essential to reduce the acting forces on the sample, such as a DNA molecule, to prevent damage.

Besides their wide-spread use in SPPs, where the connection between the probe and sample is realized at a single point (the tip), microcantilevers have recently been used as sensors for measuring extremely small bending moments that are produced by thermally or chemically generated stresses over the whole cantilever surface. Working on such principles, the advancement of the microcantilever beams as ultra-sensitive force sensors increase enormously.

Today microcantilever based sensors are irreplaceable in many different scientific fields such as visualization and measurement of different physical quantities in the nanoscale range, as well as for such applications as information science, microfabrication, quality control, nano-science technology and biological research.

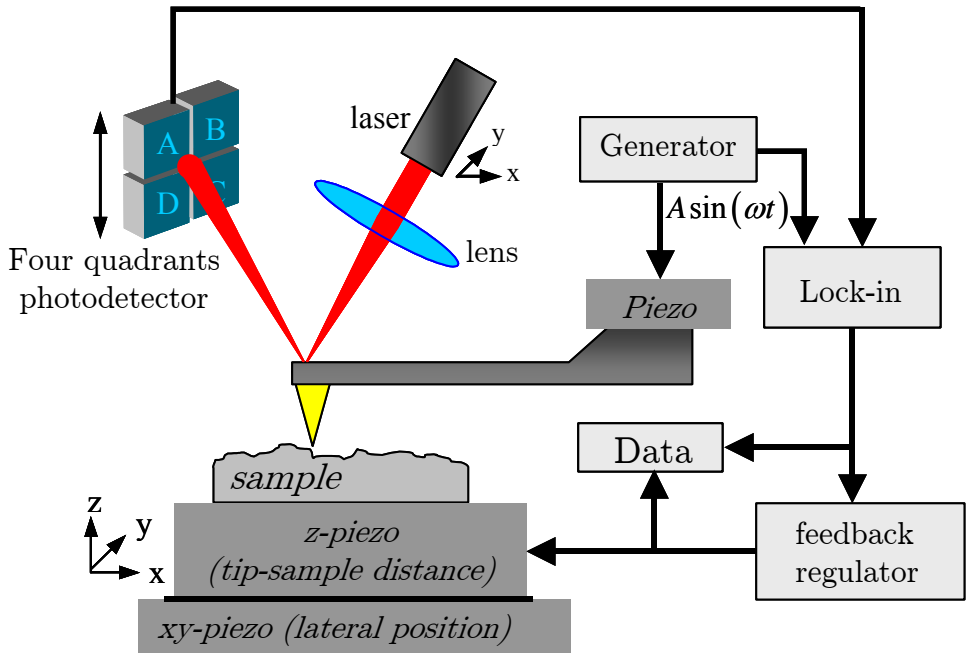

Figure 1.1 Schematic diagram of the components in an AFM laser beam deflection system.

The AFM detection principle is based on the deflection of the cantilever beam. Therefore one of the major tasks is to precisely measure small deflections. In the most exploited deflection measurement scheme [4], the cantilever deflection is measured by detecting the relative displacement of a laser beam reflected off the back of the cantilever. As an alternative to such an optical detection method of the cantilever deflection, the development of cantilevers integrated with piezoresistive displacement detection sensors [5] has resulted in a remarkable improvement of their capability in terms of applicability and ease of implementation. The sensing element or transducer is a piezoresistor embedded in the arms of the cantilever. The change of the piezoresistor resistance, which is caused by the stresses due to the cantilever bending, can be easily converted into an electrical signal suitable for measurement. These piezoresistive cantilevers are much more suited for operation in higher resonance modes compared to optical detection schemes, which require laser beam alignment and monitoring the deflection with a laser spot at different locations along the cantilever in order to avoid the vibration nodes.

This scheme of a high sensitivity, low force cantilever system, which is capable of ultra high frequency response has resulted in the development at the California Institute of Technology (CalTech) of a mechanical beam resonator with a fundamental resonance frequency of 70.72 MHz and a quality factor of $2x10^4$, fabricated using common silicon IC technology [6]. Such devices have the potential to provide new classes of particle and energy sensors due to their very small dimensions and mass, consequently high operating frequencies, and sensitivity to external conditions. For example, a resonator with a fundamental mechanical resonance frequency in order of 1GHz could sense quantum effects and interact with thermal phonons having the same range of frequencies. The CalTech's team device has the ability to detect forces ~ 10^{-18} N, at a central frequency of 1.0156MHz corresponding to a higher vibration eigenmode of the structure. This is below the intrinsic noise level corresponding to a minimum detectable force of $48x10^{-18}$ N with a bandwidth of 80 Hz [7].

Microcantilevers are also useful when portable, low cost individual sensors are required. Researchers at the Oak Ridge National Laboratory [8] had developed measurement sensors for humidity, mass, heat and chemical reactions based on microcantilevers. For example, the heat detected in a bimorph structure causing a bending, while mass

changes affect the resonant frequency. For portability and ease of use, laser detection should be avoided. These types of measurements can potentially be combined in an array of sensors to create an electronic nose. The advantages of the piezoresistive readout system over the cumbersome conventional laser readout principle for sensor-actuator arrays are obvious and they herald the possibility of generic massively parallel SPP systems. They must, however, be able to achieve the same deflection sensitivity as the laser deflection method.

The fundamental key to advance the capability of the SPM techniques is to improve the force (for static or DC-mode force microscopy) and force gradient (for dynamic or AC-mode force microscopy) sensitivity of the micro-fabricated cantilever. Small force measurements, for example, are needed for biology applications, where they are important for measuring antibody-antigen binding (100pN [9]) and protein folding (0.1-100pN [10]). Ultrasensitive cantilevers are required for the Magnetic Resonance Force Microscopy (MRFM), where the forces below the attonewton have to be measured [11]. The ultimate sensitivity of the force and force gradient measurements are restricted by the thermal excitation noise of the micro-cantilever, which can be determined from the fluctuation-dissipation theorem (FDT). This theorem has been established by Callen et.al [12 , 13 , 14 , 15], who predicts the relationship between the spectrum of the thermal noise and the dissipation of systems. The obtained results for the minimum detection force [16] and minimum detection force gradient [17] give us the blueprint conditions for the design of ultrasensitive cantilevers. Such cantilevers have to be maximally soft at the maximal bandwidth. The only way to meet the requirements of both conditions is to make thinner, narrower as and longer cantilevers. Therefore, cantilever sensors with extremely high sensitivity can be fabricated by simply reducing the cantilever dimensions. The basic idea of this design optimisation is to decrease the cantilever thickness below 100nm, which dictates a reduction of the integrated piezoresistor thickness below 50nm [18]. The physical consequence of this thin piezoresistor is the confinement of the charge carriers in the direction perpendicular to the cantilever surface. As it is well known from the quantum mechanics, below this boundary the quantum confinement begins to have significant influence on the electrical properties of the resistor.

At the moment the dominant mode of AFM imaging has become intermittent contact mode, or tapping mode (TM-AFM), firstly introduced by Zhong *et al.* [19]. The advantages of this technique is that it reduces lateral forces between the tip and sample [20]. However, the scan speed of current TM-AFM's is limited to about 250 μm/s due to the actuation time constant of the piezotube feedback loop that keeps the tapping amplitude constant. This limitation can be overcome by reducing the size of the system and consequently its inertia. In this manner it is possible to increase the scanning speed significantly. Furthermore, by increasing the sensitivity of the tapping probe the signal to noise ratio can be improved, thus leading to a further reduction in the time constant needed for stable feed-back loop operation. Consequently, to the integration of the detecting piezoresistive sensor, actuator integration into the cantilever has to be considered as fundamental for the realisation of fast, high-resolution imaging. For signal conversion from the electrical to the mechanical domain, it is necessary to add conversion elements compatible with CMOS processing, using thin film technology. Signal conversion by electrostatic forces has been demonstrated [21]. However, electrostatic forces are normally only significant for small separation of the plates because electro-statically driven cantilevers are based on electrostatic forces that are proportional to the square of the separation of the cantilever plates. The main advantages of electro-statically driven cantilevers are low power consumption and short actuation-times. Piezoelectric actuators based on sputtered ZnO films have been successfully used to excite mechanical vibration in micromachined cantilevers for AFM applications [22]. The micro-actuators described in this work are based on the so-called bimetal effect [23]. The actuator consists of a sandwich of layers, namely Al, SiO_2 and Si. The aluminium layer forms the heating micro-resistor and is used as the driving element.

The main objective of the work described in this thesis is to enable the construction of cantilevers with piezoresistive readout and to integrate bimorph actuators. The thesis focuses its efforts on the design and the determination of the physical limit of piezoresitive cantilevers with an embedded actuator needed for developing of ultimate sensitive force sensors for advanced measurement techniques for nano-science, including physical, chemical and biological applications. To achieve these goals the thesis draws

on areas such as theoretical physics, numerical simulations, noise characterization and micro mechanical technology. The organization of this thesis is based on the following 8 chapters:

- The current chapter presents the background and motivation for this work, and outlines the thesis organization.
- Chapter 2 provides the basic definitions needed for a macroscopic description of the piezoresistive effect.
- Chapter 3 gives an outline of the effective mass method (**kp** approximation), used to construct energy bands and wave functions near the conduction and valence band edges in semiconductors. The effects of strain on the band structure will be reviewed and the necessary corrections to the effective Hamiltonian will be presented.
- Chapter 4 deals in detail with issue regarding the piezoresistive effect in both n and p-type bulk silicon.
- Chapter 5 discusses the way to extend the applicability of existing piezoresistive models by incorporating new physical effects that arise due to the scaling of the piezoresistors thickness and energy band modification in case of 2D.
- Chapter 6 considers the fundamental equations for the mechanical characteristics of the cantilever beam. It is necessary to make this analysis, because the cantilever sensors transform the investigated force into a mechanical deflection. In addition the principles of the thermal bimorph actuations of the cantilever beam will be discussed as well.
- Chapter 7 discusses the fundamental limits for the sensitivity of the piezo-cantilever beam with an integrated bimorph actuator with respect to the noise and actuator-sensor crosstalk. As, the noise is connected with the energy dissipation (according to the fluctuation dissipation theorem), the different mechanisms of energy dissipation will be discussed.
- Chapter 8 focuses on several questions during device fabrication and gives examples of cantilever based sensors and their applications.
- Finally the thesis finishes with a summary and conclusions of this research.

Chapter 2
Characteristic of the piezoresistive medium

The piezoresistive effect of semiconductors describes how the resistivity is influenced by mechanical stress. For the phenomenological description of the piezoresistive effect elastic (stress or strain) and electrical (electrical filed) quantities are necessary.

2.1 Strain and stress tensors

For the definition of the elastic quantities, it is necessary to give a brief review of continuum mechanics theory.

Stress is the distribution of internal body forces of varying intensity due to externally applied forces and/or heat. The intensity is represented as the force per unit area of surface on which the force acts. To illustrate this concept, consider an arbitrary continuous and homogeneous body. Around an arbitrary point in the continuous body we define an elementary volume with cubic form. The planes of this volume are normal to the coordinate directions ($x \equiv 1,\ y \equiv 2,\ z \equiv 3$). The stress in such a point is presented by a stress tensor $\mathbf{T}$ of rank two. Due to the mechanical equilibrium conditions of the infinitesimal cubic element the stress tensor can be written as a symmetrical matrix:

$$\mathbf{T} = \begin{pmatrix} T_{11} & T_{12} & T_{13} \\ T_{21} & T_{22} & T_{23} \\ T_{31} & T_{32} & T_{33} \end{pmatrix}. \qquad (2\text{-}1)$$

In the definition above, T_{ii} are the normal stress components, which act on the faces perpendicular to the $i-$direction. In addition, T_{ij} are the shear stress components oriented in $j-$direction and acting on the faces with normal in the $i-$direction.
The deformation of a body around the same point is characterized by the components of the strain tensor $\mathbf{S}$. Strain is a dimensionless quantity, which represents the state of deformation in a solid body. In the one-dimensional case for any point of a crystal, the strain can be defined as a ratio between the deformation δu and length of the segment δx, given by the following relationship:

$$\lim_{\delta x \to 0} \frac{\delta u}{\delta x} = \frac{\partial u}{\partial x}. \tag{2-2}$$

To expand this definition to the three-dimension case, let us consider a solid, which differs from a perfect crystal in that the atoms are displaced from their equilibrium positions $\mathbf{x}$ by a small amount $\mathbf{u}$. In elastic theory one is interested in how the displacements *change* in space. The deformation $\Delta\mathbf{u}$ of the segment between points $\mathbf{x}$ and $\mathbf{x}+\Delta\mathbf{x}$ can be expressed as:

$$\Delta u_i = \frac{\partial u_i}{\partial x_j}\Delta x_j \quad where \quad i, j = 1, 2, 3. \tag{2-3}$$

The second rank tensor $\partial u_i / \partial x_j$, which appears in the above equation, can be decomposed into symmetric and anti-symmetric tensors:

$$\frac{\partial u_i}{\partial x_j} = \left(\frac{\partial u_i}{\partial x_j}\right)^s + \left(\frac{\partial u_i}{\partial x_j}\right)^a = \frac{1}{2}\left(\frac{\partial u_i}{\partial x_j} + \frac{\partial u_j}{\partial x_i}\right) + \frac{1}{2}\left(\frac{\partial u_i}{\partial x_j} - \frac{\partial u_j}{\partial x_i}\right). \tag{2-4}$$

The anti-symmetric part is associated with a *rotation* of the whole crystal and there is no elastic energy associated with a pure rotation. Therefore, it is more convenient to define the strain tensor as the symmetrical part of the deformation tensor:

$$\mathbf{S} = \begin{pmatrix} S_{11} & S_{12} & S_{13} \\ S_{21} & S_{22} & S_{23} \\ S_{31} & S_{32} & S_{33} \end{pmatrix} \quad where \quad S_{ij} = \frac{\partial u_i}{\partial x_j} + \frac{\partial u_j}{\partial x_i} \quad for \quad i, j = 1, 2, 3 \tag{2-5}$$

The diagonal elements S_{11}, S_{22} *and* S_{33} represent the normal strains. They are defined as the change in length per unit length in the line segment in the direction under consideration. The shear strains S_{12}, S_{23} *and* S_{13} are defined as the tangent of the change in the angle between segments whose original directions were i *and* j. For small angle changes the tangent length is nearly equal to the angle change in radians. Therefore we associate the off-diagonal elements S_{12} S_{21} S_{13} S_{31} S_{23} *and* S_{32} with the shear strains.

Consider a solid that is weakly deformed by external forces, which are represented by the stress tensor (2-1). In this case, the stress and strain tensors are related by Hooke's law, which states that the stress tensor is linearly proportional to the strain tensor:

$$\begin{aligned} T_{ij} &= c_{ijkl} S_{kl} \quad i, j, k, l = x, y, z \quad c_{ijkl} - stiffness\ coefficients \\ S_{ij} &= s_{ijkl} T_{kl} \quad i, j, k, l = x, y, z \quad s_{ijkl} - compliance\ coefficients \quad . \end{aligned} \tag{2-6}$$

The symmetrical tensors **T** *and* **S** have only six different components, thus we can simplify the notation by introducing the following substitutions:

$$T_p = T_{ij}, \tag{2-7}$$

$$S_q = \begin{cases} S_{ij} & for \quad i = j \\ 2S_{ij} & for \quad i \neq j \end{cases} \qquad where \quad i, j = 1, 2, 3 \ ; \ q = 1, 2, 3, 4, 5, 6. \tag{2-8}$$

The relationships between the indexes are:

$$\begin{aligned} &11 \to 1 \quad 22 \to 2 \quad 33 \to 3 \\ &23 \to 4 \quad 13 \to 5 \quad 12 \to 6 \end{aligned} \tag{2-9}$$

From the symmetrical form of both stress and strain tensors follows the symmetric form of the compliance and stiffness tensors. Therefore, the original 81 components of both fourth rank tensors can be reduced to a maximum of 36 independent constants, which are elements of a 6x6 matrix.
Consequently, using the above conventions, equations (2-6) can be simplified into the following form:

$$\begin{aligned} T_p &= c_{pq} S_q \quad p,q = 1,2,3,4,5,6; \\ S_p &= s_{pq} T_q. \end{aligned} \tag{2-10}$$

Comparing the equations (2-6) and (2-10) we can realize the relationships:

$$\begin{aligned} s_{pq} &= s_{ijkl} \quad \textit{for } p,q = 1,2,3; \\ s_{pq} &= 2s_{ijkl} \quad \textit{for } \text{either } p \textit{ or } q = 4,5,6; \\ s_{pq} &= 4s_{ijkl} \quad \textit{for } \text{both } p \textit{ and } q = 4,5,6. \end{aligned} \tag{2-11}$$

Since the stiffness and compliance matrixes in equations (2-10) are not tensors, they have to be transformed using a different transformation law, which will be discussed in section 2.4.

2.2 Resistive and piezoresistive tensors

The relation between the electric field vector $\mathbf{E}$ and electric current density $\mathbf{J}$ is given by Ohm's law:

$$\mathbf{J} = \boldsymbol{\sigma}\mathbf{E}, \tag{2-12}$$

The electric field vector is proportional to the current vector by a symmetrical conductivity tensor of rank two with nine components.
The piezoresistive effect indicates that the stress tensor in crystalline materials causes a change of the conductivity tensor:

$$\frac{d\sigma_{ij}}{\tilde{\sigma}} = -\pi_{ijkl} T_{kl} \tag{2-13}$$

or in matrix notation:

$$\frac{d\sigma_{p}}{\tilde{\sigma}} = -\pi_{pq} T_{q}\,, \tag{2-14}$$

where: $\tilde{\sigma} = (\sigma_{11} + \sigma_{22} + \sigma_{33})/3$.

The origin of the piezoresistive coefficients will be discussed in Chapter 4.

2.3 Simplification by crystal symmetry

The Neumann's principle [24] states that: *Every physical property of an object must have at least the symmetry of the point group of the object*. This means, that the symmetry operations from the point group of the elementary cell did not change any physical parameters of the crystal. The silicon crystal has a diamond type lattice structure, for which there exist 48 point symmetric operations. By applying all symmetry operations one by one, the matrix describing the two-index matrix coefficients can be significantly reduced, yielding [25]:

$$\mathbf{p} = \begin{pmatrix} p_{11} & p_{12} & p_{12} & 0 & 0 & 0 \\ p_{12} & p_{11} & p_{12} & 0 & 0 & 0 \\ p_{12} & p_{12} & p_{11} & 0 & 0 & 0 \\ 0 & 0 & 0 & p_{44} & 0 & 0 \\ 0 & 0 & 0 & 0 & p_{44} & 0 \\ 0 & 0 & 0 & 0 & 0 & p_{44} \end{pmatrix}, \tag{2-15}$$

where $\mathbf{p}$ is any property of the crystal- (in this thesis we deal with stiffness, compliance and piezoresistive matrixes).

Thus, the cubic symmetry of silicon reduces the number of non zero independent components to three constants. Instead of components of the compliance and stiffness

the following material constants are often used: Young's modulus (Y), Poisson's ratio (ν) and Shear modulus (G). They are defined respectively as:

$$\begin{aligned} \frac{1}{Y} &= s_{11} = \frac{c_{11}+c_{12}}{(c_{11}-c_{12})(c_{11}+2c_{12})}, \\ \nu &= -\frac{s_{12}}{s_{11}} = \frac{c_{12}}{c_{11}+c_{12}}, \\ \frac{1}{G} &= s_{44} = \frac{1}{c_{44}}. \end{aligned} \tag{2-16}$$

The silicon material constants in crystallographic coordinates are given in the Appendix - *Table 8*.

2.4 Coordinate transformation of the coefficients in matrix notation

All of the above equations were developed with the coordinate axes corresponding to the $[100]$ directions of a crystal (crystallographic coordinates) in the cubic family. It would be more general and more useful to express the coefficients for an arbitrary direction. This can be done by defining longitudinal and transverse coefficients, p_l and p_t. The longitudinal coefficient refers to the case where the *applied field* is in the same direction as the *induced field*, whereas the transverse coefficient refers to the case where the *applied field* is perpendicular to the *induced field*.
Generally the arbitrary rotation of one coordinate system can be presented as:

$$x'_i = a_{ij} x_j . \tag{2-17}$$

There are many ways to describe 3D rotations. However, in physics, the Euler's angles α, β and γ are often used, (see *Figure 2.1*). With such parameterisation the components of the transformation matrix can be expressed as [26]:

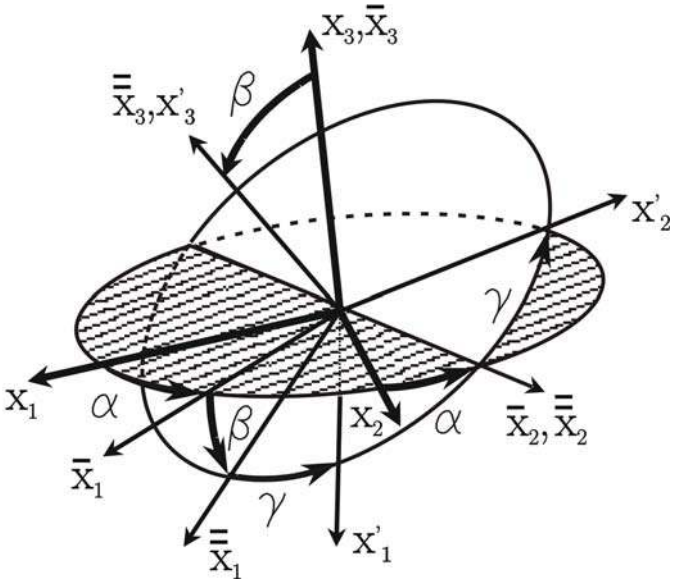

Figure 2.1 Definition of the Euler's angles.

$$\begin{pmatrix} a_{11} & a_{12} & a_{13} \\ a_{21} & a_{22} & a_{23} \\ a_{31} & a_{32} & a_{33} \end{pmatrix} \equiv \begin{pmatrix} l_1 & m_1 & n_1 \\ l_2 & m_2 & n_2 \\ l_3 & m_3 & n_3 \end{pmatrix} = \begin{pmatrix} \cos\alpha & -\sin\alpha & 0 \\ \sin\alpha & \cos\alpha & 0 \\ 0 & 0 & 1 \end{pmatrix} \begin{pmatrix} 1 & 0 & 0 \\ 0 & \cos\beta & -\sin\beta \\ 0 & \sin\beta & \cos\beta \end{pmatrix} \begin{pmatrix} \cos\gamma & -\sin\gamma & 0 \\ \sin\gamma & \cos\gamma & 0 \\ 0 & 0 & 1 \end{pmatrix} = \tag{2-18}$$

$$= \begin{pmatrix} \cos\alpha\cos\beta\cos\gamma - \sin\alpha\sin\gamma & \cos\alpha\cos\beta\cos\gamma + \sin\alpha\sin\gamma & -\cos\alpha\sin\beta \\ -\sin\alpha\cos\beta\cos\gamma - \cos\alpha\sin\gamma & -\sin\alpha\cos\beta\cos\gamma + \cos\alpha\cos\gamma & \sin\alpha\sin\gamma \\ \sin\beta\cos\gamma & \sin\beta\sin\phi & \cos\beta \end{pmatrix},$$

where l_i, m_i and n_i are known as direction cosines.

When we have the transformation of the coordinate system described by the above equation, the transformation rule for a tensor of rank-n is given by:

$$A_{i'_1 i'_2 \ldots i'_n} = a_{i'_1 i_1} a_{i'_2 i_2} \ldots a_{i'_n i_n} A_{i_1 i_2 \ldots i_n} . \tag{2-19}$$

Then the tensors of second rank in the simplified notation are transforms of the type:

$$A'_i = \alpha_{ij} A_j , \tag{2-20}$$

where [27]:

$$\boldsymbol{\alpha} = \begin{pmatrix} l_1^2 & m_1^2 & n_1^2 & 2m_1n_1 & 2n_1l_1 & 2l_1m_1 \\ l_2^2 & m_2^2 & n_2^2 & 2m_2n_2 & 2n_2l_2 & 2l_2m_2 \\ l_3^2 & m_3^2 & n_3^2 & 2m_3n_3 & 2n_3l_3 & 2l_3m_3 \\ l_2l_3 & m_2m_3 & n_2n_3 & m_2n_3 + m_3n_2 & n_2l_3 + n_3l_2 & m_2l_3 + m_3l_2 \\ l_3l_1 & m_3m_1 & n_3n_1 & m_3n_1 + m_1n_3 & n_3l_1 + n_1l_3 & m_3l_1 + m_1l_3 \\ l_1l_2 & m_1m_2 & n_1n_2 & m_1n_2 + m_2n_1 & n_1l_2 + n_2l_1 & m_1l_2 + m_2l_1 \end{pmatrix}. \tag{2-21}$$

It can be also shown that tensors of fourth rank, which give the relations between two tensors of second rank, in the simplified notation, transform as:

$$A'_{pq} = \alpha_{pr} A_{rt} \alpha^{-1}_{tq}. \tag{2-22}$$

For example, applying the above transformation law we can express the longitudinal and transversal piezoresistive coefficients in an arbitrary direction, respectively, as:

$$\begin{aligned} \pi_l \equiv \pi'_{11} &= \pi_{11} - 2(\pi_{11} - \pi_{12} - \pi_{44})\left(l_1^2 m_1^2 + l_1^2 n_1^2 + m_1^2 n_1^2\right), \\ \pi_t \equiv \pi'_{12} &= \pi_{12} + (\pi_{11} - \pi_{12} - \pi_{44})\left(l_1^2 l_2^2 + m_1^2 m_2^2 + n_1^2 n_2^2\right). \end{aligned} \tag{2-23}$$

Thus, using the values of the piezoresistive coefficients in the crystallographic coordinate system (*Table 8*) we can calculate the piezoresistive coefficients in an arbitrary direction of the (001) wafer plane. As two of the Euler's angles β and γ are equal to zero, we can find the extreme value of the piezoresistive coefficients with respect to α. For n-type Si the maximum magnitude of the piezoresistive coefficients occurs at $\alpha = 0$, which is equivalent to the [100] direction ($\pi_{l,max} = \pi_{11} = -102.2 \times 10^{-11}\ m^2/N$, $\pi_{t,max} = \pi_{12} = 53.4 \times 10^{-11}\ m^2/N$). Moreover, for p-type Si the maximum magnitude of the piezoresistive coefficients occurs at $\alpha = \pi/4$, which is equivalent to the [110] direction ($\pi_{l,max} = \pi_{11} - (\pi_{11} - \pi_{12} - \pi_{44})/2 = 71.8 \times 10^{-11}\ m^2/N$, $\pi_{t,max} = \pi_{12} + (\pi_{11} - \pi_{12} - \pi_{44})/2 = -66.3 \times 10^{-11}\ m^2/N$).

Chapter 3
Quantum mechanical background

While the preceding sections presented the continuum theory, we will now turn towards to the methods, which allow an atomistic description of a semiconductor crystal as a system consisting of atoms and electrons. Consequently this theory will be applied to model the piezoresistive effect.

A material is said to be piezoresistive when an applied stress/strain results in a change in the material's electrical resistance. Piezoresistive transducers have the advantages of simple fabrication and simple interface circuits.

A stretched wire grows longer and thinner, which increases its resistance from geometry alone. Any conducting material can act as a strain gauge by this geometrical mechanism, but piezoresistive sensing usually refers specifically to strain gauges in semiconductors. The electrical properties of some doped semiconductors respond to stress with resistance changes over 100 times greater than those attributable to geometric changes alone.

Piezoresistive effect in silicon was discovered more than fifty years ago [28], and is widely used in commercial pressure sensors and accelerometers.

The piezoresistors in silicon are created by introducing dopant atoms to create a conducting path. When the silicon experiences stress, and therefore strain, the lattice spacing between the atoms changes. This change affects and alters the band structure by either shifting it in energy, distorting it, removing degeneracy effects, or any combination of the three and thus affects the conductivity.

In this chapter, the microscopic theory for analysis of the piezoresistive effect will be introduced based on general quantum mechanics and semiconductor physics. As a starting point, we will introduce the Hamiltonian of the whole crystal and then consider the approximations usually assumed in order to calculate its energy states.

3.1 Electrons in a perfect crystal

The stationary many-electron Schrödinger equation is:

$$H\Psi = E\Psi \,, \tag{3-1}$$

where H is the Hamiltonian operator that incorporates all kinetic and potential energies of the system. As in a crystal, there a huge number of simultaneous interactions occurring between every electron and every atom core, the Hamiltonian describing the electron states in perfect crystal takes the form:

$$H = -\frac{\hbar^2}{2m}\sum_i \nabla^2_{\mathbf{r}_i} - \frac{\hbar^2}{2}\sum_i \frac{\nabla^2_{\mathbf{R}_i}}{M_i} + \sum_{j<k}\frac{e^2}{r_{jk}} + \sum_{iJ}\frac{Z_J e^2}{r_{iJ}} + \sum_{J<K}\frac{Z_J Z_K e^2}{R_{JK}}\,. \tag{3-2}$$

The first and second terms represent kinetic energy contribution due to the electron and lattice vibrations, respectively. The next three terms represent the electron-electron, electron-nuclei and nuclei-nuclei Coulomb interaction, respectively. As even a small crystal contains a huge number of nucleus and electrons, the problem, as it stands, is practically impossible to be solved. Further approximations are outlined in the following section.

In general it is difficult to obtain a complete solution to the problem of many-particle quantum systems. Each electron experiences a potential that depends on its own position and the rest of the electrons. This non-locality of the potential makes the Schrödinger equation extremely difficult to be solved. Further we will consider a possible approximation, which can be applied in order to simplify the problem.

3.2 Approximations

Ion cores have masses which may be up to 10^4 times of the electron mass, and consequently it can be shown that the ion core moves much slower than the electrons (approximately 10^3). As a result, the electrons effectively exhibit an adiabatic

response, adjusting their motion almost instantaneously to the ion core, while the ion cores see only a time-average (adiabatic) electronic potential. The adiabatic approximation is also known as the Born-Oppenheimer approximation. The Hamiltonian can be now expressed as a sum of two terms, which described the electron and ion motions separately. For the electron motion we assume that the ion cores are *frozen* at position $\mathbf{R}_J$. Thus, we may split the wave function of the system into electronic $\varphi(\mathbf{r})$ and ionic $\Phi(\mathbf{R})$components, such that:

$$\Psi(\mathbf{r},\mathbf{R}) = \varphi(\mathbf{r})\Phi(\mathbf{R}). \tag{3-3}$$

The problem can be reformulated as two eigenvalue problems, yielding both electronic and ionic eigensolutions. The first problem, which will be further discussed, gives a solution for the electronic band structure. The second one gives a solution for the crystal lattice vibration properties known as phonons.
The electronic eigenvalue equation is represented by:

$$H\varphi(\mathbf{r}) = E\varphi(\mathbf{r}) \quad where \quad H = -\frac{\hbar^2}{2m}\sum_i \nabla^2_{\mathbf{r}_i} + \sum_{j<k}\frac{e^2}{\mathbf{r}_{ik}} - \sum_{iJ}\frac{Z_J e^2}{\mathbf{r}_{iJ}}. \tag{3-4}$$

The above equation still represents a many-body problem. Hartree suggested that in a many electron system it is possible to approximate the potential energy of the electron-electron interaction (second term) by a time average potential $U(\mathbf{r})$, in which the electrons move independent. This leads to a self-consistent equation. Thus we have to solve a single electron Schödinger equation of the form:

$$\left[-\frac{\hbar^2}{2m}\nabla^2 + V(\mathbf{r})\right]\varphi = E\varphi \quad where \quad V(\mathbf{r}) = U(\mathbf{r}) - \sum_J \frac{Z_J e^2}{\mathbf{r}_{iJ}}. \tag{3-5}$$

The band structure of semiconductors can be obtained by solving equation (3-5) with various approaches: the pseudopotential method, the linear coupled atomical orbital (LCAO) method, the free-electron approximation method and the **kp** perturbation (effective mass) method. All of these methods take into account the translation

symmetry of the crystal. Here we will deal with the **kp** perturbation method, for which the remaining problem lies in the representation of the wave function in case of the translation symmetry of the potential. The solution of this problem leads to the Bloch's theorem, which describes the form of the eigenfunction in a spatially periodic potential as:

$$\varphi_{\mathbf{k}}(\mathbf{r}) = u_{\mathbf{k}}(\mathbf{r})\, e^{i\mathbf{k}\mathbf{r}}, \tag{3-6}$$

where

$$u_{\mathbf{k}}(\mathbf{r}) = u_{\mathbf{k}}(\mathbf{r}+\mathbf{R}). \tag{3-7}$$

Introducing the wave function from equation (3-6) into equation (3-5) we have:

$$-\frac{\hbar^2}{2m}\nabla^2 u_{\mathbf{k}} + V(\mathbf{r})u_{\mathbf{k}} - \frac{i\hbar^2}{m}\mathbf{k}\nabla u_{\mathbf{k}} + \frac{\hbar^2\mathbf{k}^2}{2m}u_{\mathbf{k}} = E_{\mathbf{k}}u_{\mathbf{k}}. \tag{3-8}$$

If we define the momentum operator $\mathbf{p} = -i\hbar\nabla$, the above equation at $\mathbf{k} = \mathbf{k}_0$ has the form:

$$\left[\frac{\mathbf{p}^2}{2m} + V(\mathbf{r}) + \frac{\hbar}{m}\mathbf{k}_0\mathbf{p}\right]u_{n\mathbf{k}_0} = \left[E_{n\mathbf{k}_0} - \frac{\hbar^2\mathbf{k}_0^2}{2m}\right]u_{n\mathbf{k}_0} \tag{3-9}$$

Here $V(\mathbf{r})$ is the potential of the unstrained unit cell, $E_{n\mathbf{k}_0}$ is the energy spectrum of the unstrained crystal at $\mathbf{k}_0$ and $u_{n\mathbf{k}_0}$ is the *unstrained* electron Bloch wave function which transforms according to the representation located at $\mathbf{k}_0$ (see section 3.5).

3.3 Band structure in the presence of strain

In the strained crystal, the unit cell is deformed but it still remains periodic, consequently retaining the periodicity of the wave function. Thus, we can write the

equation (3-9) at wave vector $\mathbf{k}_0 + \mathbf{k}$ for the wave function in the strained crystal satisfying the equation:

$$\left[\frac{\mathbf{p}'^2}{2m} + V(\mathbf{r}') + \frac{\hbar}{m}(\mathbf{k}_0 + \mathbf{k})\mathbf{p}'\right] u'_{n\mathbf{k}_0} = \left[E'_{\mathbf{k}} - \frac{\hbar^2(\mathbf{k}_0 + \mathbf{k})^2}{2m}\right] u'_{n\mathbf{k}_0}. \qquad (3\text{-}10)$$

In order to find the perturbation term, the above equation should be written in terms of the unstrained (unprimed) coordinate system. Thus we have to look how the terms $\mathbf{p}'$ and $V(\mathbf{r}')$ will be transformed. The relationship between the coordinate systems in strained and unstrained crystals can be written as:

$$x'_i = x_i + S_{ij}x_j. \qquad (3\text{-}11)$$

Using such a transformation of the coordinate system we can find the transformation law for the momentum and potential as:

$$p'_i = -i\hbar\frac{\partial}{\partial x'_i} = -i\hbar\frac{\partial}{\partial x_j(\delta_{ij} + S_{ij})} \approx (\delta_{ij} - S_{ij})\left(-i\hbar\frac{\partial}{\partial x_j}\right) = (\delta_{ij} - S_{ij})\,p_j, \qquad (3\text{-}12)$$

$$\mathbf{p}'^2 = p'_i p'_i \approx \mathbf{p}^2 - 2p_i p_i \delta_{ij} S_{ij} = \mathbf{p}^2 - 2p_i S_{ij} p_j, \qquad (3\text{-}13)$$

$$V(\mathbf{r}') = V(\mathbf{r}) + V_{ij}(\mathbf{r})S_{ij} \qquad \textit{where} \quad V_{ij}(\mathbf{r}) = \frac{\partial V((\mathbf{1}+\mathbf{S})\mathbf{r})}{\partial S_{ij}}\Big|_{\mathbf{S}=0}. \qquad (3\text{-}14)$$

By comparing the Schrödinger equations for strained and unstrained crystals we can find the term acting as a perturbation in the form:

$$\delta H(\mathbf{S}) = H_{\mathbf{S}}((1+\mathbf{S})\mathbf{r}) - H_0 \qquad (3\text{-}15)$$

or

$$\delta H(\mathbf{k},\mathbf{S}) = H_{\mathbf{S}} + H_{\mathbf{k}} + H_{\mathbf{kS}} \equiv \Xi_{ij}S_{ij} + \left[\frac{\hbar}{m}\mathbf{k}(\mathbf{p} + \hbar\mathbf{k}_0) + \frac{\hbar^2\mathbf{k}^2}{2m}\right] + \left[i\frac{\hbar^2}{m}k_i S_{ij}\frac{\partial}{\partial x_j}\right]. \qquad (3\text{-}16)$$

where:

$$\Xi_{ij} = \left[\frac{\hbar^2}{m} \frac{\partial^2}{\partial x_i \partial x_j} + V_{ij}(r) + i \frac{\hbar^2}{m} k_{0i} \frac{\partial}{\partial x_j} \right] \tag{3-17}$$

is known as deformational potential operator.

As we have arrived at the close form expression of the perturbation term, we can apply either the degenerate or nondegenerate perturbation theory in order to find the dispersion around the $\mathbf{k_0}$ in the presence of stress $\mathbf{S}$. Further, we are interested in such places $\mathbf{k_0}$ of the band structure at which the energy has an extremum. Thus, the linear terms in $\mathbf{k}$ vanish. The term of order $\mathbf{kS}$ describes only small changes of the energy.

Further we will employ the first order perturbation theory in $\mathbf{S}$ and the second order in $\mathbf{k}$ for the above-obtained perturbation.

3.4 Spin-orbit interaction

In the previous section the perturbation Hamiltonian was obtained without considering the electron spin. In order to include the interaction of the electron spin with the magnetic field induced by the electron orbital movement we have to consider an additional perturbation term, which will be estimated below.

The spin-orbit coupling is a relativistic effect. Here will be demonstrated only a conclusion based on classical electrodynamics.

Since the electron has charge and spin it also has a magnetic moment $\boldsymbol{\mu} = -\mu_0 \boldsymbol{\sigma}$, where $\mu_0 = \frac{e\hbar}{2mc}$ is Bohr magneton and the components of vector $\boldsymbol{\sigma}$ are the Pauli spin matrices:

$$\boldsymbol{\sigma}_x = \begin{pmatrix} 0 & 1 \\ 1 & 0 \end{pmatrix}, \quad \boldsymbol{\sigma}_y = \begin{pmatrix} 0 & -i \\ i & 0 \end{pmatrix}, \quad \boldsymbol{\sigma}_z = \begin{pmatrix} 1 & 0 \\ 0 & -1 \end{pmatrix}. \tag{3-18}$$

If an electron moves with velocity $\mathbf{v}$ in an electrical field with intensity $\mathbf{E}$ it will *see*, in the coordinate system connected with it, the magnetic field $\mathbf{H}$:

$$\mathbf{H} = \left[\mathbf{E} \times \frac{\mathbf{v}}{c} \right]. \tag{3-19}$$

The intensity of the electric field is connected with the potential $V(\mathbf{r})$ as:

$$\mathbf{E} = -\frac{1}{e} \nabla V(\mathbf{r}). \tag{3-20}$$

As the energy of the dipole with moment $\boldsymbol{\mu}$ in the magnetic field $\mathbf{H}$ is equal to $\boldsymbol{\mu}\mathbf{H}$, we can finally express the classical spin-orbit operator as:

$$H_{so}^{cl} = \frac{\hbar}{2c^2 m^2} (\nabla V \times \mathbf{p}) \boldsymbol{\sigma}. \tag{3-21}$$

However this energy term is not complete, due to the relativistic effect called Thomas precession [29], the correct energy of the spin dipole is [30]:

$$H_{so} = H_{so}^{cl} / 2. \tag{3-22}$$

The above-obtained spin-orbit Hamiltonian is important for the proper description of the valence band structure (see Chapter 4.2) and has to be considered in addition to the perturbation given by (3-16).

3.5 Crystal symmetry of the Silicon

In previous sections the perturbation term to the Hamiltonian in the presence of strain has been obtained. In order to calculate the correction to the energy spectrum $E_{n\mathbf{k}_0}$ given by equation (3-9) the perturbation theory to the perturbation term has to be applied. As the perturbation theory method requires the *exact* wave function $u_{n\mathbf{k}_0}$ in

this section we will give an idea how they can be obtained using the symmetry properties of the crystal.

According to Wigner [26] the Schrödinger equation for any physical system has to be invariant with respect to the symmetry transformations of this system. For the classification of the symmetry transformation the well-developed mathematical apparatus of the group theory [31] is used. In terms of the group theory, symmetry operations which are carried out on spatial coordinates, are classified as group elements. When these operations are applied to some function of coordinates (in the configuration space of the system) we will generate a number of functions from which we can choose a set of n linearly independent functions called *basic functions*. The action of some symmetry operation R_S on any of the basic functions f_i results in a function $R_S[f_i]$ represented as a linear combination of basic functions i.e. $R_S[f_i] = a_{ij} f_j$. In such a manner applying the symmetry operation R_S to all basic functions we will generate a matrix a_{ij}. Thus, applying all symmetry operations one by one to the basic functions we obtain a set of matrices, which together with the usual rule for matrix multiplication form a group that is equivalent to the group of symmetry operations. The obtained group of matrices is called *representation with dimension n*. Obviously, generated matrices (i.e. the representation) depend on the basic functions. Further we are interesting in basic functions, which generate so-called *irreducible representations* or in other words representations that cannot be expressed in terms of representation of lower dimensionality.

As we have introduced the general definition used in group theory we can begin with the classification of symmetry properties of the elementary Si lattice and its reciprocals lattice. The elementary cell of Si can be expressed as two face-centred cubic (FCC) lattices with a size a_0, where the second lattice, in Cartesian coordinates is translated by vector $(a_0/4, a_0/4, a_0/4)$ relative to the first lattice, see *Figure 3.1a*. According to the crystallographic classification, the FCC lattice belongs to the cubic *syngony*. Its symmetrical properties are determined by the 48 symmetrical elements, which belong to the O_h point group and are generated from the 24 elements R_i of the group T_d (see *Table 1*) by adding the inversion operation J [26].

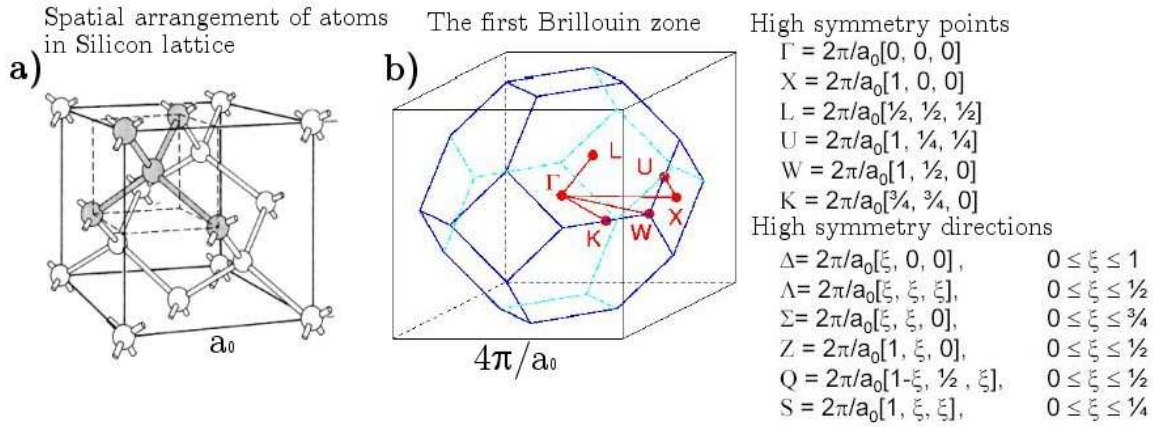

Figure 3.1 a) The diamond structure characteristic for Si and b) The first Brillouin zone of the FCC lattice.

Returning to the equation (3-9) and taking into account that the potential $V(\mathbf{r})$ has the symmetry of the elementary cell we will realize that the Hamiltonian is invariant under a part of the symmetry operation of the O_h group i.e. the symmetry is determined from the symmetry of the wave vector $\mathbf{k}_0$. As the wave vector is presented as a point in the reciprocal lattice space it is important to study the symmetrical properties at different points in the reciprocal lattice. The reciprocal lattice to the FCC is a body-centered cubic (BCC) lattice. The first Brillouin zone of the Si reciprocal lattice has the form of a *truncated octahedron* with volume $4(2\pi/a_0)^3$ - *Figure 3.1b*. Further we are interested in the points at which the conduction band minimum and valence band maximum are located. For the case of Si these points occur at point in Δ direction and in Γ point, respectively (for definitions see *Figure 3.1b*). The electronic states belong to one dimension Δ_1 representation with spherical symmetric base function, while the hole states belong to three dimension $\Gamma_{25}^{'}$ representation with basic functions $\{xy; yz; zx\}$ [32].

E	$R_1(xyz)$
$3C_4^2$	$R_2(xy_z_)$ $R_3(x_yz_)$ $R_4(x_y_z)$
$8C_3$	$R_5(yzx)$ $R_6(y_zx_)$ $R_7(y_z_x)$ $R_8(yz_x_)$ $R_9(zxy)$ $R_{10}(z_x_y)$ $R_{11}(zx_y_)$ $R_{12}(z_xy_)$
$6S_4=6JC_4$	$R_{13}(x_zy_)$ $R_{14}(x_z_y)$ $R_{15}(z_y_x)$ $R_{16}(zy_x_)$ $R_{17}(yx_z_)$ $R_{18}(y_xz_)$
$6\sigma=6JC_2$	$R_{19}(xzy)$ $R_{20}(xz_y_)$ $R_{21}(zyx)$ $R_{22}(z_yx_)$ $R_{23}(yxz)$ $R_{24}(y_x_z_)$

Table 1 Classification of the group T_d symmetrical element into six classes and its transformation laws.

In this chapter the stress influence on the Hamiltonian in terms of **kp** and deformation potential perturbation has been described. In addition the symmetrical properties of the Si crystal have been introduced in order to find the basis of Bloch wave functions. In the following chapter we will continue with calculations of the dispersion curves using the results obtained above.

Chapter 4
Calculation of the piezoresistive effect for the bulk piezoresistors-3D case

As already pointed out, the piezoresistive effect in semiconductors is due to the stress dependence of the band structure (*Figure 4.1*). Therefore, the effective-mass approximation (**kp** method) and the theory of deformation potential have been introduced in the previous chapter. This theoretical tool permit description of the effect of stress on the band structure near extreme points i.e. near the conduction band minimum and the valence band maximum. However, it is desirable to relate the fundamental theory of physical properties of semiconductors to the piezoresistive coefficients given by equation (2-14).

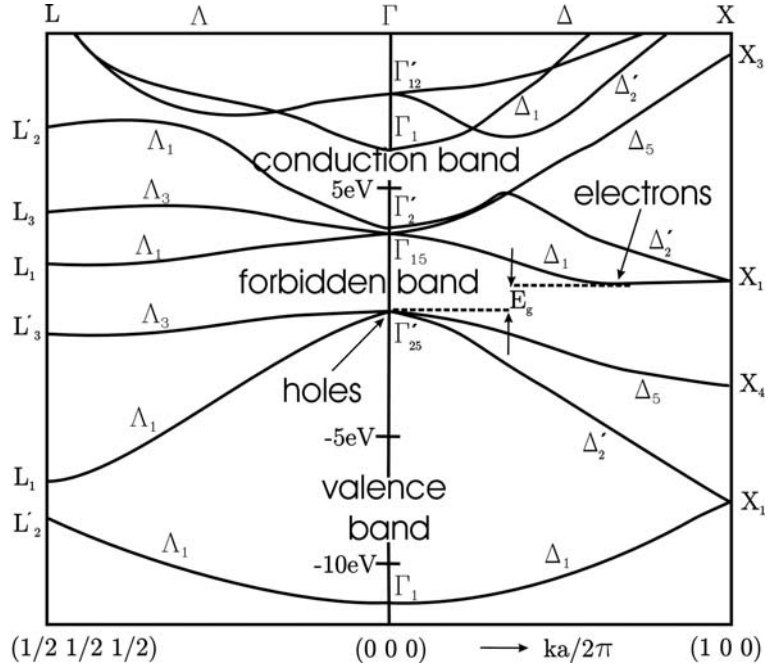

Figure 4.1 Dispersion relations for the energy E(k) of an electron or hole versus wave vector length in the first Brillouin zone of silicon (after [33]).

In this chapter we will use the previously obtained results to calculate the piezoresistive coefficients for n-type and p-type silicon.

4.1 Conduction band structure-piezoresistive coefficients

For silicon, the band edge of the conduction band is along the Δ direction near $\mathbf{k}=[3/4,0,0]$. Corresponding to this band edge there are six equivalent valleys, although under strain, the sixfold degeneracy of the conduction band is decomposed into a two- and fourfold degeneracy. Herring and Vogt [34] had described quantitatively the band edge shifting with the help of dilatation Ξ_d and shear deformation Ξ_u potentials. From cyclotron resonance experiments an additional parameter Ξ_m, which describes the stress inducing effective mass change, has been provided by Hensel [35].
In order to present the conduction band energy shift in terms of conduction band parameters, the results from the deformation potential theory obtained by H_S and H_{kS} in equation (3-16) for the case of the conductive band minima can be rewritten as [36]:

$$\begin{aligned}
\Delta E_{c1} &= \Xi_d\left(S_{11}+S_{22}+S_{33}\right)+\Xi_u S_{11}+\Xi_m S_{23}k_2k_3 \\
\Delta E_{c2} &= \Xi_d\left(S_{11}+S_{22}+S_{33}\right)+\Xi_u S_{22}+\Xi_m S_{13}k_1k_3 \\
\Delta E_{c3} &= \Xi_d\left(S_{11}+S_{22}+S_{33}\right)+\Xi_u S_{33}+\Xi_m S_{12}k_1k_2\ .
\end{aligned} \tag{4-1}$$

In n-type silicon, the piezoresistance is attributed to the raising or lowering of the conduction band minima under applied stress. *Figure 4.2*a shows the ellipsoidal constant energy surfaces in *k*-space for three of six equivalent conduction bands. The length of the major and minor axis, which can be obtained from perturbation theory with respect to the **kp** perturbation term, is indicative of the effective mass. Thus the electrons in longitudinal direction have high mass m_l (low mobility μ_l) while the transverse electrons have low mass m_t (high mobility μ_t). An electron current along one of the cubic axes (*Figure 4.2*a) consists of two types of electrons: Electrons with longitudinal mass and concentration n_l (Valley-1) and electrons with transversal mass and concentration n_t (Valleys-2, 3). Therefore the conductivity can be expressed as:

$$\sigma=\sum_{i=1..6} en_i\mu_i = 2en_l\mu_l+4en_t\mu_t = 2\frac{e^2n_l\tau_e}{m_l}+4\frac{e^2n_t\tau_e}{m_t}. \tag{4-2}$$

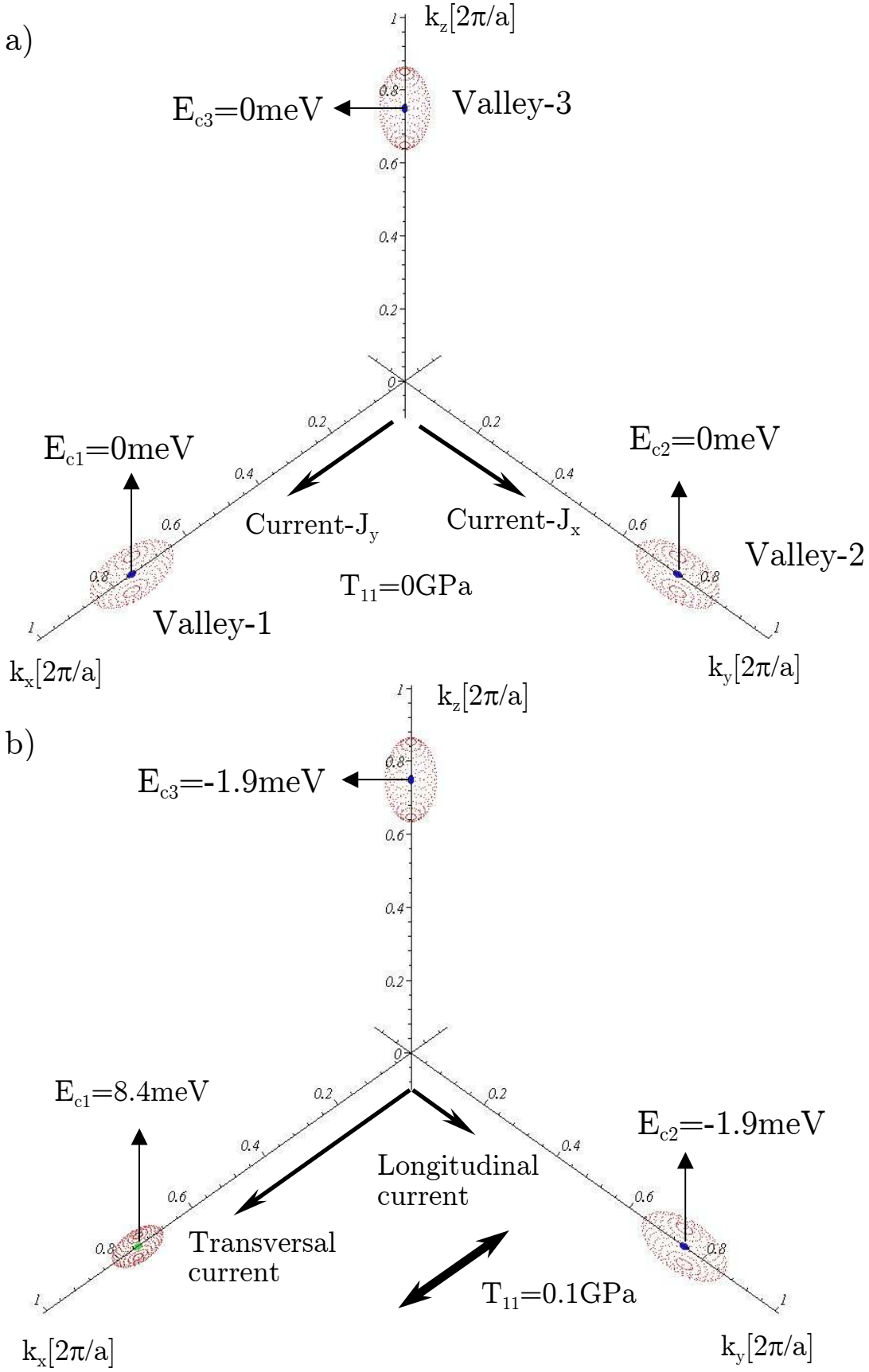

Figure 4.2 The conduction band isoenergetic surfaces (90meV) in relaxed and stressed silicon.

The effect of tensile stress on the conduction band structure and constant energy surfaces is shown in *Figure 4.2*b. If a uniaxial tensile stress is applied in x direction, the conduction band energy minimum at valley-1 is increased. This causes electrons to be transferred to valleys 2 and 3, which have lower energy minimum.
Referring to the theory of semiconductor physics [37], the free carrier concentration in every valley i can be obtain from:

$$n_i = N_c F_{1/2}\left(-\frac{E_{ci} - E_f}{k_B T}\right), \tag{4-3}$$

where the material effective density of states N_c and the half-order Fermi integral $F_{1/2}$ are defined, respectively, as:

$$N_c = 2\left(\frac{m_c^* k_B T}{2\pi\hbar^2}\right)^{3/2}, \qquad m_c^* \equiv \left(m_l m_t^2\right)^{1/3}, \tag{4-4}$$

$$F_s(\eta) = \int_0^\infty \frac{x^s dx}{e^{x-\eta}+1}, \quad s = 1/2. \tag{4-5}$$

The Fermi energy E_f is obtained from the neutral charge conditions:

$$\sum_{i=1..6} n_i = \frac{n_d}{1 + 0.5e^{\left(E_c - E_d - E_f\right)/k_B T}}, \tag{4-6}$$

where n_d and E_d are the donor concentration and donor energy level, respectively.
Using the equations (4-3) and (4-6) we can calculate the electron concentration in every valley. In case of tensile stress the concentration of electrons in valley-1 (which have longitudinal mass with respect to the current in x-direction; see *Figure 4.2*b) is decreased i.e. using the equation (4-2), a net decrease in resistivity is expected. Based on this model we can calculate the piezoresistive coefficients according to equation (2-14). The computed piezoresistive coefficients, for the conductive band parameters taken from *Table 8*, are presented in *Table 2*.

Concentration $[m^{-3}]$	Stress $[GPa]$	Concentration at stress $[m^{-3}]$	Shear mass $[atomic\ units]$	PR coefficients $[Pa^{-1}]$
$n_{valley1,2} = 1.66 \times 10^{21}$ $n_{valley3,4,5,6} = 1.66 \times 10^{2}$	$T_{11} = 0.1$	$n_{valley1,2} = 1.25 \times 10^{21}$ $n_{valley3,4,5,6} = 1.87 \times 10^{21}$	$m_{44}^{valley1,2} = 0$ $m_{44}^{valley3,4,5,6} = 0$	$\pi_{11} = -89.9 \times 10^{-11}$ $\pi_{12} = 45.0 \times 10^{-11}$
$n_{valley1,2} = 1.66 \times 10^{21}$ $n_{valley3,4,5,6} = 1.66 \times 10^{21}$	$T_{12} = 0.1$	$n_{valley1,2} = 1.66 \times 10^{21}$ $n_{valley3,4,5,6} = 1.66 \times 10^{21}$	$m_{44}^{valley1,2} = 11.12$ $m_{44}^{valley3,4,5,6} = 0$	$\pi_{44} = -8.6 \times 10^{-11}$

Table 2 Calculated piezoresistive coefficients at room temperature for boron-doped silicon ($E_c - E_d = 44meV \quad n_d = 10^{22} m^{-3}$).

The so called many-valley theory presented in this section describes n-type silicon very well. A large, negative π_{11} coefficient is predicted, π_{21} is expected to be the opposite in sign and with half magnitude of π_{11}. Finally, the shear coefficient, π_{44}, is predicted to be very small. The original data from Smith [28] confirm these predictions reasonably well.

4.2 Valence band structure - piezoresistive coefficients

While in the previous section the piezoresistive coefficients for the n-type silicon was calculated, in this section we will present the stress influence on the valence band structure. Thus we will be able to calculate the piezoresistive coefficients for the p-type silicon.

The near-band-edge valence band structure of the silicon is much more complicated than the conduction band, which leads to a more complex dependence of conductivity on stress. The top of the valence band, located at the Γ point, $\mathbf{k} = 0$ (see *Figure 4.1*), comprised two distinct bands, designated heavy-hole and light-hole. Considering the spin-orbit interaction, $44meV$ below the degenerate maximum of these two bands

appears the maximum of a third band, known as split-off band. Due to the *interaction* between the light-hole and split-off bands, the shape of the light-hole band is complex. In order to model the Si valence bands we use a **kp** description of the bands, see equation (3-16). As already pointed out, the states of the holes at the Brillouin zone centre belong to the $\Gamma_{25}^{'}$ representation of the O_h group. Basic functions $\{xy; yz; zx\}$ of this representation upon symmetry elements of the O_h group (see *Table 1*) transform similar to the $\{x; y; z\}$ [38]. Considering the electron spin we can order the basic function as:

$$\psi_1 = \left| x\uparrow \right\rangle,\ \psi_2 = \left| x\downarrow \right\rangle,\ \psi_3 = \left| y\uparrow \right\rangle,\ \psi_4 = \left| y\downarrow \right\rangle,\ \psi_5 = \left| z\uparrow \right\rangle,\ \psi_6 = \left| z\downarrow \right\rangle. \qquad (4\text{-}7)$$

Looking for the first order correction to the energy with respect to the strain and second order correction to the energy with respect to the **kp** perturbation, we can apply the perturbation theory to the perturbation Hamiltonian given with equation (3-16). Including the spin-orbit perturbation H_{SO}, this leads us to the following *secular* equation for the energy correction $E^{(\mathbf{kS})}$:

$$\left| H_{ii'}^{\mathbf{k}} + H_{ii'}^{\mathbf{S}} + H_{SO} - \mathrm{E}^{(\mathbf{kS})} \right| = 0, \qquad (4\text{-}8)$$

where:

$$H_{ii'}^{\mathbf{k}} = \sum_{\alpha\beta} k_\alpha k_\beta \underbrace{\sum_{i''\neq i,i'} \frac{\langle \psi_i | p_\alpha | \psi_{i''} \rangle \langle \psi_{i''} | p_\beta | \psi_{i'} \rangle}{E_i - E_{i''}}}_{S_{\alpha\beta,ii'}} \quad ; \quad \begin{matrix} i,i' = 1..6 \\ \alpha,\beta = 1..3 \end{matrix} \qquad (4\text{-}9)$$

$$H_{ii'}^{\mathbf{S}} = \sum_{\alpha\beta} \varepsilon_{\alpha\beta} \langle \psi_i | \Xi_{\alpha\beta} | \psi_{i'} \rangle. \qquad (4\text{-}10)$$

For presenting the matrix elements $H_{ii'}^{\mathbf{S}}$ and $H_{ii'}^{\mathbf{k}}$ in the basis given with (4-7), we will consider their symmetrical properties with respect to elements of the O_h group. The second sum $S_{\alpha\beta,ii'}$ in the Hamiltonian $H_{ii'}^{\mathbf{k}}$, upon acting of the symmetry operation, transforms like product the $\psi_i \cdot p_\alpha \cdot p_\beta \cdot \psi_{i'}$. The operators $p_\alpha \equiv -i\hbar\,\partial/\partial x_\alpha$, in this product, transform like coordinates x_α. Therefore the sum $S_{\alpha\beta,ii'}$ and the matrix elements $D_{ii'\alpha\beta} \equiv \langle \psi_i | \Xi_{\alpha\beta} | \psi_{i'} \rangle$ in the Hamiltonian $H_{ii'}^{\mathbf{S}}$ will be transformed in a similar way.

Let's now assume $i = i' = 1$.

When $\alpha \neq \beta$ we have $S_{\alpha\beta,11} = 0$ and $D_{\alpha\beta,11} = 0$. For example if $\alpha = 1$ and $\beta = 2$ ($1 \equiv x,\ 2 \equiv y,\ 3 \equiv z$) we can apply the symmetry element R_2 (see *Table 1*) to the sum $S_{12,11} \equiv xyxx$. The result is $R_2(xyxx) = -xyxx$ i.e. $S_{12,11} = 0$ and $D_{12,11} = 0$.

When $\alpha = \beta = 1$ we have $S_{11,11} \equiv xxxx$ and $D_{11,11} \equiv xxxx$. As we cannot find a symmetry element, which can change the sign, the matrix elements S_{1111} and D_{1111} are presented by constants. Thus we can define the following valence band parameter L and deformation potential l:

$$L = \frac{\hbar^2}{m^2} \sum_{i'' \neq 1} \frac{\langle x | p_x | \psi_{i''} \rangle^2}{E_1 - E_{i''}} \text{ and } l = \langle x | \Xi_{11} | x \rangle . \tag{4-11}$$

When $\alpha = \beta = 2$ (or $\alpha = \beta = 3$) we have $S_{11,22} \equiv xxyy$ and $D_{11,22} \equiv xxyy$ (or $S_{11,33} \equiv xxzz$ and $D_{11,33} \equiv xxzz$). We can see also that $R_{13}\left(xy^2x\right) = xz^2x$. Thus we can define another valence band parameter M and deformation potential m:

$$M = \frac{\hbar^2}{m^2} \sum_{i'' \neq 1} \frac{\langle x | p_y | \psi_{i''} \rangle^2}{E_1 - E_{i''}} = \frac{\hbar^2}{m^2} \sum_{i'' \neq 1} \frac{\langle x | p_z | \psi_{i''} \rangle^2}{E_1 - E_{i''}} \text{ and } m = \langle x | \Xi_{22} | x \rangle = \langle x | \Xi_{33} | x \rangle . \tag{4-12}$$

Finally we obtain:

$$H_{11}^{\mathbf{k}} = Lk_x^2 + M(k_y^2 + k_z^2) \text{ and } H_{11}^{\mathbf{S}} = lS_{xx} + m(S_{yy} + S_{zz}) . \tag{4-13}$$

If $i = 1$ and $i' = 2$ in similar way we can realize that it has only two non-zero members in the sum when $\alpha = 1$ and $\beta = 2$ or $\alpha = 2$ and $\beta = 1$. Thus we can define a third valence band parameter N and deformation potential n:

$$N = \frac{\hbar^2}{m^2} \sum_{i'' \neq 1} \frac{\langle x | p_x | \psi_{i''} \rangle \langle \psi_{i''} | p_y | y \rangle + \langle x | p_y | \psi_{i''} \rangle \langle \psi_{i''} | p_x | y \rangle}{E_1 - E_{i''}} \text{ and } n = \langle x | \Xi_{12} | y \rangle + \langle x | \Xi_{21} | y \rangle . \tag{4-14}$$

So the respective matrix elements can be written as:

$$H_{12}^{\mathbf{k}} = H_{21}^{\mathbf{k}} = Nk_x k_y \text{ and } H_{12}^{\mathbf{S}} = H_{21}^{\mathbf{S}} = nS_{12}\,. \tag{4-15}$$

Following the same technique we can find the rest of the matrix elements and finally we can construct the following Hamiltonian in the basis (4-7):

$$H = \begin{bmatrix} h_{xx} & 0 & h_{xy} - i\Delta'_{SO} & 0 & h_{xz} & \Delta'_{SO} \\ 0 & h_{xx} & 0 & h_{xy} + i\Delta'_{SO} & -\Delta'_{SO} & h_{xz} \\ h_{xy} + i\Delta'_{SO} & 0 & h_{yy} & 0 & h_{yz} & -i\Delta'_{SO} \\ 0 & h_{xy} - i\Delta'_{SO} & 0 & h_{yy} & -i\Delta'_{SO} & h_{yz} \\ h_{xz} & -\Delta'_{SO} & h_{yz} & i\Delta'_{SO} & h_{zz} & 0 \\ \Delta'_{SO} & h_{xz} & i\Delta'_{SO} & h_{yz} & 0 & h_{zz} \end{bmatrix}, \tag{4-16}$$

where:

$$h_{\alpha\alpha} = H_{\alpha\alpha}^{\mathbf{k}} + H_{\alpha\alpha}^{\mathbf{S}} = Lk_\alpha^2 + M(k_\beta^2 + k_\gamma^2) + lS_{\alpha\alpha}^2 + m(S_{\beta\beta}^2 + S_{\gamma\gamma}^2)\,, \tag{4-17}$$

$$h_{\alpha\beta} = H_{\alpha\beta}^{\mathbf{k}} + H_{\alpha\beta}^{\mathbf{S}} = Nk_\alpha k_\beta + nS_{\alpha\beta}\,, \tag{4-18}$$

$$\Delta'_{SO} \equiv \frac{\Delta_{SO}}{3} = \frac{i\hbar}{4m^2c^2}\left\langle x \left| \frac{\partial V}{\partial x} p_y - \frac{\partial V}{\partial y} p_x \right| y \right\rangle. \tag{4-19}$$

By using the above perturbation Hamiltonian, Dijkstra [39] has found analytical solutions for the valence band energies:

$$\begin{aligned} E_{SO}^{\mathbf{kS}} &= -2\sqrt{Q}\cos\left(\frac{\Theta}{3}\right) - p/3\,, \\ E_{hh}^{\mathbf{kS}} &= -2\sqrt{Q}\cos\left(\frac{\Theta + 2\pi}{3}\right) - p/3\,, \\ E_{lh}^{\mathbf{kS}} &= -2\sqrt{Q}\cos\left(\frac{\Theta - 2\pi}{3}\right) - p/3\,, \end{aligned} \tag{4-20}$$

where:

$$Q = \frac{p^2 - 3q}{9}\;;\quad R = \frac{2p^3 - 9pq + 27r}{54}\;;\quad \Theta = arc\cos\left(\frac{R}{\sqrt{Q^3}}\right), \tag{4-21}$$

and:

$$
\begin{aligned}
p &= -\left(h_{xx} + h_{yy} + h_{zz}\right) \ , \\
q &= h_{xx}(h_{yy} + h_{zz}) + h_{yy}h_{zz} - h_{xy}^2 - h_{xz}^2 - h_{yz}^2 - 3\left(\Delta'_{SO}\right)^2 \ , \\
r &= -h_{xx}h_{yy}h_{zz} + h_{xx}h_{yz}^2 + h_{yy}h_{xz}^2 + h_{zz}h_{xy}^2 - 2h_{xy}h_{xz}h_{yz} - p\left(\Delta'_{SO}\right)^2 + 2\left(\Delta'_{SO}\right)^3 \ .
\end{aligned}
\tag{4-22}
$$

The advantage of the above equation is that it expresses an analytical solution for the valence band energies, which gives us the possibility to increase the speed of the calculations significantly. Consequently we can calculate the energy values around the band edges in the Brillouin zone.

In the frame of this work the 3D k-space was divided into 300x300x300 equally spaced intervals. For all generated mesh points we calculate the corresponding energies, *Figure 4.3* shows the warped constant energy surfaces for heavy and light holes without stress and in presence of stress with magnitude T=10^8 Pa in direction [110]. The corresponding strain components in the crystallographic coordinate system, which are necessary for the calculation of the Hamiltonian elements, are:

$$
S_{\alpha\alpha} = S_{\beta\beta} = \left(s_{11} + s_{12}\right)T/2 \ ; \quad S_{\gamma\gamma} = s_{12}T \ ; \quad S_{\alpha\beta} = s_{44}T/4 \, . \tag{4-23}
$$

As we have two types of holes (heavy holes-hh and light holes-lh), the isotropic hole conductivity is the sum of both hole conductivities:

$$
\sigma = e^2\tau\left(\frac{n_{hh}}{m_{hh}} + \frac{n_{lh}}{m_{lh}}\right). \tag{4-24}
$$

Applying stress to the semiconductor results in a split between the upper valence bands, which finally changes the hole concentration. Beside that, a change in the warped constant energy surfaces shape, which is off course connected to the effective mass, will occur due to the same stress. In such a way change in the conductivity under an applied stress can be explained in the terms of hole transfer δn and mass change δm phenomena [40]:

$$
\delta\sigma_{ij} = e^2\tau\left(\frac{n_{hh}}{m_{ij}^{hh}}\frac{\delta n_{hh}}{n_{hh}} + \frac{n_{lh}}{m_{ij}^{lh}}\frac{\delta n_{lh}}{n_{lh}}\right) - e^2\tau\left(\frac{n_{hh}}{m_{ij}^{hh}}\frac{\delta m_{ij}^{hh}}{m_{ij}^{hh}} + \frac{n_{lh}}{m_{ij}^{lh}}\frac{\delta m_{ij}^{lh}}{m_{ij}^{lh}}\right). \tag{4-25}
$$

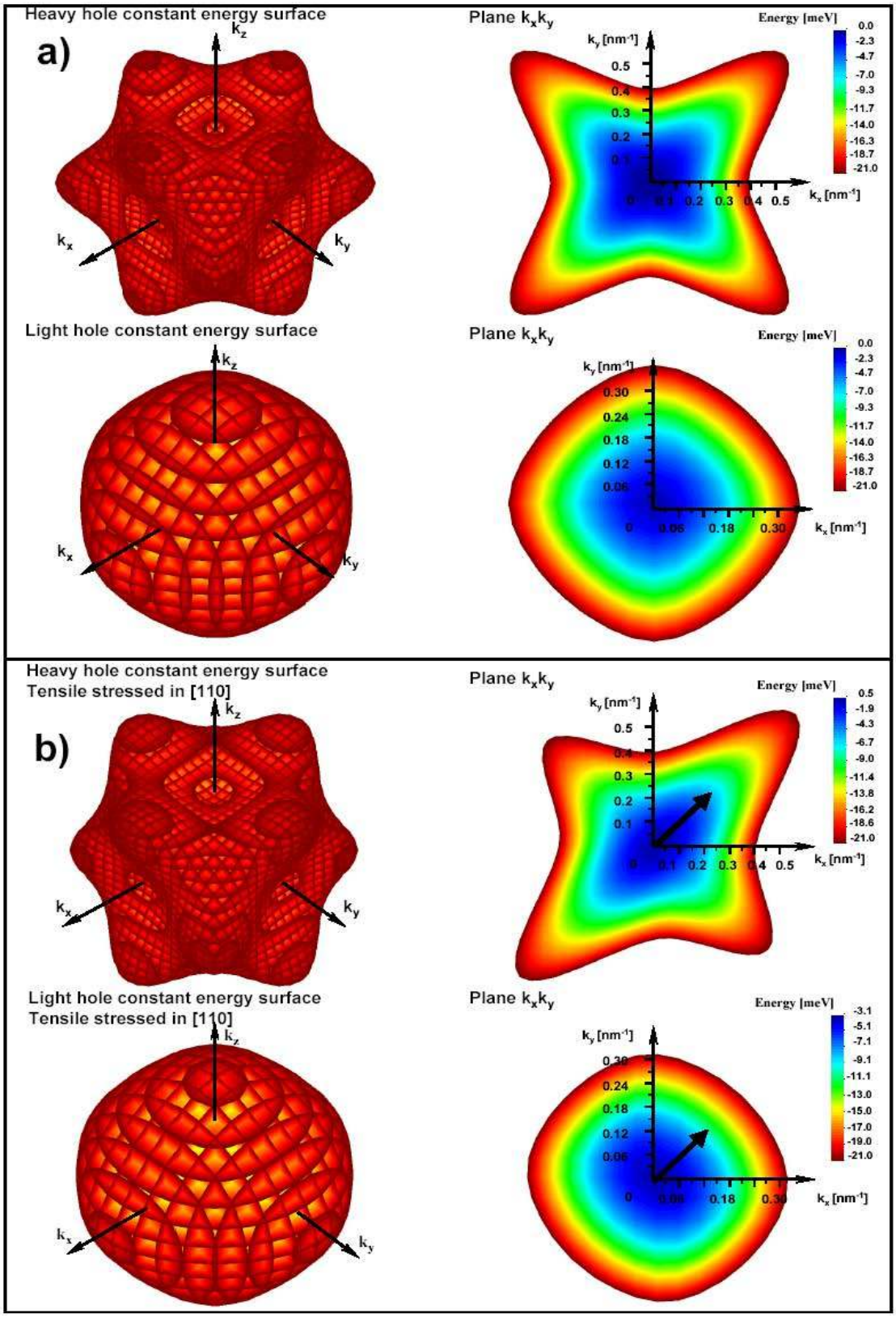

Figure 4.3 Warped heavy and light hole energy surfaces: (a) without stress and (b) with 10^8 Pa stress along [110] direction [41].

In order to calculate the piezoresistive coefficients with respect to equations (2-14), (4-24) and (4-25) we have to analyse hole concentrations and effective masses in two cases: i) without stress and ii) in the presence of stress.
Once dispersions have been calculated, hole concentrations can be calculated as well:

$$n_{hh} = 2 \int\limits_{\substack{hh \\ band}} g_{hh}(E) f(E) dE \,, \tag{4-26}$$

$$n_{lh} = 2 \int\limits_{\substack{lh \\ band}} g_{lh}(E) f(E) dE \,. \tag{4-27}$$

The density-of-states $g(E)$ of the given energy E, in the case of hh and lh are obtained from the numerical integration of the hh and lh volume, respectively; in k-space which are between the energy E and $E + dE$

$$g(E)dE = \frac{1}{(2\pi)^3} \int\limits_{E \le E_k \le E+dE} dk_x dk_y dk_z \,. \tag{4-28}$$

To calculate the Fermi-Dirac function for hole, $f(E) = \left(1 + \exp(E_f - E)\right)^{-1}$, we have to find the Fermi energy E_f from the equation, that is given by the charge conservation law:

$$\int\limits_{\substack{hh \\ band}} \frac{2 g_{hh}(E) dE}{1 + e^{(E_f - E)/kT}} + \int\limits_{\substack{lh \\ band}} \frac{2 g_{lh}(E) dE}{1 + e^{(E_f - E)/kT}} = \frac{n_a}{1 + 2e^{(E_a - E_f)/kT}} \,, \tag{4-29}$$

where: n_a and E_a are the acceptor concentration and acceptor energy level respectively. In such a way we could consequently find the Fermi energy and concentrations of the heavy and light holes.
In order to consider the mass change contribution to the piezoresistive effect we have to calculate the longitudinal and transversal effective masses with respect to the stress direction. They can be found from the following expression:

$$m_{ij}(E) = \hbar^2 \left(\frac{\partial^2 E}{\partial k_i \partial k_j} \right)^{-1} . \tag{4-30}$$

It is very important to note that the above effective mass depends very strongly on the energy. As an example in the case of unstressed silicon at the band edge ($E = 0meV$) the heavy and light effective mass, which are relevant to the [110] direction, are $m_{hh} = 0.37m_0$ and $m_{lh} = 0.12m_0$, respectively. On the other hand at energy $-25meV$ the heavy and light effective masses become $m_{hh} = 0.95m_0$ and $m_{lh} = 0.21m_0$, respectively. Then the hole effective masses are determined by [42]:

$$m_{ij} = \frac{\int m_{ij}(E) f(E) dE}{\int f(E) dE} . \tag{4-31}$$

Calculated piezoresistive coefficients in the [110] direction, according to equations (2-14), (4-24) and (4-25), are presented in Table 3.

It can be seen from the table that the origin of the longitudinal piezoresistive effect is caused by a change of the hole concentration (the concentration of heavy holes is increased as the concentration of light holes is decreased). However, the origin of the transversal piezoresistive effect is more complicated, it depends on the sum of two opposite phenomena: i) the change of the hole concentrations and ii) the change of the effective masses in transversal direction. The latter is the dominating phenomena.

Theoretically calculated longitudinal and transversal piezoresistive coefficients are in good agreement with values of longitudinal and transversal piezoresistive coefficients in [110] direction, which were obtained by experimentally piezoresistive coefficients in the crystallographic coordinate system (see Chapter 2.4).

	Without stress	With 10^8Pa Stress in [110] direction
Heavy holes		
$m_{hh(II)}/m_0$	0.512	0.512
$m_{hh(\perp)}/m_0$	0.512	0.376
n_{hh}/n_a	0.833	0.878
Light holes		
$m_{lh(II)}/m_0$	0.159	0.159
$m_{lh(\perp)}/m_0$	0.159	0.242
n_{lh}/n_a	0.167	0.122
Piezoresistive coefficients		
π_l [Pa^{-1}]	72.9×10^{-11} (exp. 71.8×10^{-11})	
π_t[Pa^{-1}]	-60.5×10^{-11} (exp. -66.3×10^{-11})	

Table 3 Calculated piezoresistive coefficients in p-type silicon at room temperature and acceptor concentration $n_a=10^{22}m^{-3}$.

4.3 Piezoresistive coefficients as a function of temperature and concentration

The above calculations were done at room temperature and fixed impurity concentration. In general, piezoresistive coefficients depend on the impurity concentration and temperature. In this section, according to the model proposed by Kanda [43], we will discuss the physical mechanism of this dependence.

As we mentioned, in the case of parabolic approximation $E = E_c + \hbar^2 k_\alpha^2 / m_\alpha$, the electron concentration is given by equation (4-3). By considering only the effect of electron concentration change due to the applied stress dT_{11}, which is true for n-type semiconductors, we can express the conductivity change as:

$$d\sigma = \frac{e\tau}{m} N_c \frac{\partial F(\eta)}{\partial \eta} \frac{-1}{k_B T} \frac{\partial (E_c - E_f)}{\partial T_{11}} dT_{11}, \quad \eta \equiv -\frac{E_c - E_f}{k_B T}. \tag{4-32}$$

Thus, the piezoresistive coefficient can be expressed as:

$$\pi\left(n_d,T\right)=-\frac{d\sigma}{dT_{11}}\frac{1}{\sigma}=\frac{1}{k_BT}\frac{F'_{1/2}(\eta)}{F_{1/2}(\eta)}\frac{\partial\left(E_c-E_f\right)}{\partial T_{11}}. \tag{4-33}$$

If we define the piezoresistive coefficient for a low doping concentration n_{d0} at room temperature as $\pi\left(n_{d0},300\right)$, we can obtain the following expression:

$$\pi\left(n_d,T\right)=\pi\left(n_{d0},300\right)\frac{300}{T}\frac{F'_{1/2}(\eta)}{F_{1/2}(\eta)}. \tag{4-34}$$

It is important to note that the relaxation time τ, so far, was assumed to be constant. However, in reality the scattering processes depend on energy, and we will now introduce an idea how to include the influence of energy dependent relaxation times on the piezoresistive coefficients. This method is based on the Boltzmann transport equation (BTE). The BTE expresses the fact that in the six-dimensional phase space of Cartesian coordinates $\mathbf{r}$ and momentum $\mathbf{p}$, the total rate of the distribution function $f\left(\mathbf{r},\mathbf{p},t\right)$ changing with time is equal to the scattering rate [44]:

$$\frac{\partial f}{\partial t}+\dot{\mathbf{r}}\nabla_{\mathbf{r}}f+\dot{\mathbf{p}}\nabla_{\mathbf{p}}f=\left(\frac{df}{dt}\right)_{collisions}. \tag{4-35}$$

Since it is not possible to obtain a solution to the above equation under the most general conditions, simplifying assumptions are necessary in order to solve the BTE. In the relaxation time approximation (RTA), the collision integral can be replaced by an algebraic equation that involves a parameter known as the relaxation time τ

$$\left(\frac{df}{dt}\right)_{collisions}=-\frac{f-f_0}{\tau}. \tag{4-36}$$

The solutions of the BTE in the RTA approximation for a nonequilibrium distribution function give us the possibility to express the current $\mathbf{J}$, which is due to the applied electrical field $\mathbf{E}$ ($\dot{\mathbf{p}}=e\mathbf{E}$) as:

$$\mathbf{J} = en\langle \dot{\mathbf{r}} \rangle = en\frac{2}{(2\pi)^3}\int \mathbf{v}f(\mathbf{r},\mathbf{p},t)d\mathbf{k} = -\frac{e}{4\pi^3}\int \tau(\mathbf{k})\frac{\partial f_0}{\partial \varepsilon}\mathbf{v}(\mathbf{vE})d\mathbf{k}. \tag{4-37}$$

According to Ohm's law (equation (2-12), we can express the conductivity as:

$$\sigma_{ij} = -\frac{e}{4\pi^3}\int \tau(\mathbf{k})\frac{\partial f_0}{\partial \varepsilon}v_i v_j d\mathbf{k}. \tag{4-38}$$

In most cases the relaxation time as a function of energy can be expressed as $\tau = \tau_0 E^s$, where s depends on the scattering type (*Table 4*). As a result, in the case of parabolic dispersion, we are able to obtain a simple formula for the conductivity [38]:

$$\sigma = NF_{s+1/2}(\eta). \tag{4-39}$$

Thus the piezoresistive coefficients as a function of the dopand concentration and temperature can, in the case of the energy dependent relaxation time, be expressed as a function of $s+1/2$ order Fermi integral:

$$\pi(n_d, T) = \pi(n_{d0}, 300)\frac{300}{T}\frac{F'_{s+1/2}(\eta)}{F_{s+1/2}(\eta)}. \tag{4-40}$$

According to the above equation, at low doping concentrations, there is higher stress sensitivity but stronger temperature dependence. As doping concentrations becomes higher than $10^{20} cm^{-3}$, the temperature dependence becomes indiscernible, but the sensitivity to stress decreases strongly. For sensors applications, such as thermally driven AFM cantilevers, with the width of thermal ranges usually required, these devices will almost certainly have to balance the sensitivity requirements with the temperature dependence of the piezoresistive coefficients.

Scattering center	Scattering mechanism	Fermi integral order-s
Phonons-longitudinal acoustic *dominant at intermediate and high temperatures*	Longitudinal acoustic phonons cause modulations of the band gap of the semiconductor through a deformation potential and thereby partial reflection of electron wave functions, which leads to a change in the electron wave vector.	**-1/2** [45 , 46]
Optical phonons *dominant at high temperatures*	Interact with the carriers through a deformation potential mechanism in nonpolar semiconductors.	**1/2** [45 , 46]
Ionized impurities *dominant at low temperatures and dopand materials*	Cause deflection of the trajectories of carriers due to the Coulomb potential.	**3/2** [46 , 47]
Neutral impurities *dominant at low ionized impurity density and low temperatures*	Various different models, which either treat neutral impurities as a Hydrogen atom immersed in a liquid with a certain dielectric constant or take into account that neutral impurities get easily ionised.	**0** [48 , 49]

Table 4 Important scattering centers.

Chapter 5
Piezoresistive effect in quantum wells

In biotechnology, microelectronics, and materials science, many products require a detailed understanding of microscopic and sub-microscopic fabrication methods. For the measurement equipment this is translated into demanding sensitivity requirements. Highly sensitive measurements become possible as the probe technology allows scaling of the electronic devices into the nanometer range. For scanning probe the maximal mechanical stress induced in the bended cantilever beam is located at the beam surface. Consequently, thin piezoresistors placed on the beam surface are desirable in order to ensure maximal sensitivity. Therefore, it is very important to understand the influence of the reduction and thickness scaling on the piezoresistive effect, which was presented in the previous chapter.

In this chapter we will present a model of the piezoresistivity effect in *ultrathin* piezoresistors by investigating the transport properties of the carriers under quantum confinement conditions in z direction.

5.1 Quantum confinement - 2D electron gas

The dimensional scaling of electronic devices leads to electron confinement in a space with the size L, comparable with the deBroglie wavelength of electron. Following the results from the quantum mechanical problem of a particle in a box [26] the confinement energy in a quantum well can be expressed as:

$$E_i^{l,t} = \frac{\pi^2 \hbar^2 i^2}{2 m_{l,t} L^2} \;\; ; \;\; i = 1, 2 \ldots , \qquad (5\text{-}1)$$

where m_l and m_t are the electrons longitudinal and transversal effective masses, respectively. This mean that, under the quantum confinement, for piezoresistors along the [100] direction of the silicon crystal, the confinement energy of two longitudinal valleys will be smaller than the confinement energy of the another four transverse valleys. This splitting of the valley energies is related to the difference of longitudinal and transverse effective mass in z direction ($m_l > m_t$). Since the longitudinal effective mass for electron in silicon is five times larger than the transverse effective mass, the electron in the longitudinal valleys 3i will have five-times smaller confinement energy than the electrons in valleys 1i and 2i (*Figure 5.1*a). As we received energy subbands of the conduction valleys, it is necessary to obtain subband occupations. Since the subband density of states is constant with energy, the occupation comes from the first-order Fermi integral, which is analytically integrable. In the electron case, we can write the occupation as [50]:

$$n_i = \frac{m_i}{\pi\hbar^2} \ln\left[1 + e^{\left(E_i - E_f\right)/k_B T}\right], \tag{5-2}$$

where m_i is the in-plane effective mass of the ith subband. In our case, for electrons in the longitudinal valleys, we have $m_i = m_t$. Whereas for those in the transverse valleys, we have $m_i = \sqrt{m_l m_t}$. The reason why we do not use m_l as in-plane effective mass for electrons in the transverse valleys is because the in-plane mass tensor in this case has different values along the x and y direction, which suggests an ellipsoidal shape for the constant energy surface.

For the value $L = 10nm$, accepted in the example, E_i for the first longitudinal subband (valley 3_1) is equal to $4.1meV$. The corresponding energies for the first transversal subbands (valleys 1_1 and 2_1) are quite considerable ($19.7meV$). Thus the dominant electron population is occurring for the valley 3_1.

Similarly to the case presented in the section 4.1, under stress along [100] direction the energy of the subband along k_x direction (valleys 1_1 and 1_2) will rise (*Figure 5.1*b).

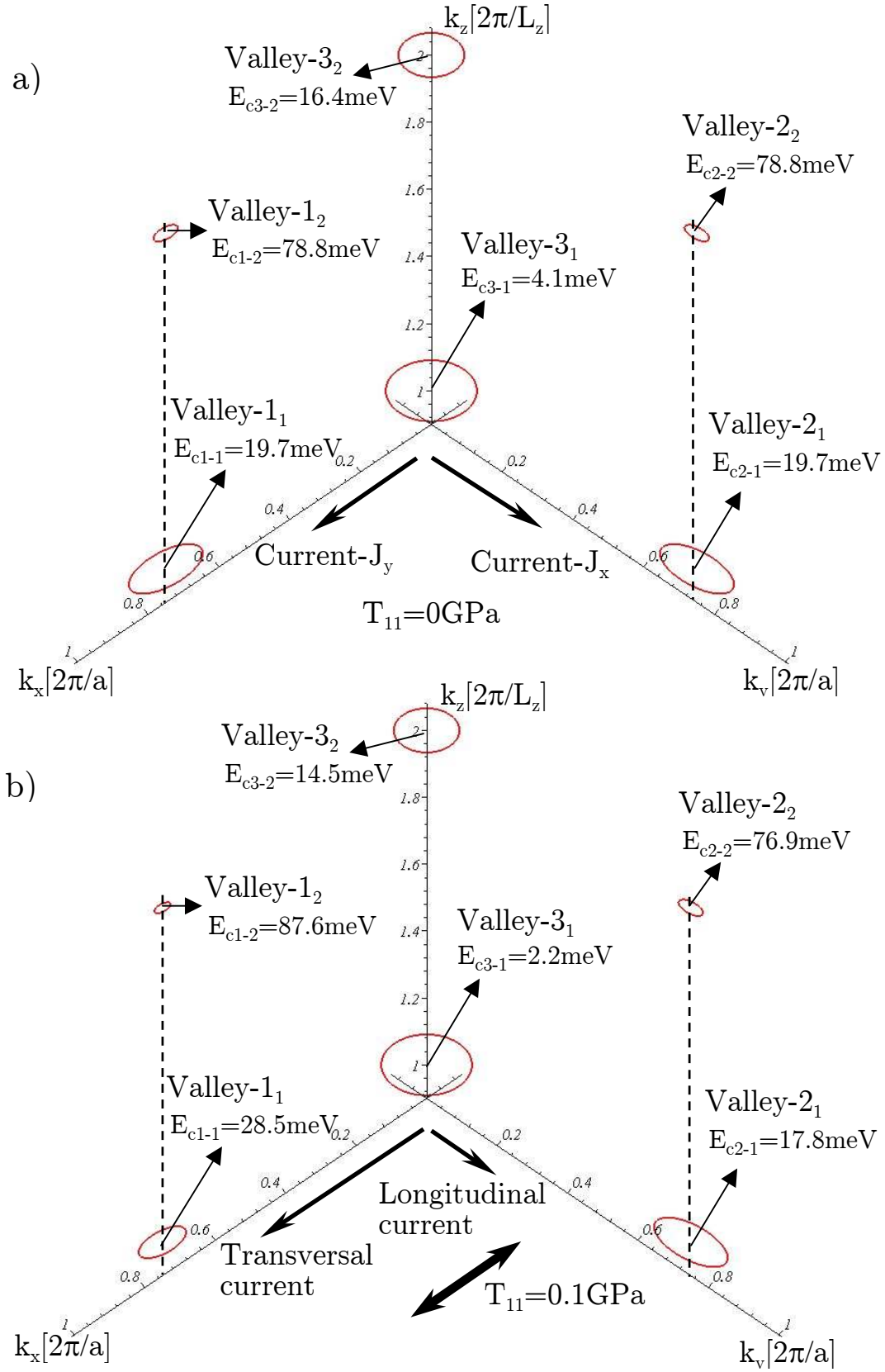

Figure 5.1 The conduction band isoenergetic energy lines (120meV) for a quantum well in a) relaxed and b) stressed silicon.

As the main part of conductivity is due to the dominant populated subband 3_1 and the conductivity change under the stress is due to the minor populated subband 1_1, we can expect lower values of the piezoresistive coefficients for the case of n-type quantum confined piezoresistivity. This can be seen from the *Figure 5.2*, where the piezoresistive coefficients are presented as a function on the quantum well thickness.

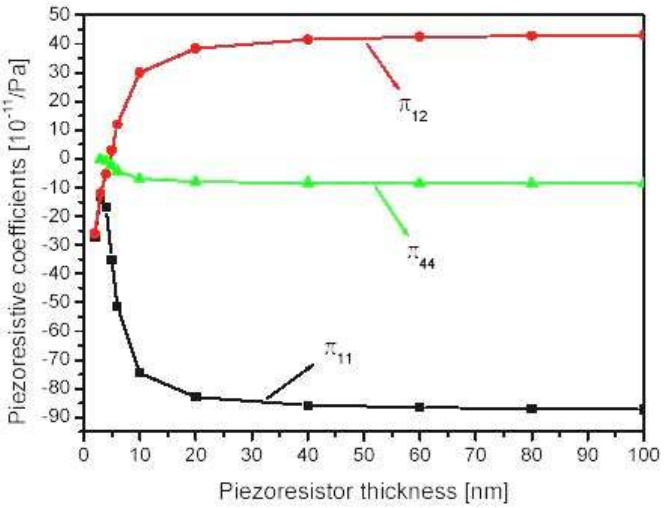

Figure 5.2 Piezoresistive coefficients in n-type quantum well vs. the quantum well thickness.

As a result of the above presented analysis we can conclude that cantilevers with n-type piezoresistors, thinner than 20nm, offer low deflection sensitivity.

5.2 Quantum confinement effect - 2D hole gas

As it was pointed out in the previous chapter, the degeneracy between the heavy and the light hole bands close to the Γ point makes the $E(\mathbf{k})$ energy dispersion complex and therefore leads to more complicated mechanism of the p-type piezoresistance in comparison with the n-type piezoresistance. The aim of this section is to study the space confinement influence on the valence band structure and consequently on the p-type piezoresistance. Since under confinement the translation invariance along the z direction is broken, now we have to interpret and substitute into the **kp** Hamiltonian, given by equation (4-16), the component of the wave vector k_z with the differential

operator $-i\partial/\partial z$. Thus the wave functions of the quantum states, in presence of a confinement potential V^{qw}, and the corresponding subband dispersion curves are solutions of the respective eigenvalue problem:

$$\sum_{\nu=1}^{6}\left[H_{\mu\nu}\left(k_x, k_y, k_z = -i\frac{\partial}{\partial z}\right) + \left(V^{qw} - E\right)\delta_{\mu\nu}\right]\Psi_\nu(\mathbf{r}) = 0, \qquad \Psi_\nu(\mathbf{r}) = F_\nu(z)e^{i\left(k_x x + k_y y\right)}. \quad (5\text{-}3)$$

As $\mu = 1..6$, the above equation represents a coupled set of six, second-order differential equations. Further the problem will be handled by expanding the wave functions in Fourier series:

$$F_\nu(z) = \sum_p \tilde{F}_{\nu,p} e^{ik_p z}, \qquad k_p = p\frac{2\pi}{L}, \quad (5\text{-}4)$$

where L is the periodic length of the structure (which, because of the solution method, is implicitly assumed to be a superlattice). A finite number p of k_p vectors are taken in consideration. Substituting the Fourier expanded wave functions, equation (5-4) into the equation (5-3), then multiplying from the left side by any one conjugate harmonic, integrating and finally using the orthogonality of plane waves we arrive at the following equation:

$$\sum_{\nu=1}^{6}\sum_p \left[H_{\mu\nu,pq} - E\delta_{\mu\nu}\delta_{pq}\right]\tilde{F}_{\nu,p} = 0, \quad (5\text{-}5)$$

where the matrix elements $H_{\mu\nu,pq}$ have the following form:

$$H_{\mu\nu,pq} = \int_{-L/2}^{L/2} e^{-ik_q z}\left(H_{\mu\nu} + V^{qw}\right)e^{ik_p z}. \quad (5\text{-}6)$$

Equation (5-5) presents an equation for eigenvalues and eigenvectors of a $6p \times 6p$ matrix.

The fact that the charge distribution reacts on the confining potential, which itself determines the charge distribution, imposes a stringent self-consistency requirement on

the energy level calculations. This requirement is accounted for by the self-consistent solution of equation (5-5), with a modified confining potential $\tilde{V}^{qw} = V^{qw} + e\Phi_{sc}(\mathbf{r})$, together with the Poisson's equation:

$$\frac{\partial^2 \Phi_{sc}}{\partial z^2} = -\frac{4\pi e}{\varepsilon_d}\left(\sum_{occupied\ p} n_p \sum_{\nu=1..6} \left| \tilde{F}_{\nu,p} e^{ik_p z} \right|^2 - n_{a-I} \right), \tag{5-7}$$

where ε_d is the dielectric constant of the material, n_{a-I} is the density of ionised acceptor impurities and n_p is the two dimensional electron concentration of the p[th] subband, which is expressed as:

$$n_p = 2\int \left\{ 1 - f\left(E_p\left(k_x, k_y\right) \right) \right\} \frac{dk_x dk_y}{4\pi^2}. \tag{5-8}$$

The Fermi energy will be calculated using the thermodynamical and electrical equilibrium conditions of the structure. These conditions will give us the following requirements: constant level of the Fermi energy and charge balance, expressed as:

$$\sum_{occupied\ p} n_p = n_{a-I} \ ; \quad n_{a-I} = \frac{n_a}{1 + 2e^{\left(E_a - E_f\right)/kT}}. \tag{5-9}$$

This method allows us to obtain the band structure $E_p\left(k_x, k_y\right)$ in the $k_x - k_y$ plane, using the following interaction procedure:

1. Obtain solutions for the energy and wave function from the Schrödinder equation (5-5).
2. Use the energy and wave functions to obtain the charge density.
3. Solving the Poison's equation (5-7) and obtain the new approach for the self-considered potential.
4. Test out for convergence. If the potential is converged then stop. Otherwise we continue with repeating the whole procedure.

The isoenergetic lines for a $9nm$ thick quantum well, in relaxed and strained structure, are plotted in *Figure 5.3* and *Figure 5.4*. The simulations were done for 60 harmonics

($p = 60$) in a grid of 200x200 points. *Figure 5.3* shows the first three subbands, which correspond to the first heavy, light and split-off subbands, respectively, however, *Figure 5.4* shows also the second three subbands, which are far away and are not included in further calculations.

As the valence-band structure in the quantum well and its dependence on the strain is already obtained, we are again interested in the calculation of the piezoresistive coefficients. From the *Figure 5.3*, it can be clearly seen that the stress has a minimal influence on the band edge energy levels. On the other hand, the isoenergetic line shapes are strongly deformed due to the stress. In contrast to the piezoresistive coefficients in the 3D p-type piezoresistors, both the longitudinal and transversal piezoresistive coefficients in the quantum well are determined by mass changes of the majority populated first heavy hole subband. Since the deformation of the isoenergetic lines shape for the heavy hole subband is significant, the calculated change of the effective mass is very large. As a result the magnitude of the p-type quantum well piezoresistive coefficients (*Table 5*) are bigger in comparison to the bulk p-type piezoresistive coefficients.

In summary, in this chapter a theory of the piezoresistive effect for the case of a two-dimensional electron (hole) gas was developed. Based on numerical calculations we can predict the behaviour of their piezoresistive coefficients with respect to the piezoresistor thickness. We found that the 2D piezoresistive coefficients in n-type silicon drop when the electron localisation increases. On the other hand, the increase of the hole localisation leads to enhancement of the p-type piezoresistive coefficients. Moreover, recently a technology which allows formation of ultra shallow (7nm) junctions [51 , 52] was demonstrated. Thus, it can be possible to produce a sensitive piezoresistive cantilever using the phenomena of the enhancement of the p-type 2D piezoresistive coefficients.

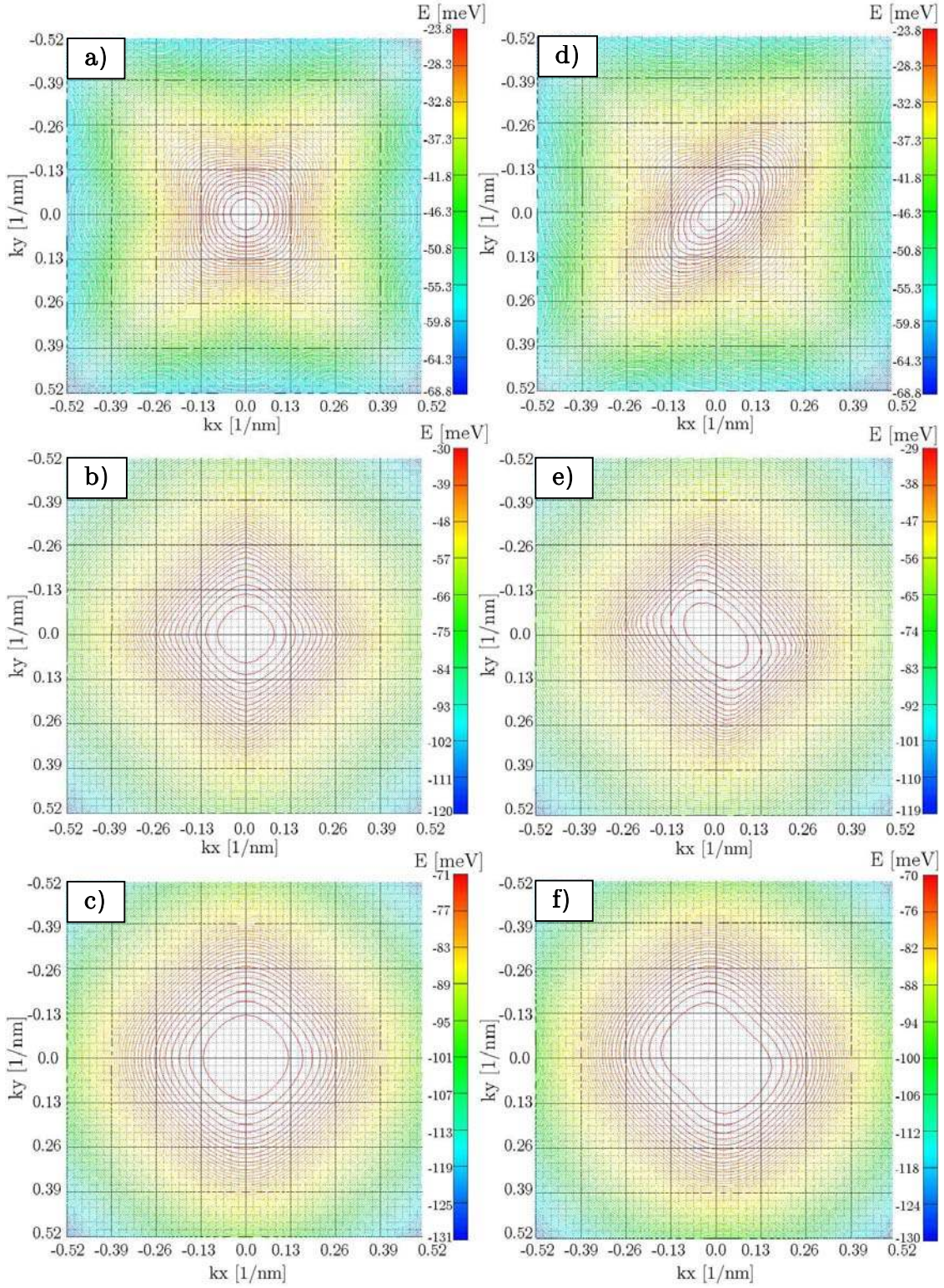

Figure 5.3 The isoenergetic lines related to the first three valence band subbands in a 9nm thick relaxed (a,b,c) and stressed quantum well (d,e,f).

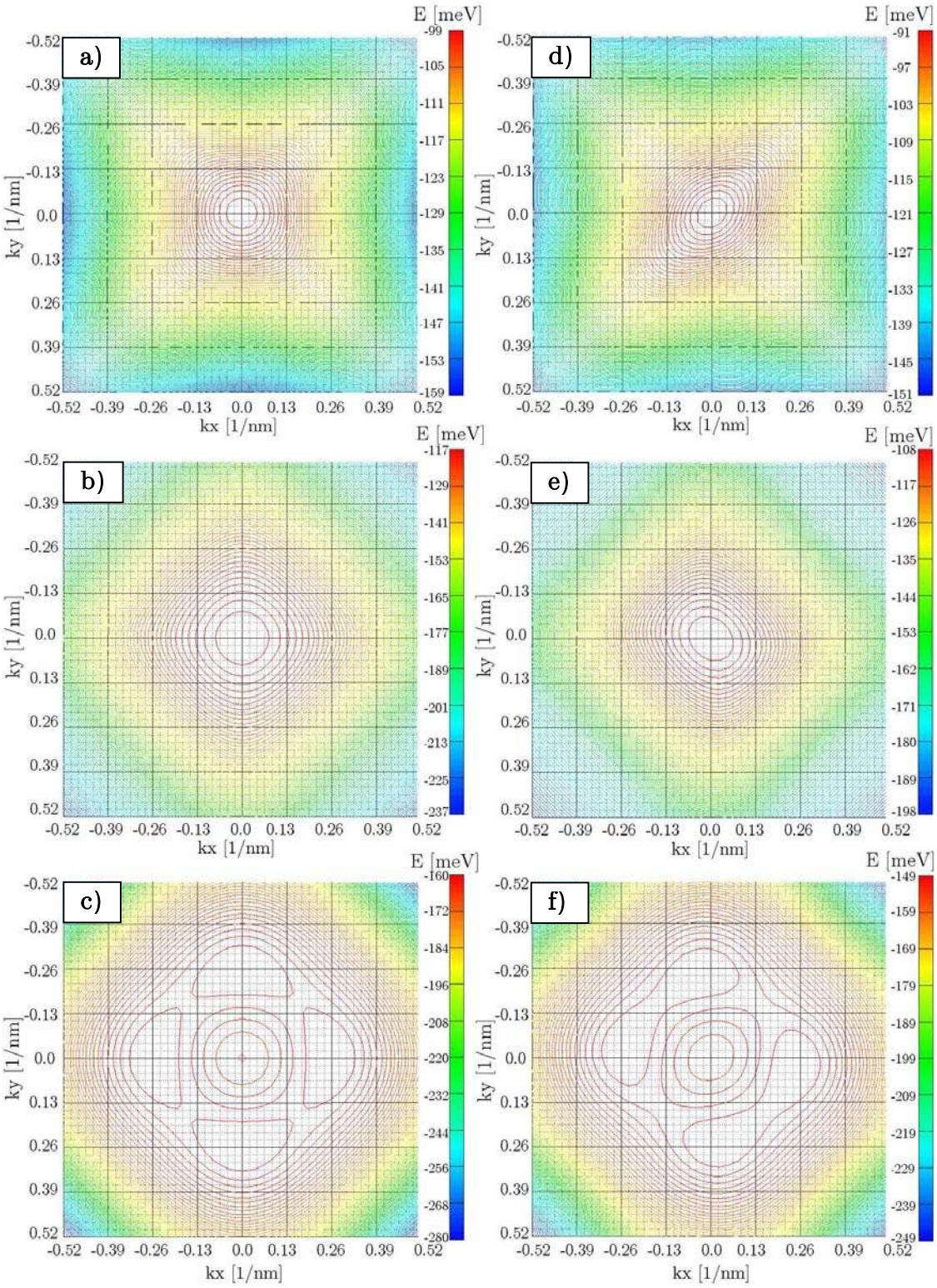

Figure 5.4 The isoenergetic lines related to the second three valence band subbands in a 9nm thick relaxed (a,b,c) and stressed (d,e,f) quantum well.

	Without stress	With 10^8Pa Stress in [110] direction
Heavy holes		
$m_{1hh(\parallel)}/m_0$	0.428	0.725
$m_{1hh(\perp)}/m_0$	0.428	0.277
$n_{1hh}/(n_{1hh}+n_{1lh})$	0.562	0.558
Light holes		
$m_{1lh(\parallel)}/m_0$	0.353	0.313
$m_{1lh(\perp)}/m_0$	0.353	0.462
$n_{1lh}/(n_{1hh}+n_{1lh})$	0.438	0.442
Piezoresistive coefficients		
π_l [Pa^{-1}]	$152x10^{-11}$ (bulk $72.9x10^{-11}$)	
π_t[Pa^{-1}]	$-163x10^{-11}$(bulk $-60.5x10^{-11}$)	

Table 5 Calculated piezoresistive coefficients in 9nm p-type SiO_2-Si-SiO_2 quantum wells at room temperature and acceptor concentration $n_n=10^{22}m^{-3}$.

Chapter 6
Thermo-Mechanical analysis of the cantilever beams

The key component of the atomic force microscope is a cantilever with an integrated tip and deflection sensor. The goal of this chapter is to describe the possibility of the integration of an additional actuator to the piezoresistive cantilever.

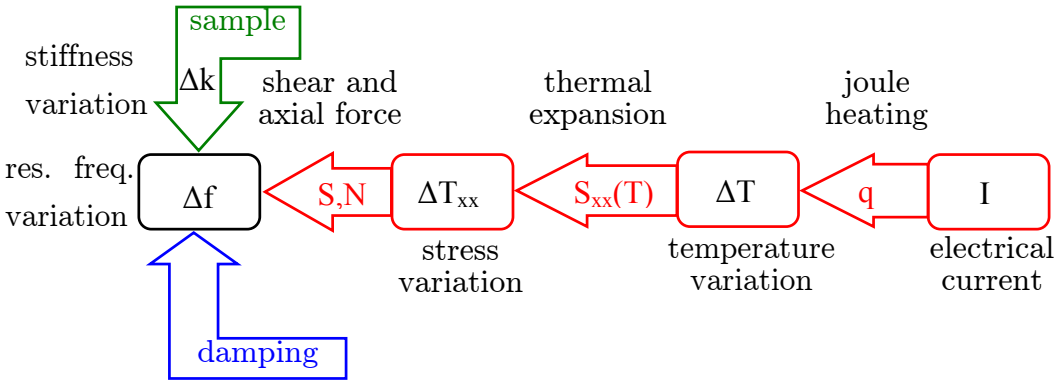

Figure 6.1 Hierarchy of the influenced cantilever resonance frequency shift by different mechanisms.

The analysis of the following mechanical cantilever parameters will be presented: stiffness constant, cantilever resonance frequency, as well as the mechanisms for inducing frequency shifts according to *Figure 6.1*. Such an analysis is necessary for the proper theoretical classification of the cantilever sensor with respect to fulfilment of the required measurement parameters. A basic theoretical model for a simple rectangular cantilever will be given. After that the actuation mechanism of the bimorph actuator will be discussed. Moreover a close form expression for the bending of the multi-layer composite cantilever, appropriate for numerical analysis will be demonstrated. A

thermal model was developed in order to predict the total electrical power necessary to drive the cantilever.

In order to optimise the piezoresistive sensitivity of the cantilever and to integrate the thermal actuator, some restrictions on the cantilever design are dictated. Such a cantilever has a more complex structure and geometry and the use of finite element modelling (FEM) in order to analyse those structures is necessary. The FEM simulations will be done with the programme ANSYS [53].

6.1 Quasi - Statical Beam deflection under axial and transverse load

In this section we will present the basic principles and equations, which describe the bending of a rectangular cantilever beam under axial and transversal load.

We consider the differential section of a cantilever beam as it is shown in *Figure 6.2*, where a single beam segment has been curved as a result of the acting forces. Our goal is to find the differential equation that governs the deflection of a beam under transversal and axial loading.

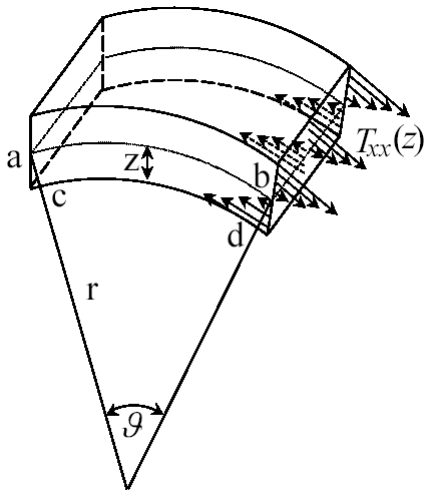

Figure 6.2 A differential segment of the bending beam.

The stain of segment cd, which has a distance z to the *'neutral plain'* segment ab, is defined like:

$$S_{xx} = \frac{cd - ab}{ab}. \tag{6-1}$$

The curvature of the beam for the small deflection is equal to the second derivative of the deflection. We therefore start by considering the radius of curvature r. From geometrical considerations we can express the length of the segments ab and cd through the radius of curvature r as:

$$ab = rd\vartheta, \tag{6-2}$$

and

$$cd = (r - z)\, d\vartheta. \tag{6-3}$$

As the strain is the difference between the length of the segment at the neural axis ab and the length of the segment cd at a position z, the strain of the segment cd becomes:

$$S_{xx} = -\frac{z}{r}. \tag{6-4}$$

The relation between stress and the strain is given by Hooke's law:

$$T_{xx} = YS_{xx} = -\frac{z}{r}Y. \tag{6-5}$$

Force equilibrium conditions can be applied to obtain the position of the neutral plane and its curvature radius r. Specifically the internal forces caused by the stress distribution acting over the cross section A have to balance the external applied force N_x so that the resultant force must be equal to zero:

$$N_x = \int_A T_{xx} dA. \tag{6-6}$$

Equilibrium conditions can be used to relate the applied external moment M, to the generated moment from the internal resulting stress. Specifically the internal moment, caused by the distributed stress over the cross section, has to balance the applied moment:

$$M = \int_A z T_{xx} dA = \int_A -\frac{Y z^2}{r} dA . \tag{6-7}$$

Defining the second moment of the area as:

$$I \equiv \int_A z^2 dA , \tag{6-8}$$

we finally come to the Euler-Bernoulli equation [54], which allows us to understand how the beam bends under different load moments:

$$\frac{\partial^2 \xi}{\partial x^2} \approx \frac{1}{r} = -\frac{M}{YI}, \tag{6-9}$$

where ξ is the beam deflection.

For the case of a cantilever with length l under the influence of a concentrated point force F exerted on a free end of the cantilever, the moment is $F(l-x)$. Using equation (6-9) we can express the deflection as:

$$\xi = \frac{F x^2 (3l - x)}{6YI} . \tag{6-10}$$

While many striking qualitative properties of the investigated sample are revealed in topographic and friction data, developing a fundamental understanding of these phenomena requires a quantitative analysis. Moreover, for biological samples, where the cantilever acting as a spring has to compensate forces under 1nN, the use of soft

cantilevers is necessary. Thus, whatever type of cantilever or detection method is employed, the measured deflection signals must be accurately calibrated to the load force. This requires, among other cantilever parameters, knowing the normal force constant of the cantilever, which describes its response due to the applied concentrated load. Unfortunately many of the commercial cantilevers have been formed in a V shape and their calibration is a rather complicated task. Experimentally the normal spring constant can be determined from the gravimetric method [55]. Theoretically the spring constant can be estimated using algebraic formulas or calculations based on numerical methods. Formulae for the force constants of simple rectangular-shaped microfabricated cantilevers beam are based on equation (6-10) when $x = l$. For a silicon ($Y = 170GPa$) cantilever with length $562\mu m$, width $220\mu m$ and thickness $4.7\mu m$ the spring constant is $5.47\,N/m$.

As we know for the maximal sensitivity, the piezoresistors should be placed to the place of maximal stress. The idea demonstrated firstly in [56 , 57] is that, with minimal changes on the rectangular cantilever shape we can control the position on the maximal stress with respect to the length position. With such a design now the four arms of the piezoresistive Wheatstone bridge (see Section 6.6) are under concentrated stress. Such cantilever has a shape, which is different from the rectangular one and the spring constant can't be estimated from the formulae valid for a simple rectangular shape. The spring constant has to be estimated from FEM calculations, which describe the cantilever deflection under concentrated normal load.

Figure 6.3 shows the deflection of the cantilever, with more complicated design, obtained from FEM simulations. As a result of these simulations we can calculate that the spring constant is 5N/m. Comparing with the spring constant of a rectangular cantilever we find that the modified cantilever is less stiff by about 10%. It can also be clearly seen that the maximal stress with respect to the placement of piezoresistros in z direction will occur at the surface. This dictates the necessity of the thin, surface placed, piezoresistors, the theory of which was discussed in the previous chapters.

The cantilever sensors are typically coated with a thin over-layer material (e.g. gold) to enhance laser reflectivity. This layer produces a surface stress and affects the mechanical properties of the cantilever. Furthermore, depending on the microfabrication process or operational environments, mechanical stress can also be

introduced into the cantilever. This is particularly true for silicon nitride cantilevers as they are produced by chemical vapour deposition resulting in an amorphous structure with uncertain stoichiometry and residual stress. Direct measurement of the stress, in the case of multilayer cantilever is difficult due to the inherent complexity. A statical analysis of the film stress measurements can be used, where the cantilever beam technique is performed [58] to detect changes in the cantilever curvature according the Stoney's theory [59].

The influence of the surface stress on the dynamical properties of the cantilever will be discussed in the next section, where the vibration theory for the cantilever beam in case of general force load will be considered.

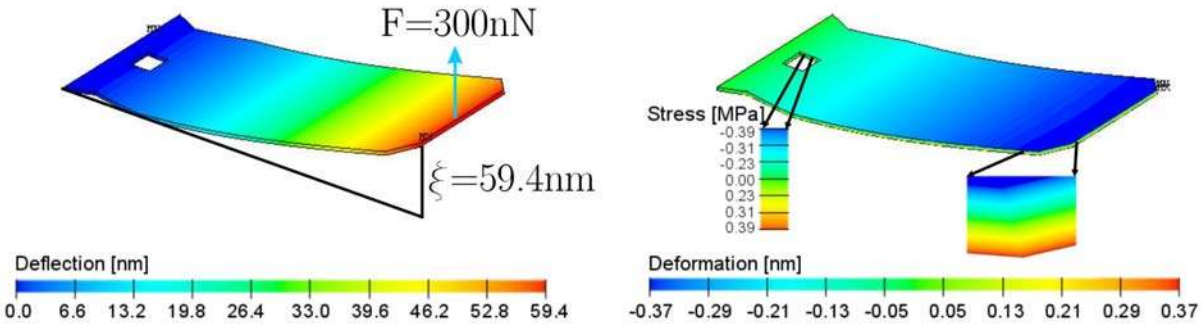

Figure 6.3 Deflection and deformation distributions obtained from the finite element method simulations.

6.2 Structural dynamics of the cantilever beam

The previous section has described the static (DC) AFM operation mode, where the tip-sample force is translated into a deflection and the surface topography is obtained as a function $z\left(x, y, F_{tip-sample} = const\right)$. In the following we will describe the dynamic (AC) operation modes, where the cantilever is intentionally vibrated. The measured quantities are the resonance frequency, the amplitude of oscillation and the phase shift. Any one of them can be used as a feedback parameter to track the surface topography.

Oscillations in AC measurements can take place in contact, noncontact and intermittent contact (known also as tapping mode [19]) - *Figure 6.4*. Today, two major detecting techniques have been developed in order to map the sample topography and potentials in noncontact and intermittent contact AC-SPM modes. In the first one, known as amplitude modulation (AM-[60]), the oscillation amplitude of the cantilever vibrating at or near free resonance frequency is used as a feedback parameter to track the changes of the force gradient at the sample surface. In the second one, known as frequency modulation (FM-[17]), the cantilever is kept oscillating at the resonance frequency with a fixed amplitude by applying a feedback through the oscillation control amplifier. The information parameter in the FM detection scheme is the instantaneous changes of the frequency due to the changing force gradient.

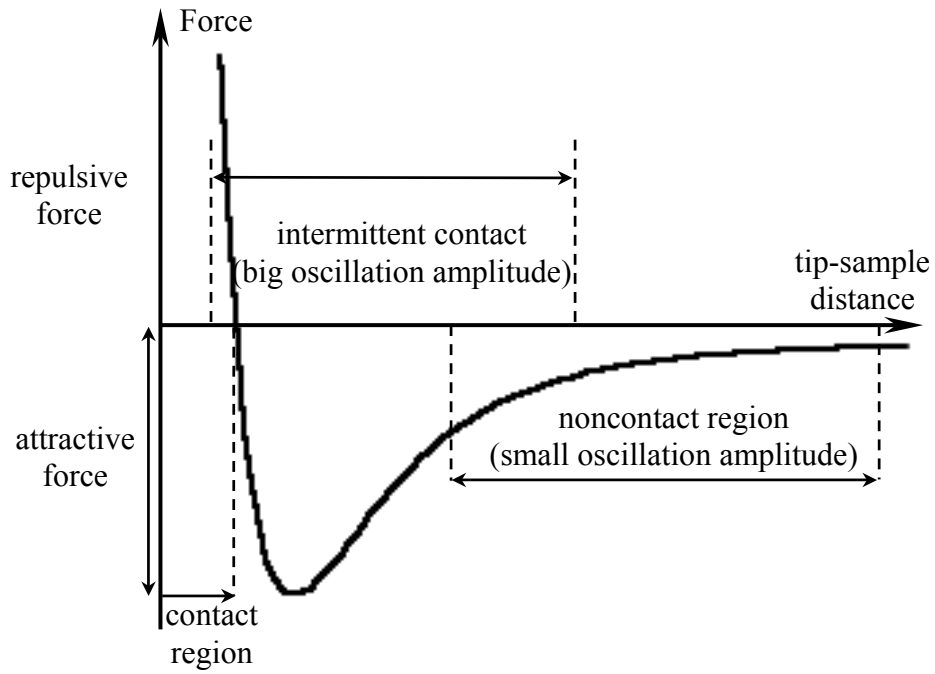

Figure 6.4 Schematic representation of the possible operation regimes of AC-AFM.

The main benefits of such resonant beam transducers are their potential for high lateral resolution and stability compared to DC measurements. The dynamic detection mode of the cantilever was preferred in our experimental arrangement due to its higher sensitivity compared to the static detection.

Compared to the detection of a quasistatic force in DC operation mode, the response of the cantilever in the AC mode is in any case more complex and deserves more detailed discussion. In most cases the treatment of the dynamical behaviour of the flexural cantilever beam is based on the simple theory presented in the previous section, where the periodically variable transversal load plays a major role for the driving force. The experimental results have indicated that the stress effects have significant influence on the resonance character, [61],[62], and sensitivity of the micro cantilever devices. As the stability of the resonance frequency is important, the theoretical understanding of stress influences is necessary in order to optimise the structural parameters and to improve the performance of the devices. The stress can arise from the thermal load as well as from residual strain. Also, due to operation in ambient conditions, the surface of the cantilever has the possibility to absorb molecules (chemisorption or physisorption), which can induce significant surface stress.

The applied correction to the usually exploiting beam vibration theory is connected with the axial force. There are two very different situations that we consider: First, the beam can be in tensile axial stress, which tends to keep the beam straight, and we expect that the stress makes the beam stiffer. Second, the beam can be in compressive stress, which tends to increase the deflection, i.e. it makes the beams less stiff.

Let's now consider the general case of the beam subject to a multiple load, *Figure 6.5*.

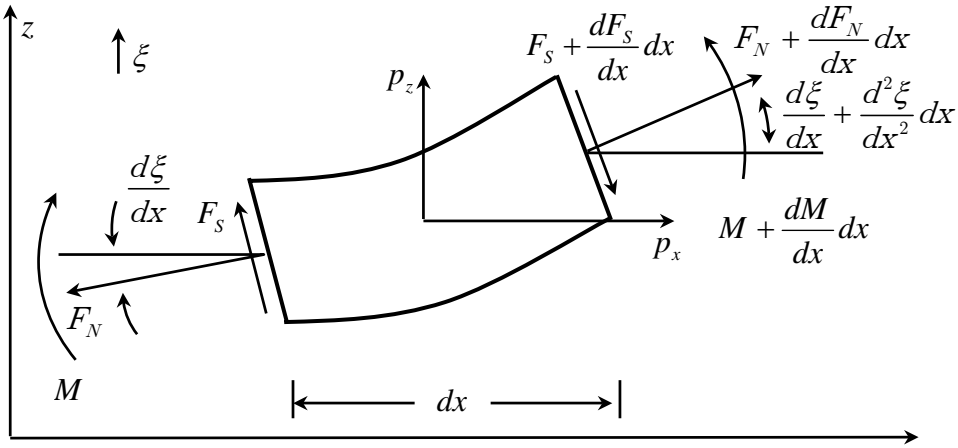

Figure 6.5 A General case of the cantilever beam load.

The concentrated force load contains transversal, F_S, and axial, F_N, components. The distributed applied load per unit length is decomposed into two components p_x and p_z. In order to obtain the equilibrium, the total force acting on the cantilever must be zero. The balance of the applied forces acting upon an infinitesimal beam element dx, projected on the x direction is:

$$\begin{gathered}\sum F_x = 0\ , \\ -F_N + \left(F_N + \frac{dF_N}{dx}dx\right) + p_x dx - F_S\frac{d\xi}{dx} + \left(F_S + \frac{dF_S}{dx}dx\right)\left(\frac{d\xi}{dx} + \frac{d^2\xi}{dx^2}dx\right) = 0\ .\end{gathered} \tag{6-11}$$

This leads to:

$$\frac{dF_N}{dx} = -p_x - \frac{d}{dx}\left(F_S\frac{d\xi}{dx}\right). \tag{6-12}$$

The force balance in the z direction is:

$$\begin{gathered}\sum F_z = 0\ , \\ -F_N\frac{d\xi}{dx} + \left(F_N + \frac{dF_N}{dx}dx\right)\left(\frac{d\xi}{dx} + \frac{d^2\xi}{dx^2}dx\right) + F_S - \left(F_S + \frac{dF_S}{dx}dx\right) + p_z dx = 0\ .\end{gathered} \tag{6-13}$$

This results to:

$$\frac{dF_S}{dx} = p_z + \frac{d}{dx}\left(F_N\frac{d\xi}{dx}\right). \tag{6-14}$$

For the balance of the bending moments around the y-axis we can write:

$$\begin{gathered}\sum M_y = 0\ , \\ -M + M + \frac{dM}{dx}dx + p_z dx\frac{dx}{2} - p_x dx\frac{d\xi}{dx}\frac{dx}{2} - \left(F_S + \frac{dF_S}{dx}dx\right)dx = 0\ .\end{gathered} \tag{6-15}$$

combining with the force balance equations we have:

$$\frac{dM}{dx} = F_S \,. \tag{6-16}$$

Considering the equations (6-9), (6-16) and (6-14) we receive the basic differential equation for the beam bending in case of general force load:

$$\frac{d^2}{dx^2}\left(YI\,\frac{d^2\xi}{dx^2}\right) - \frac{d}{dx}\left(F_N\,\frac{d\xi}{dx}\right) = p_z \,. \tag{6-17}$$

From the equations (6-9), (6-16) and (6-13) we arrive at an equation for the axial force distribution:

$$\frac{dF_N}{dx} = -p_x - \frac{d}{dx}\left(\frac{d\xi}{dx}\frac{d}{dx}\left(YI\,\frac{d^2\xi}{dx^2}\right)\right) \approx -p_x \,. \tag{6-18}$$

In order to find the response of the cantilever beam, both equations (6-18) and (6-17) have to be solved, respectively.

The dynamical deflection of the cantilever $\xi(x,t)$ can be described by the inhomogeneous differential equation (6-17) and the assumption that the distribution load p_z is expressed by the inertial force $-\rho A\partial_t^2\xi(x,t)$:

$$\rho A\,\frac{\partial^2}{\partial t^2}\xi(x,t) + YI\,\frac{\partial^4}{\partial x^4}\xi(x,t) - F_N\,\frac{\partial^2}{\partial x^2}\xi(x,t) = 0 \,, \tag{6-19}$$

where ρ is the density per unit length.

For the case of dumping, which will be considered later, the distributed force $f(x,\partial x/\partial t)$ has to be taken into account.

For determination of the eigenfrequencies of the cantilever (and characterising of our sensor) we have to solve the equation (6-19) by variable separation $\xi(x,t) = \upsilon(x)\,\tau(t)$:

$$\frac{\frac{d^2}{dt^2}\tau(t)}{\tau(t)} = -\frac{\frac{YI}{\rho A}\frac{d^4}{dx^4}\upsilon(x)}{\upsilon(x)} + \frac{\frac{F_N}{\rho A}\frac{d^2}{dx^2}\upsilon(x)}{\upsilon(x)}. \tag{6-20}$$

As the right hand side of equation (6-20) is independent from x, and the left hand side is independent from t, the equation is true for all values of x and t. Then both sides of the equation can be assumed to be equal to an arbitrary constant. Using a constant $-\omega^2$, the local and the time dependent part of the equation (6-20) can be separated into two independent differential equations:

$$\frac{d^2}{dt^2}\tau(t) + \omega^2\tau(t) = 0, \tag{6-21}$$

and

$$\frac{d^4}{dx^4}v(x) - \frac{F_N}{YI}\frac{d^2}{dx^2}v(x) - \frac{\rho A}{YI}\omega^2 v(x) = 0. \tag{6-22}$$

The equation (6-21) represents the harmonic oscillator equation with radial frequency ω and has the solution $\tau(t) = e^{i\omega t}$.

If we define $k^4 \equiv \omega^2 \rho A/YI$ and $\beta = F_N/2YI$ and assume a trial solution $\upsilon(x) = Ce^{\lambda x}$ for the equation (6-22), we lead to an equation for λ:

$$\lambda^4 - 2\beta\lambda^2 - k^4 = 0. \tag{6-23}$$

The general solution (6-22) can be found in the following forms:

$$v(x) = C_1 e^{ik_1 x} + C_2 e^{-ik_1 x} + C_3 e^{k_2 x} + C_4 e^{-k_2 x}, \tag{6-24}$$

where $\pm ik_1 \equiv \pm i\sqrt{\sqrt{\beta^2 + k^4} + \beta}$ and $\pm k_2 \equiv \pm\sqrt{\sqrt{\beta^2 + k^4} - \beta}$ are solutions of the equation (6-23).

The equation (6-24) presents the general solution of the fourth-order differential equation. The exact shape function can be found considering the boundary conditions.

As many factors can influence the cantilever operation, different boundary conditions need to be assumed. The boundary conditions however, normally are only an approximation to the real practical problems. Examples of typical boundary conditions are presented in *Table 6*.

At the fixed end we found that the deflection and slope must be equal to zero. The other end of the cantilever can have different boundary conditions. Usually in models presented in the literature, a free end, where the bending moment M and shear force F_S are considered to be equal to zero, is discussed. The nonuniform mass distribution due to the tip can be approximated by the inertia load [63].

	Deflection component $\upsilon(x)$	Slope component $\frac{\partial \upsilon}{\partial x}$	Moment M component $\frac{\partial^2 \upsilon}{\partial x^2}$	Shear F_S component $\frac{\partial^3 \upsilon}{\partial x^3}$
Fixed	$\upsilon = 0$	$\frac{\partial \upsilon}{\partial x} = 0$		
Free $M = 0 \quad F_S = 0$			$YI\frac{\partial^2 \upsilon}{\partial x^2} = 0$	$\frac{\partial^3 \upsilon}{\partial x^3} = \frac{F_N}{YI}\frac{\partial \upsilon}{\partial x}$
Inertia load $F_S = m\frac{\partial^2 \upsilon}{\partial t^2}$			$YI\frac{\partial^2 \upsilon}{\partial x^2} = 0$	$\frac{\partial^3 \upsilon}{\partial x^3} = \frac{F_N}{YI}\frac{\partial \upsilon}{\partial x} + \frac{F_S}{YI}$
Spring load $F_S = -\kappa\upsilon$			$YI\frac{\partial^2 \upsilon}{\partial x^2} = 0$	$\frac{\partial^3 \upsilon}{\partial x^3} = \frac{F_N}{YI}\frac{\partial \upsilon}{\partial x} + \frac{F_S}{YI}$
Simply supported	$\upsilon = 0$		$YI\frac{\partial^2 \upsilon}{\partial x^2} = 0$	

Table 6 The possible boundary conditions for the cantilever end.

In the non-contact AFM the long-range attractive forces between cantilever tip and the sample surface are derived from the Van-der-Waals interaction [64]. The influence of this interaction onto the cantilever vibration can be modelled if we consider at the

cantilever end a spring, which can be also nonlinear [65]. This means that we have spring load boundary conditions.

The influence of the axial force load into the resonance frequency on microbridges, fixed-fixed boundary conditions, has been discussed in [66].

In the frame of this work we will consider an axially force load cantilever beam with fixed-free end boundary conditions. Applying to the general solution, given by (6-24), fixed-free end boundary conditions (see *Table 6*) we get a homogeneous system of four linear equations for the unknowns C_1, C_2, C_3 and C_4. This system has a nontrivial solution only if the wave numbers $(kl)_n$ of the cantilever are solutions of the following equation:

$$\frac{k_1^2\cos(k_2 l)+k_2^2\cosh(k_1 l)}{k_2\sin(k_2 l)+k_1\sinh(k_1 l)} = -\frac{k_1^2 k_2\sin(k_2 l)-k_1 k_2^2\sinh(k_1 l)}{k_2^2\cos(k_2 l)+k_1^2\cosh(k_1 l)}. \qquad (6\text{-}25)$$

The solutions $(kl)_n$ of this equation, which can be calculated numerically, depend on the dimensionless axial force βl^2. Using the definition of the wave numbers the resonance frequency depends on the axial force like:

$$\omega = \frac{(kl)^2}{l^2}\sqrt{\frac{YI}{\rho A}} \qquad (6\text{-}26)$$

The above equation can be used to calculate the resonance frequency dependence on the axial force only in the case of a rectangular cantilever. Therefore, we will follow a procedure in which all calculations are performed in the FEM tool and which could be applied to other structures with non-trivial geometries, even with multiple materials. An example of the natural frequencies and mode shapes of a nonuniform microcantilever beam is presented in *Figure 6.6*. Resonance frequencies were computed as eigen frequencies of the undamped cantilever. *Figure 6.6a,b and c* show the eigen frequencies and shapes of the first three transverse vibration modes. The simulations show the existence of a shear vibration modus *Figure 6.6*d with a frequency near to the second transverse vibration modus *Figure 6.6*b. Usually, share vibration modes

presented in *Figure 6.6*-d,e and f does not appear in the cantilever spectrum. This is related to the symmetry of the cantilever beam. Moreover the existence of non vibrating points at higher vibration modes make detection of the cantilever bending through a reflecting laser beam difficult.

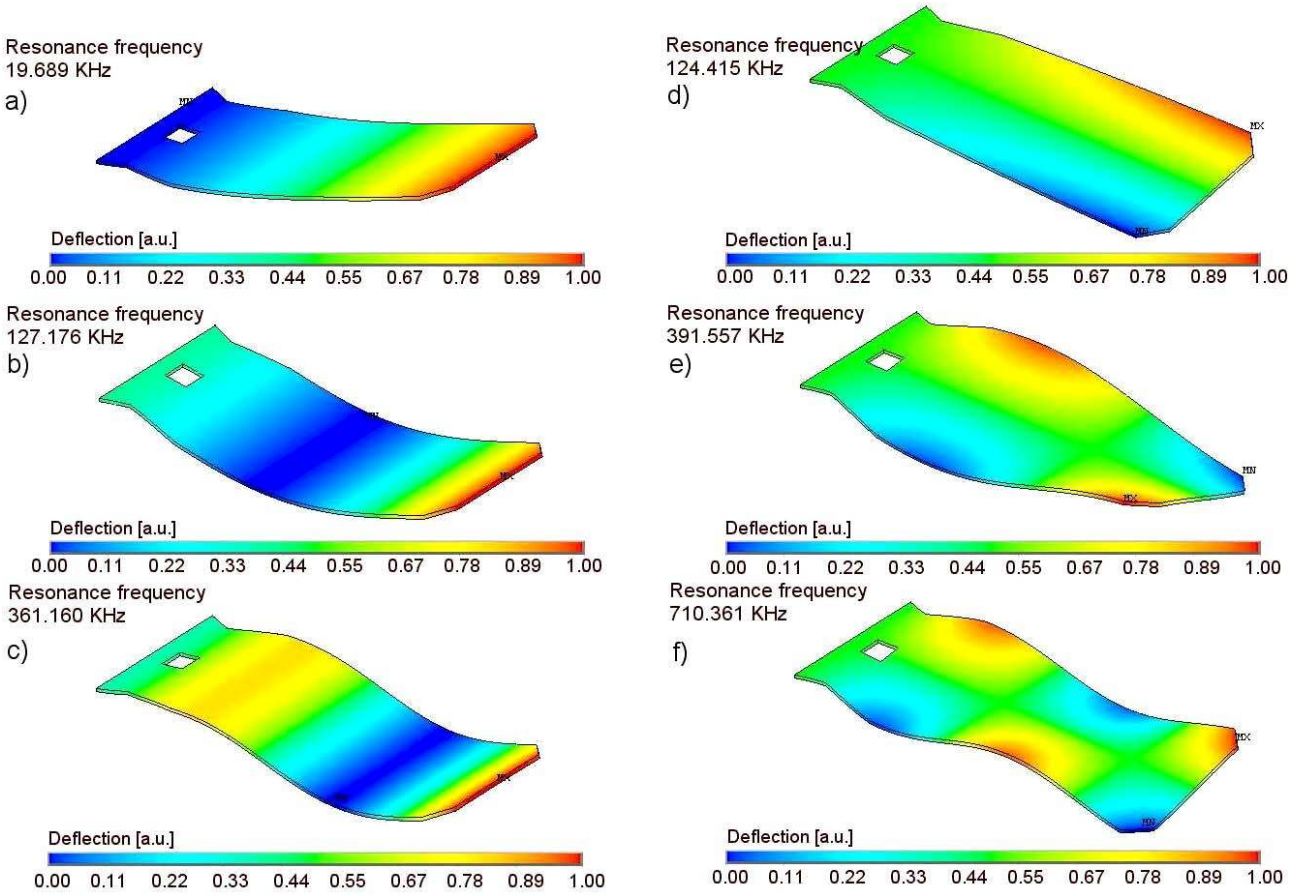

Figure 6.6 The eigen oscillation modes of the cantilever.

The effect of constant axial tensile (*Figure 6.7a*) and compressive (*Figure 6.7e*) force load on the natural frequencies and mode shapes of the first three transverse vibration modes is discussed below. *Figure 6.7b, c and d* show the influence of tensile axial force load, while *Figure 6.7f, g and h* show the influence of compressive axial force load. This analysis was performed with the help of the frequency modal analysis just after the static solution was obtained for each axial load. It can clearly be seen that the resonance frequency of the cantilever depends strongly on the applied axial force. Based

on such principles Harley and Kenny [67 , 68] demonstrate very sensitive devices capable of detection extremely low forces (in range of aN). On the other hand the analysis provided above shows the inapplicability (as the image has to be obtained for the fixed frequency shift) of the FM detection scheme in case of bimorph actuating cantilever, where an axial force exist - see also section 6.4.

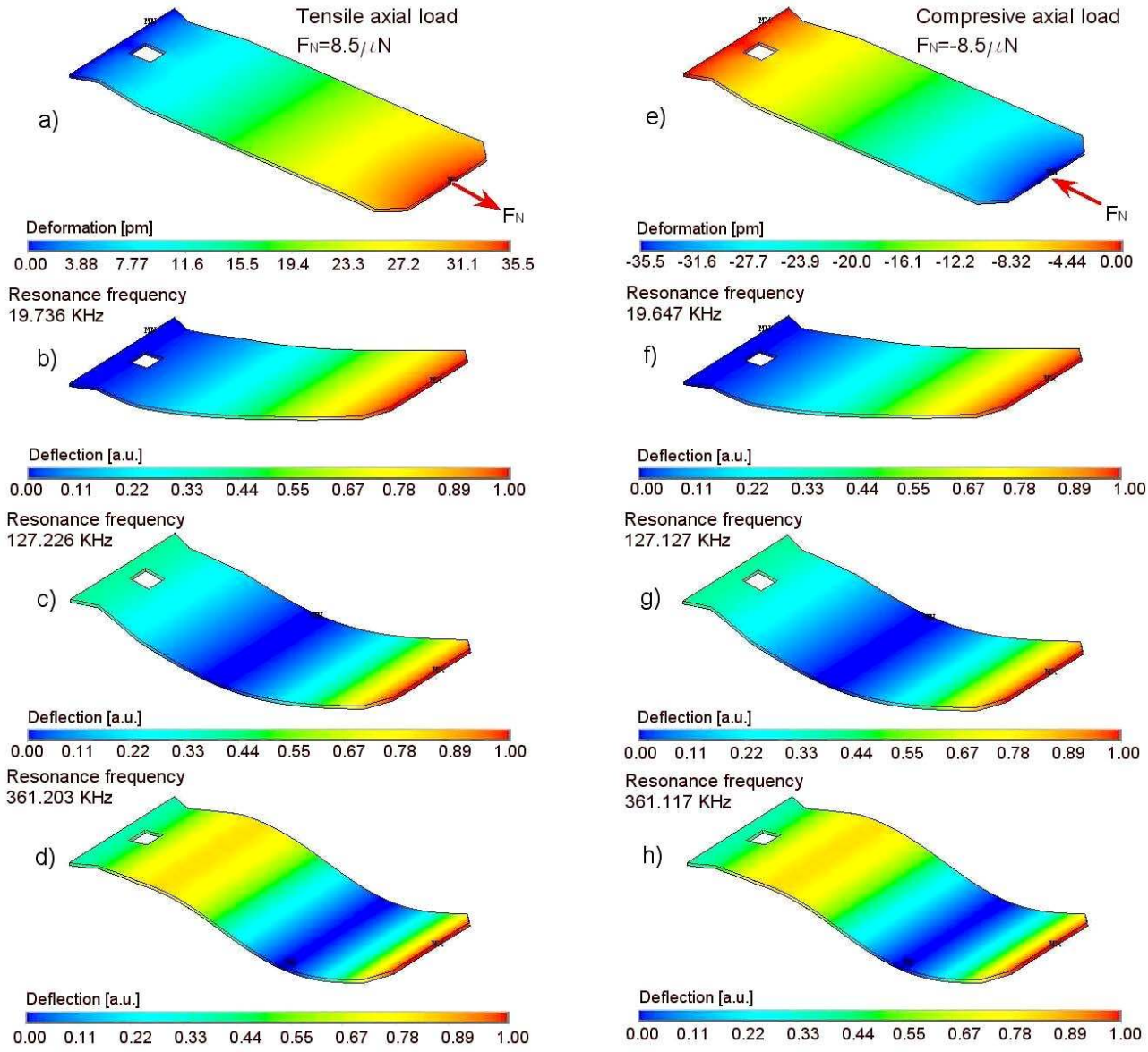

Figure 6.7 Influence of the axial stress on the eigen oscillation frequency of the first three transversal modes of the cantilever.

6.3 Multi-modes analysis of the periodic force driven cantilever with damping

In the previous section was discussed the free vibration of the cantilever, where the total energy remains constant during the whole time. However, in practice the stored mechanical energy in the cantilever always gets converted into heat due to dissipative forces. The process of energy dissipation is called damping. With respect to the TM-AFM, where the tip strikes the sample surface, the energy dissipation is involved. Moreover, TM-AFM allows locally mapping of this process and obtaining information of the material properties in the nanometer scale.

Therefore in this section the influence of damping over the parameters of the TM-AFM imaging will be discussed.

The dissipation term is usually included after the variable separation into equation (6-21) or into equivalent mass-spring system. Such model can be applied if the dissipations are homogeneous. The damping of vibrating AFM cantilevers is caused by: i) internal losses in the cantilever beam and losses to any surrounding fluid in which the cantilever vibrates and ii) losses due to interaction of the cantilever tip and the sample surface. Therefore, the damping force in general is inhomogeneous, which lead to the coupling between the cantilever eigen modes. Below we will demonstrate the basic multi-mode method, which can be applied in the case of inhomogeneous energy dissipation.

In the multi-mode analysis the dissipation term is introduced before the equation of motion of the total system is decomposed. The equation of motion of the cantilever beam subjected to time varying forces (concentrated $F(x_f,t)$ and distributed $p(x,t)$) in presence of damping $\gamma(x)$ is:

$$\rho A\frac{\partial^2}{\partial t^2}\xi(x,t)+YI\frac{\partial^4}{\partial x^4}\xi(x,t)-\gamma(x)\frac{\partial}{\partial t}\xi(x,t)=p(x,t)+F(x_f,t). \qquad (6\text{-}27)$$

To solve the above equation, the deflection $\xi(x,t)$ is expanded as a superposition of basic functions:

$$\xi(x,t) = \sum_{m=1}^{\infty} \upsilon_m(x)\ \tau_m(t), \tag{6-28}$$

where the basic functions $\upsilon_m(x)$ are the solutions of the free vibrating cantilever-equation (6-22). The displacements $\upsilon_m(x)$ are components of an orthogonal complete system. Substituting the equation (6-28) into the equation of motion (6-27), multiplying by $\upsilon_n(x)$ and integrating over the cantilever length we receive the following equation:

$$m_n \partial_t^2 \tau_n(t) + \sum_m \gamma_{nm} \partial_t \tau_m(t) + \kappa_n \tau_n(t) = p_n(t) + F_n(t), \tag{6-29}$$

where, [69], the n-th modal mass, spring constant, damping coefficient, distributed force and force are defined respectively as:

$$m_n \equiv \rho A \int_0^l \upsilon_n^2(x)\,dx\,, \tag{6-30}$$

$$\kappa_n \equiv YI \int_0^l \left(\partial_x^2 \upsilon_n(x)\right)^2 dx\,, \tag{6-31}$$

$$\gamma_{mn} \equiv \int_0^l \gamma(x)\,\upsilon_n(x)\,\upsilon_m(x)\,dx\,, \tag{6-32}$$

$$p_n(t) \equiv \int_0^l p(x,t)\,\upsilon_n(x)\,dx\,, \tag{6-33}$$

$$F_n(t) = \upsilon_n(x_f)\,F(t)\,. \tag{6-34}$$

In such way (6-29) present a system of equations, which describes the coupling between the cantilever eigen modes due to the damping.

Below we will consider the case of homogeneous dissipation. As a result, the solutions of the equation (6-29) are not mode coupled. Thus, we can solve the n-th equation individually, for example, knowing its impulse response behaviour. The impulse response $h(t)$ is defined as response of the cantilever to the Delta function $\delta(t)$ driving force. In physics the impulse response is usually called Green's function. When

we know the impulse response of the cantilever we can calculate its response for each driving signal according to the convolution theorem:

$$\tau_n(t) = \int_{-\infty}^{\infty} h_n(t-t')F_n(t')\,dt'. \tag{6-35}$$

The impulse response is taken like the Green's function [70] for differential equation of the driven damped harmonic oscillator:

$$h_n(t) = \Theta(t-t')\left[-\frac{e^{-i(t-t')\omega_{n+}} - e^{-i(t-t')\omega_{n-}}}{i(\omega_{n+}-\omega_{n-})}\right] = \Theta(t-t')\frac{e^{-\gamma_n t/2m_n}\sin(\omega_{nd}t)}{m\omega_{nd}}, \tag{6-36}$$

where

$$\omega_{n\pm} = -\frac{i\gamma_n}{2m_n} \pm \omega_{nd}\ ;\quad \omega_{nd} = \sqrt{\omega_n^2 - {\gamma_n}^2/2m_n}\ ;\quad \omega_n = \sqrt{\kappa_n/m_n}\,. \tag{6-37}$$

Introducing equation (6-36) into equation (6-35), for the periodically driven force $F_{nd} = f_n\cos(\omega t)$, we obtain the solution:

$$\tau_n(t) = A_n\cos(\omega t - \theta_n) + B_n e^{-\gamma_n t/2m_n}\cos(\omega_{nd}t + \varphi_n), \tag{6-38}$$

where

$$A_n = \frac{f_n/m_n}{\sqrt{\left(\omega_n^2-\omega^2\right)^2 + \left(\omega\gamma_n/m_n\right)^2}};\quad \tan(\theta_n) = \frac{\omega\gamma_n}{\left(\omega_n^2-\omega^2\right)m_n}. \tag{6-39}$$

The above obtained results can be used to calculate the cantilever end amplitude behaviour $a_n(L) = \upsilon_n(l)A_n$ as for a classical damped harmonic oscillator, driven with periodically force $F_d = f\cos(\omega t)$, if a mode dependent mass $m_n^{cl} = m_n/\nu_n(l)^2$, spring constant $\kappa_n^{cl} = \kappa_n/\nu_n(l)^2$ and damping coefficient $\gamma_n^{cl} = \gamma_n/\nu_n(l)^2$ are introduced.

The solution has a steady part and a transient term. Initially, both motions are important, however after a time interval $2m_n/\gamma_n$ the transient term is reduced by a factor $1/e$. The resulting motion will be dominated by the steady part of the solution, which has a harmonic behaviour with a phase lag with respect to the excitation force. When the derivative of the amplitude with respect to ω/ω_n is equal to zero, we found that the amplitude has a maximum value at frequency ω_{nd}. The damping coefficient γ_n determines the cantilever quality factor $Q = m_n\omega_n/\gamma_n$. From equations (6-38) and (6-39) we can see that, cantilevers with high Q (i.e. small γ_n) factor gives a higher sensitivity, but in the other hand the cantilever's response with respect to the feedback system, due to the transient term, will be reduced. In such way the scan speed of TM-AFM is limited by the speed of the feedback loop that maintains constant tapping amplitude.

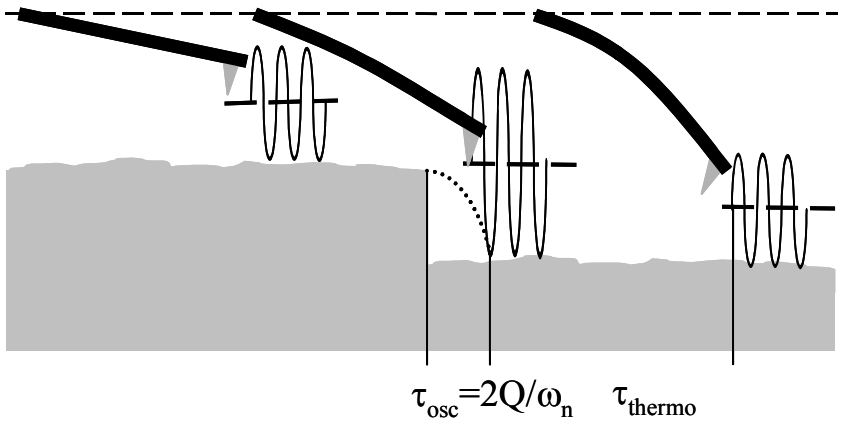

Figure 6.8 Schematic representation of the TM-AFM imaging performed with bimorph actuating cantilever.

Figure 6.8 shows a schematic view of the TM-AFM, when the cantilever scans over a downward step. Such vertical steps provide a worst-case scenario limit to scanning speed. It can be seen the existing of two characteristic times: The first one τ_{osc}, as was already discussed, is connected with the time needed for the amplitude stabilization. The second one τ_{thermo} depends on the time needed for the bimorph actuating cantilever to follow the profile and will be investigated also in this chapter - 6.5.

Sulchek *et al* [71 , 72] has proposed the feedback with active damping control, which allows decreasing of τ_{osc} and increasing of the imagining speed. In this work (see

chapter 8.3) is used another method for reducing the time constant $\tau_{osc} = 2Q/\omega_n$. The idea is based on increasing of the cantilever operation frequency. As we will see the cantilever geometry is fixed to thin and long cantilevers, which have low resonance frequency, thus the only way to use high frequency operation is to benefit from existing of the higher eigen modes at which the cantilever can vibrate. Furthermore, the phase angle changes will be used to image the sample surface. The image obtained in such way is called phase contrast or phase contrast image. This image often provides significantly more contrast than the topographic image and has been shown to be sensitive to material surface properties, such as stiffness, viscoelasticity, and chemical composition. Moreover, phase imaging in the higher eigen modes has an enhanced contrast [73].

In general, changes in phase angle during scanning are related to energy dissipation during tip-sample interaction and can be due to changes in topography, tip-sample molecular interactions, deformation at the tip-sample contact and even experimental conditions. Depending on the operating conditions, different levels of tapping force might be required to produce accurate, reproducible images on different samples.

Further we will introduce the concept of transfer function, which will be used for the force sensitivity analysis (see chapter 7.2). Applying the Fourier transform to equation (6-29) will lead to a solution in the frequency domain:

$$\tilde{\tau}_n(\omega) = H_n(\omega)\tilde{F}_n(\omega), \tag{6-40}$$

where the transfer function, $H(\omega)$, is equal to the Fourier transform of the impulse response $h(t)$ and is defined as:

$$H_n(\omega) = \frac{1}{-m_n\omega^2 + i\gamma_n\omega + k_n}. \tag{6-41}$$

From the above analysis it can be seen that the cantilever oscillations are determined by the resonance frequency, amplitude and the phase, which depend on environment conditions and on the tip-sample interactions. Thus observing any of these three oscillations parameters during the sample scanning give us the possibility of surface

roughness mapping. The resonance frequency, the amplitude and the phase are also mode dependent according to equations (6-30) to (6-34).

6.4 Multi-layer cantilever beam with an embedded thermal actuator

As was pointed out in the previous section the scanning speed of the TM-AFM is limited due to the actuation time constant of the piezotube feedback loop that keeps the tapping amplitude constant. This limitation can be overcome by reducing the size of the system and consequently its inertia. In this manner it is possible to significantly increase the scanning speed. Furthermore, by increasing the sensitivity of the tapping probe the signal to noise ratio can be improved thus leading to a further reduction in the time constant needed for stable feedback loop operation. Two issues are considered as fundamentals in the realization of this idea: i) integration of the piezoresistive read-out to the cantilever (see section 6.6) and ii) actuator integration for converting the signal from electrical to mechanical domain.

In the present and following section will be considered the aspects of actuator integration.

Discussions about bending beams are usually limited: i) to beams with at least one longitudinal plane of symmetry with the load applied in the plane of symmetry or ii) to symmetrical beams composed of longitudinal elements of similar material or iii) to initially straight beams with constant cross section and longitudinal elements of the same length. If any of these assumptions is violated, the simple equations, which describe the beam bending stress and strain, are no longer applicable. This section discusses multi-layers cantilevers, which provide a possibility of actuation due to the different respond to some stimulus such as magnetic field, an electrical field, a vapour or light. In particular we will discuss the thermal bimorph as a driving mechanism of our cantilever.

Actuators based on the thermal bimorph effect are favourable due to their large actuation range and fabrication simplicity due to simple planar processes realized by

metal deposition techniques. The electro-thermal actuation can be used to follow the topography of the sample for measurements in the constant force mode and to excite the cantilevers at their resonance frequency for dynamic mode imaging. Thermal bimorph actuators can be placed at different locations along the length of the cantilever. An aluminium heating resistor can form the actuators and in such a way the dissipated heat in the resistors will increase the temperature. As a result, due to the difference in thermal expansion coefficients of the silicon, metal and oxide layers, the increasing temperature leads to a deflection of the cantilevers. The efficiency of such actuation can be made high enough, by optimising the bending analysis of the multi-layer cantilever.

As in section 6.1, the predictions of the cantilever beam tip deflection will be found by utilizing the Euler-Bernoulli method. In the case of a multi-layer beam, the equation (6-5) of the stress component of the i-th layer has to be rewritten as:

$$T_{xx}{}^{i} = Y_i S_{xx}{}^{i} = Y_i \left(S_{xx}{}^{0} - S_{xx}{}^{i-ext} + \frac{z_i - z_o}{r} \right). \qquad (6\text{-}42)$$

This equation can be understood very well if we consider in more detail the steps, which have to be followed in order to ensure a stable beam made from an individual layer:

1) Let us assume that we have a few individual layers with equal length, but different widths and thicknesses.
2) Let some external influence induce a different strain $S_{xx}{}^{i-ext}$ to the layers.
3) In order to construct a multi-layer beam we have to ensure again the equal length of all layers. This can be done if we apply an additional stress $-Y_i S_{xx}{}^{i-ext}$ to every i-th layer. By this way all layers have again same length, but now the resultant force will not be zero. In order to ensure the condition of zero summing force, we have to add an additional unknown strain $S_{xx}{}^{0}$ to every layer.
4) Such composite will be unstable and will tend to bend in order to ensure zero resultant moment. The bending will induce an additional strain $(z_0 - z_i)/r$ to the summary strain.

Introducing equation (6-42) into equations (6-6) and (6-7) will lead us to the following system for the bending radius and strain at the neutral plane:

$$\begin{bmatrix} (Y)_{tot} & (Yz)_{tot} \\ (Yz)_{tot} & (YI)_{tot} \end{bmatrix} \begin{Bmatrix} S_{xx}{}^{0} \\ 1/r \end{Bmatrix} = \begin{Bmatrix} F_{N\Lambda} + F_N \\ M_\Lambda + M \end{Bmatrix}, \tag{6-43}$$

where:

$$(Y)_{tot} \equiv \int_A Y(z)dA\,, \tag{6-44}$$

$$(Yz)_{tot} \equiv \int_A Y(z)zdA\,, \tag{6-45}$$

$$(YI)_{tot} \equiv \int_A Y(z)z^2dA\,, \tag{6-46}$$

$$F_{N\Lambda} \equiv \int_A Y(z)S_{xx}{}^{ext}(z)dA\,, \tag{6-47}$$

$$M_\Lambda \equiv \int_A Y(z)S_{xx}{}^{ext}(z)zdA\,. \tag{6-48}$$

As can be seen from the upper equations the Euler-Bernoulli method has two advantages: i) It simplifies the analysis of composite beams with different thicknesses and mechanical properties. This is accomplished by introducing $(Y)_{tot}$ and an $(YI)_{tot}$, which respectively play a role of effective Young's modulus and effective moment of inertia about the chosen bending axis. This axis can be chosen based on convenience. For this design, the axis was chosen to lie at the bottom layer. ii) The choose of the bending axis is arbitrary, i.e. no need to know the neutral axis of the beam to calculate the bending curvature for the general case. In addition to $(Y)_{tot}$ and $(YI)_{tot}$, the Euler-Bernoulli method calculates a coupling term, $(Yz)_{tot}$. This term couples the moment calculated from the arbitrary axis to neutral axis. It also couples the extensional force to the curvature of the beam about the neutral axis. When the arbitrary bending axis and the neutral axis coincide, taking into account step 3 from the algorithm of composite beam construction, $(Yz)_{tot} = 0$. This equation can be used for investigation of the neutral axis position. It has to be noted that for multi-layer

beam the neutral axis does not, in general, correspond to the axis at which the cantilever is unstrained. Instead, the neutral axis merely indicates the position in the composite beam about which the coupling term disappears.

This method is also suitable to analyse the tip deflection due to residual stress after the device realisation. This can be done if we translate, for each beam layer, the residual stress to force and moment terms. Than so obtained force and moment terms have to be substituted into the equation (6-43). Thus we can determine the strain at the neutral axis and the beam curvature.

For the numerical analysis of the external induced bending, we have to find a close form expression for the curvature of the multi-layer cantilever. In the case when there are no external loads applied at the tip of the cantilever beam, the solutions of the equation (6-43) give us the following expressions for the curvature of the beam and the strain at the neutral plane:

$$\frac{1}{r} = \frac{M_\Lambda (Y)_{tot} - F_{N\Lambda} (Yz)_{tot}}{(Y)_{tot} (YI)_{tot} - (Yz)_{tot}^{\ 2}}, \tag{6-49}$$

$$S_{xx}^{\ 0} = \frac{F_{N\Lambda}}{(Y)_{tot}}. \tag{6-50}$$

In the case of thermal actuation the induced strain $S_{xx}^{\ i-ext}$ is $\alpha_i \Delta T_i$ where α is the coefficient of thermal expansion. The loading force and moment are determined by the thermally induced force $F_{N\Lambda}$ and moment M_Λ according equations (6-47) and (6-48), respectively.

As we get acceptable equations for numerical investigation, it is essential to apply an optimisation analysis to the actuation possibility of the multi-layer cantilever. The basic point of such optimisation will be a deflection of the cantilever end $\xi = l^2/2r$ as a function of the material properties and geometry. In the real system the material of one layer of the bimorph cantilever is fixed by technological constrains. In our case this is the silicon layer. The second material has to be chosen with possible different coefficient of thermal expansion with respect to the first material. For determination we will look for material with bigger coefficient of thermal expansion. One of the possible materials is aluminium, which is also compatible with the MEMS technology.

After the determination of the materials, it is necessary to obtain an optimum with respect to the geometry. The results of the geometry optimisation analysis are presented in *Figure 6.9*.

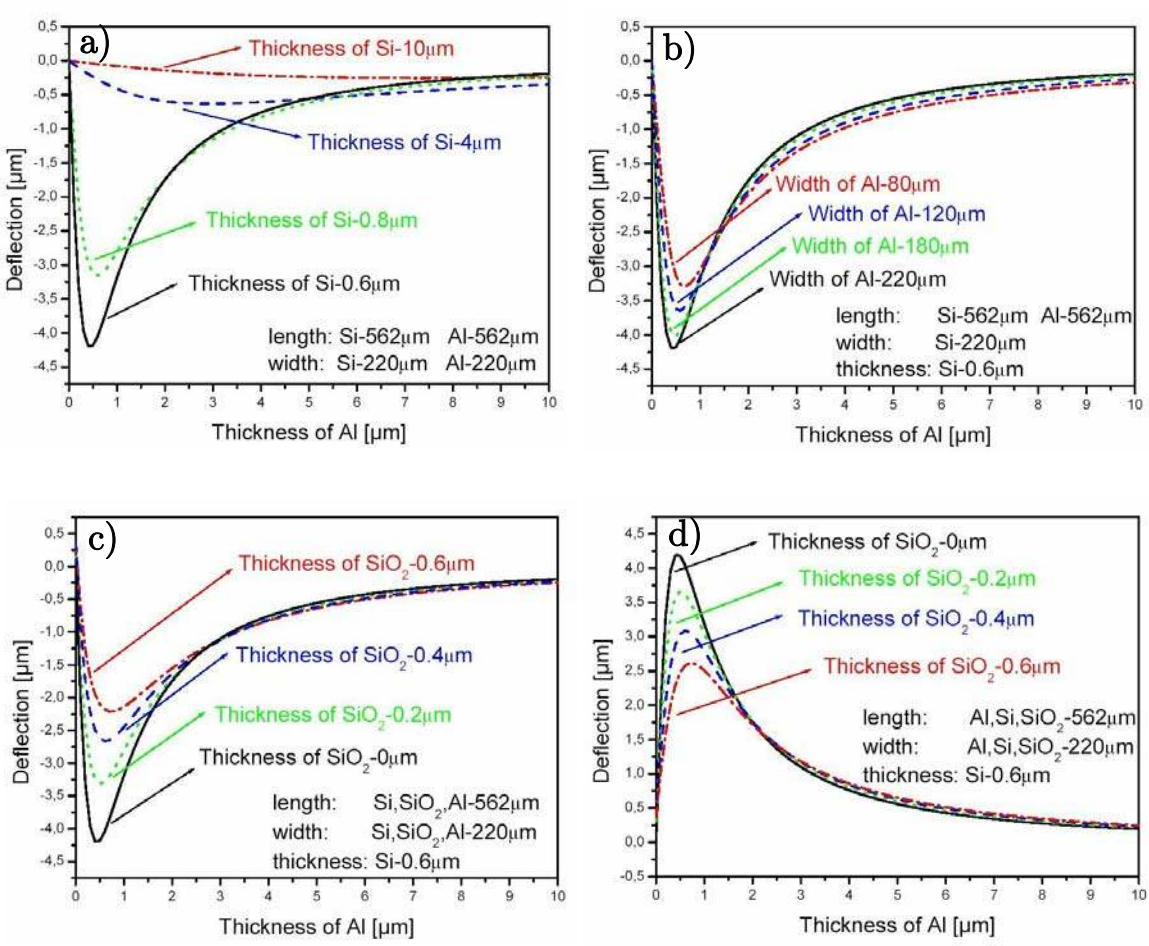

Figure 6.9 Bimorph cantilever deflection efficiency vs. the thickness at 1K temperature increasing.

From *Figure 6.9a* it can be seen that the induced response from the uniform temperature increase by 1K vanishes for thin aluminium layer, after that it reaches a maximum value and then it drops to zero for very thick aluminium layer. The maximum amplitude depends very strongly on the thickness of the base silicon layer as its value increases with decreasing of the silicon layer thickness. This thickness cannot be infinitesimal and its minimum value depends on the used technology. The influence of the ratio between the layers width over the deflection efficient is presented as well in

Figure 6.9b. It can be seen that the response has a maximum value for the layers with an equal width. When the aluminium layer is deposited on the top of the cantilever, it is necessary to have an electrical and thermal isolation between the aluminium and the silicon layer. This means that we have to use an additional dielectric layer, which is usually a silicon dioxide. As it is shown in *Figure 6.9c* this layer need to be very thin. *Figure 6.9d* presents the case, when the aluminium layer is on the backside of the cantilever and the silicon dioxide layer is on the top of the cantilever. However, the introduction of the silicon dioxide layer negatively affects the bimorph actuation efficiency.

As it was shown, under the thermal load the cantilever will stretch and bend. In addition, it has to be noted that the expressions (6-49) and (6-50) give two different detection possibilities. The first one is related to the stationary bending and the second one is related to the axial force, which according to section 6.2 indicates the changing in the resonance frequency. As the strain component is induced by the temperature change, the bimorph actuation always has an influence on the cantilever eigen frequencies. The dependence of the thermally induced stress on the thickness of the actuating aluminium layer is demonstrated in *Figure 6.10*.

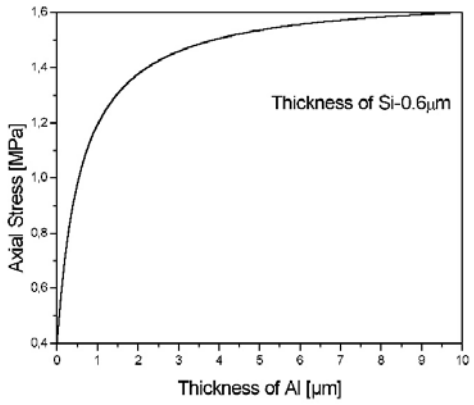

Figure 6.10 The thermally induced stress vs. Al layer thickness.

6.5 Analysis of the thermal actuators

The optimum deflection values of the bimorph cantilever were obtained from the previous section in case of uniform temperature distribution. In this section we will present a complete thermo-mechanical FEM analysis in order to predict the behaviour of real thermally driven cantilever device. A novel approach of the excitation of the mechanical vibration of micromechanical cantilever called "thermal drive" will be presented. Usually thermal actuation in MEMS is a direct result of incorporating tiny resistive heaters. These heaters can be controlled to heat locally specific areas or layers as in the case of a bi-layer actuator. The cantilevers developed in frames of this thesis were designed to accept a thermal input by passing a current through the aluminium (metal) layer or embedding resistor into the silicon layer. Resistive heating in the resistive element will raise the temperature of the beam. However the mismatch of the thermal expansion coefficients would cause the beam to bend. Two parameters are addressed to the actuator: i) consumed power needed to achieve a specified maximum bending deflection and ii) the actuating time.

The mechanical deflection is caused by the electrically induced thermal energy. Thus, the bending theory presented in the previous section has to be applied with the heat flow equation, which its solution will give the profile of the temperature distribution through the cantilever. From the heat transfer theory it is known that in most cases the heat conduction process conforms the Fourier law, which considers that the heat flux is proportional to the temperature's gradient. When the thermal conductivity, k_{th}, is constant, the energy balance for an arbitrary volume leads to the following three-dimensional heat equation.

$$\rho C \frac{\partial T}{\partial t} - k_{th} \nabla^2 T = \dot{q}\,, \tag{6-51}$$

where: C is the specific heat and $\dot{q}$ is the generated heat density per unit time.

In order to solve the heat equation, the thermal diffusivity as well as the initial and boundary conditions must be satisfied. Generally there are three basic kinds of

boundary conditions [74]: Dirichlet, Neumann and mixed conditions. Criteria, which are used in order to apply the proper boundary conditions, are described below:

i) If the walls have a prescribed temperature, they are called isothermal. The case of isothermal wall belongs to the *Dirichlet* type of boundary conditions (i.e. $T\big|_{wall} = T_0 = const.$). When the product of the specific heat per unit volume and the thermal conductivity of the wall material substantially exceeds the corresponding value for the surrounding gas, the assumption of isothermal walls is usually applicable [75].

ii) If the temperature derivative normal to the boundary, i.e. the heat flux, q, over the boundary, is defined, the *Neumann* boundary conditions are achieved (i.e. $\partial T/\partial \mathbf{n}\big|_{wall} = const.$). A particularly important special case is when there is no heat flux crossing the boundary i.e. the heat flux is zero, such boundary is called an adiabatic boundary. This case occurs on a boundary that is perfectly insulated.

iii) Dirichlet and Neumann boundary conditions may also be combined to form a third type of boundary condition, called a *mixed condition*. This boundary condition can be applied to all interface boundaries when the convective heat transfer is approximated according to the Newton's law of cooling (i.e. $q = h(T_{amb.} - T_{body})$) and the case of radiative heat transfer (i.e. $q = \varepsilon\sigma_{SB}T^4$) is valid. In the literature sometimes the convective boundary condition is called Robin's boundary condition [74].

The boundary conditions needed for the cantilever modelling will be assumed in the following way: Since the bulk of the cantilever is a large heat sink, the cantilever to bulk interface will be kept at room temperature. All other walls of the cantilever will be considered as adiabatic (in the case of vacuum). In the case of air some of the walls (which have a relatively large area) will be considered as convective. As we will work with relatively low temperatures, the thermal radiation will be totally ignored.

The methods for solving the heat equation can be divided into two general groups: analytical and numerical ones. Here we are focused on the numerical method by employing FEM. Generally, analytical methods allow solutions in the form of a single

formula of the whole structure. However, in most cases it is difficult to find such a solution due to the fact, that real structures have very complex shapes or boundary conditions.

Figure 6.11 presents the temperature distribution and the corresponding bimorph bending for three positions of the heating resistor. The cantilever has the following geometrical dimensions: length $562\mu m$, width $220\mu m$, thickness of the silicon layer $0.8\mu m$ and the thickness of the aluminium layer $0.8\mu m$. The heating element was simulated as an embedded resistor (with dimensions $170\mu m, 10\mu m, 0.4\mu m$). The applied electrical power in all cases was $272\mu W$.

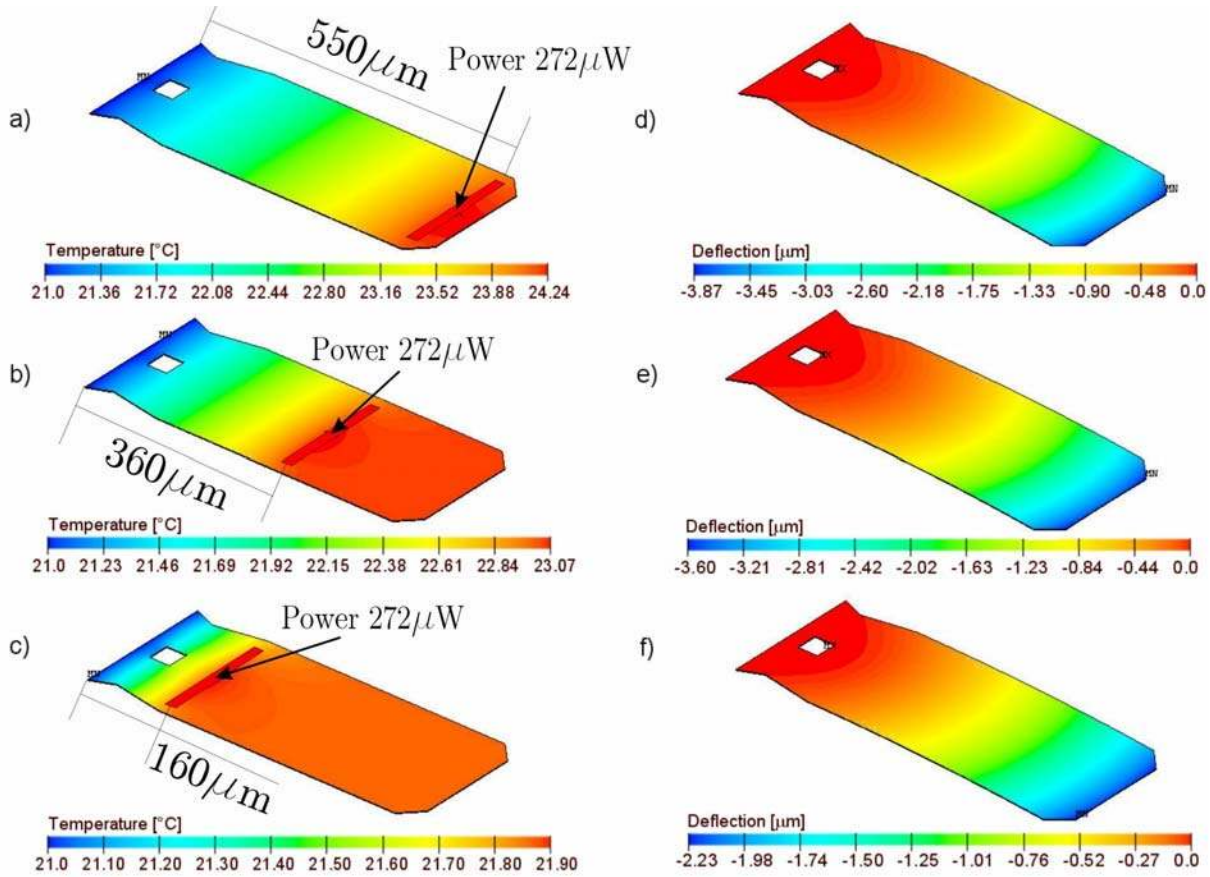

Figure 6.11 The bimorph effectivety vs. the heating element position.

The resistor was placed near the cantilever end, on the middle and near to the cantilever base respectively. As can be seen from the figure the temperature increasing and the corresponding bending efficiently with respect to the consuming power decrease

when the resistor is placed near the cantilever base. This means, that for the maximal temperature increase at fixed power, the resistor has to be as far as possible from the base of the cantilever. The temperature increase for the last case is about 1K and the distribution is nearly uniform. The corresponding bending deflection is $2.23\mu m$. This value is in an agreement with the obtained analytical results - *Figure 6.9*a.

In order to verify the FEM simulations, the calculations were done for cantilevers with the aluminium layer as resistive heater, which are currently available in our lab; *Figure 6.12*.

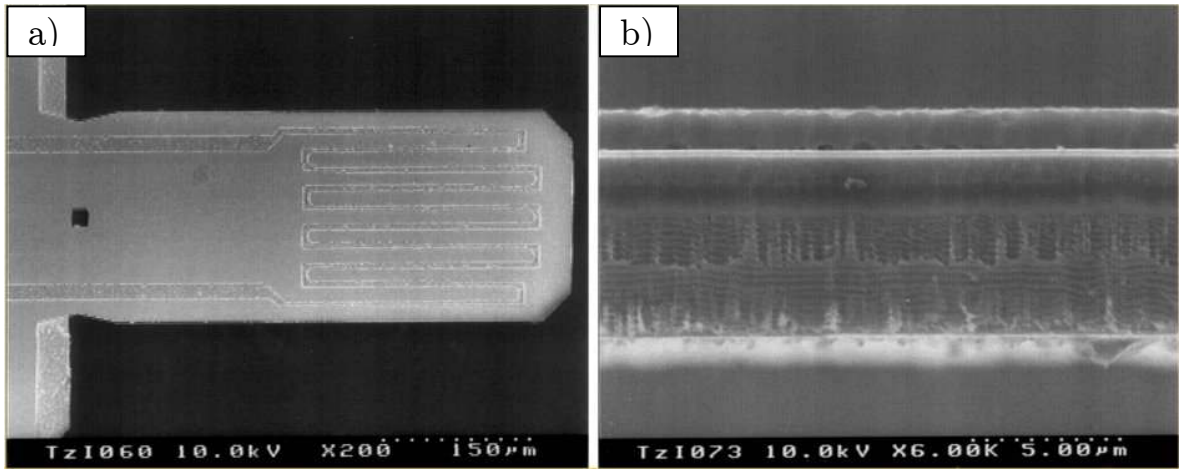

Figure 6.12 a) Scanning electron microscopy micrograph of the cantilever device; b) cross-section of the cantilever, where the thickness of Si=5µm, SiO_2=1.3µm and Al=1.3µm are visible.

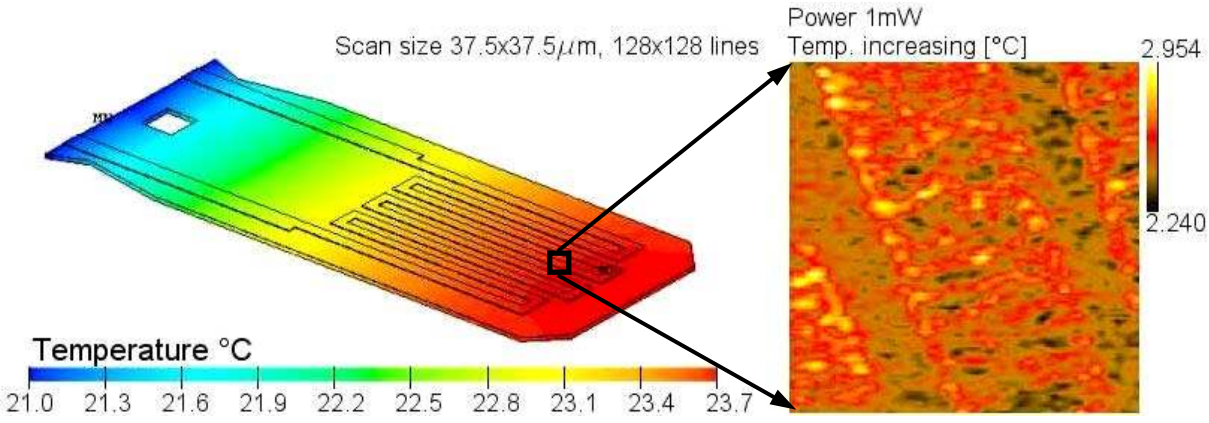

Figure 6.13 FEM calculation of the temperature distribution in comparison with the result obtained from the STM measurement.

Figure 6.13 illustrates a comparison between the experimental measurements of the increasing temperature due to the applied electrical power $1mW$ and a FEM simulation. It can be noticed that a good agreement between the simulations and experimental results has been achieved.

When the applied electrical power is $15mW$, the estimated cantilever bending of the cantilever end was $1.67\mu m$ *(Figure 6.14)*. This result was compared with the interferometer measurements (New View 3D Surface Profilers from Zygo) presented in *Figure 6.15*. Unfortunately the size of the interferometer camera was not big enough to investigate the entire cantilever. Thus the bending distribution measurement has been taken in the range of $0\mu m$ to $360\mu m$ along the cantilever length. As it can be seen *(Figure 6.15)*, if there is no applied power, the cantilever is already bended due to the compressive stress in the SiO_2 layer. When the electrical power of $15mW$ is applied to the aluminium heater the bending at the position $360\mu m$ increase with $412nm$. This experimentally obtained result was predicted from the FEM simulation presented in *Figure 6.14*.

The above considerations provided static cantilever actuation as a response to the DC voltage (V_{dc}) applied to the heather. In order to realise a high speed TM-AFM we use the above presented bimorph actuator to both: drive the cantilever at its resonance frequency, and to provide z-actuation (needed for the feedback loop, which controls the distance between the tip and the sample). For this reason, cantilever excitation is done by periodic heating, which is realised by applying an AC voltage (V_{ac}). The heating power is a square of the electrical voltage sum:

$$P = \frac{1}{R_{Heater}}\left(V_{dc} + V_{ac}\sin\omega t\right)^2 = \frac{1}{R_{Heater}}\left(V_{dc}^2 + 2V_{dc}V_{ac}\sin\omega t + V_{ac}^2\sin^2\omega t\right) . \quad (6\text{-}52)$$

It can be seen that the input signal power has three components: steady component, component with frequency ω and component with frequency 2ω. Moreover the detected signal on the piezoresistive read-out will contain also three components. Since the 2ω component depends only on the amplitude of the AC signal, it was taken for the imaging purpose. In such way, the cantilever has to be excited to oscillate at the

resonance frequency $f_r = \omega_r/2\pi$ by driving signal with radial frequency ω equal to $\omega_r/2$.

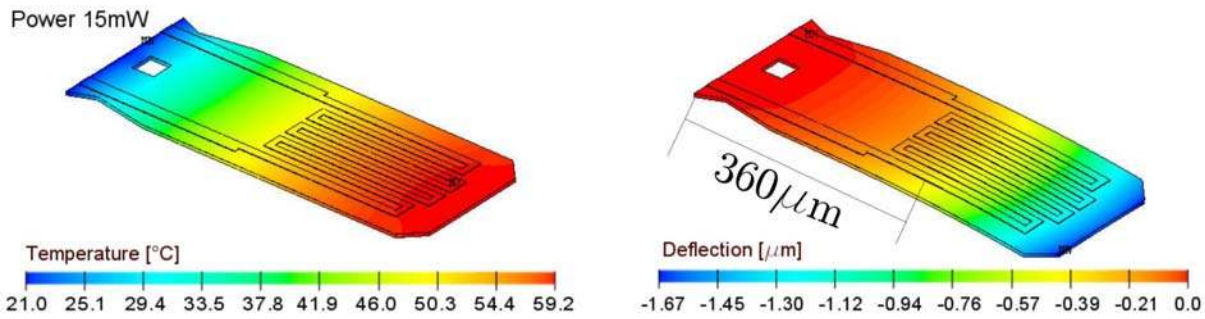

Figure 6.14 FEM calculations of the temperature distribution along the cantilever length and following deflection distribution.

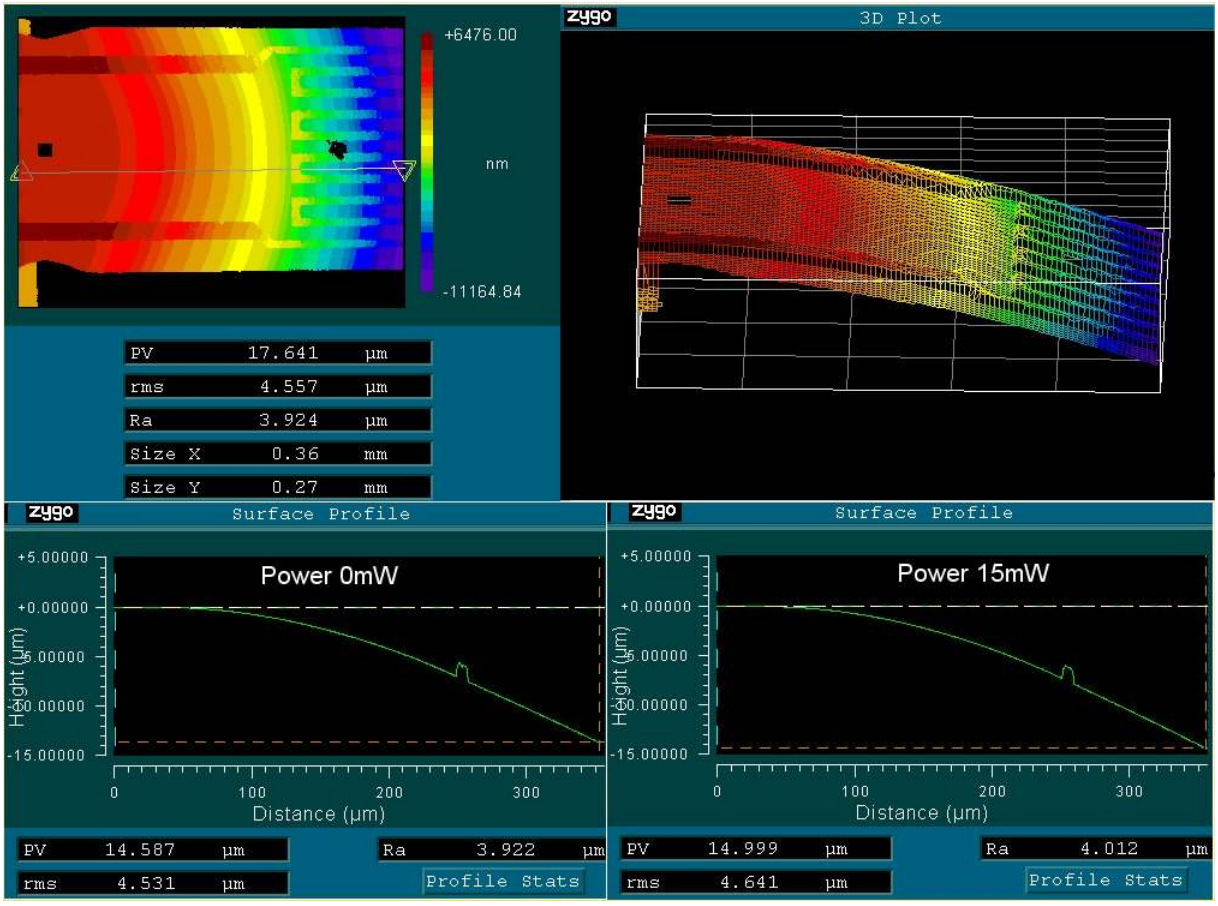

Figure 6.15 White light interferometer measurement of the deflection distribution along the cantilever length.

Integration of the thermal actuator with the cantilever results in a compactness of the scanning head. This is essentially true for an array of cantilevers where it is necessary to control the distance between the sample and the tip of each cantilever.

Figure 6.16 shows the temperature evaluation of the cantilever when the square-wave heat impulse is applied. As it can be seen, the integrated thermal bimorph z-actuation has a relatively slow response. This behaviour is due to the time needed for reaching stable temperature distribution and extending the temperature wave along the whole cantilever. The time needed for this process is always limited by the thermal diffusivity $D \equiv k_{th}/C\rho$. At a given cantilever length l the maximum frequency is $D/\pi l^2$, e.g. in the $500\mu m$ silicon cantilever the maximal frequency is less than $100Hz$.

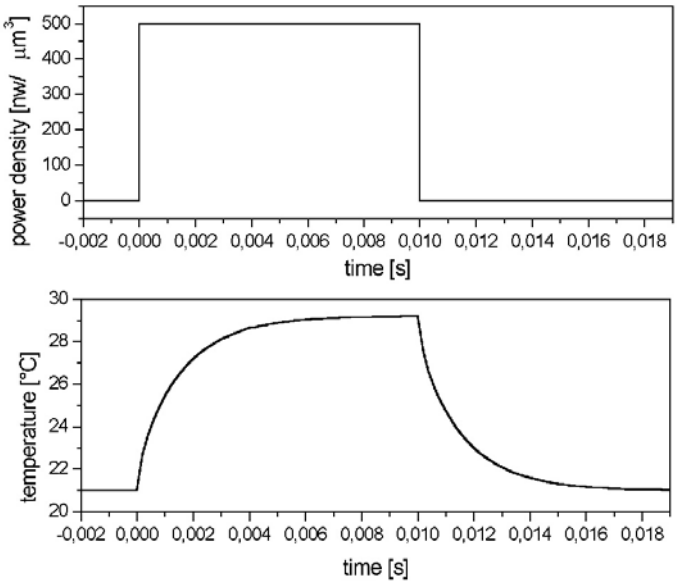

Figure 6.16 Evaluation of the max. temperature with respect to the input impulse.

The slowness of the cantilever response with respect to the heating pulse can be avoided if we design the heating element uniform to the cantilever length. Such geometry of the heater allows an actuation response frequency even up to megahertz. This mechanism is connected with the fact that at the beginning the temperature increases as a result of the stored thermal energy in the heating element. As the stored thermal energy by the fixed power density is proportional to the time, the temperature will also rise. In the aluminium the power density of $2.43\,nW/\mu m^3$ will give a

temperature increment about $1mK$ for time of $1\mu s$, such temperature increase is enough to actuate the optimised bimorph cantilever with amplitude of few nanometers needed for the TM-AFM. This also will be proved experimentally in chapter 8.3. It has to be noted that this design allows driving the cantilever at its resonance frequency, however the stable oscillations are reached after $10ms$.

Finally, we can conclude that we can also benefit from the integrated thermal bimorph actuator in case of array of cantilevers scanning in parallel. Then each cantilever can be driven in resonance modes with few hundred kilohertz. Simultaneously the z control distance, which insure following of the topology, will be with frequency of few hundred Hertz.

6.6 Analysis of the piezoresistive sensor

To realise a fast TM-AFM system it is necessary to have a thermally actuating cantilever, which has to be able to detect the oscillation amplitude and its changes when the cantilever tip approaches the sample surface. There are many sensing methods that may be employed - interferometric, optical and capacitance. The disadvantage of these methods is the requirement of external sensing element. Following the aim of this work, an integrated piezoresistive sensor, the theory of which was already discussed, is chosen.

As mentioned previously, the change in resistance of a piezoresistive transducer can be sensed with relatively simple interface circuits. One of these circuits is a Wheatstone bridge, which is shown in *Figure 6.17*.

In our design we use a full Wheatstone bridge configuration, where all four resistors are placed on the cantilever beam and act as a piezoresistive transducers. The output voltage, U_{out}, is depended on the changing of the piezoresistor values ΔR_i, which are directly proportional to the strain on the cantilevered beam:

$$U_{out} = U_{in} \frac{\Delta R_1 + \Delta R_3 - \Delta R_2 - \Delta R_4}{4R}. \qquad (6\text{-}53)$$

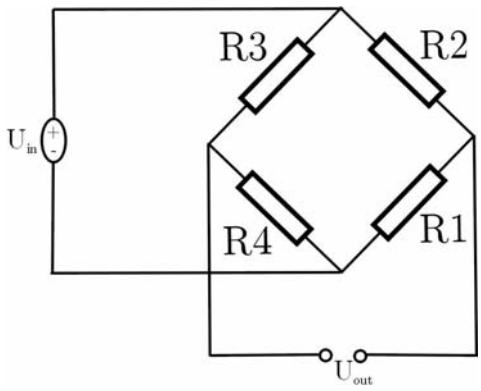

Figure 6.17 Wheatstone Bridge configuration.

For a balanced bridge circuit, we have that $\Delta R_i = 0$. When the cantilever is bended a changing in the resistance $\Delta R_1 = \Delta R_3 = \pi_t T_{xx} R$ and $\Delta R_2 = \Delta R_4 = \pi_l T_{xx} R$ occurs. This leads to the following expressions for U_{out}:

$$U_{out} = -U_{in} \frac{(\pi_l - \pi_t)}{2} T_{xx}. \tag{6-54}$$

As can be seen from the analysis, if the piezoresistive coefficients and input voltage are known, the stress (strain) and therefore the bending of the beam can be directly related to the output voltage of the Wheatstone bridge.

The values of the piezoresistors, incorporated in the device, in the Wheatstone bridge, are governed by the following relationship:

$$R = \frac{\rho_r L_r}{A_r}, \tag{6-55}$$

where: R is the resistance value of each resistor in the bridge, ρ_r is the resistivity of the doped silicon, L_r is the length of the resistor and A_r is the cross-sectional area of the resistor. The resistance has to be chosen in such a way that it will give minimum noise contribution (see section 7.4).

It must be pointed out that all bridge resistors are located on the beam and need to be adjusted for two aspects. First, there will be an offset in the designed nominal resistor value due to the induced residual stress from fabrication process. The curvature of the cantilever presented in *Figure 6.15* is evidence for this. According to equation (6-54), this will lead to an initial offset of the Wheatstone bridge. The second adjustment must be applied in order to compensate the resistivity variation due to the temperature change in the piezoresistive layer. This temperature changing is due to the heating of the bridge (*Figure 6.18)* and the heating from the aluminium layer (*Figure 6.13)*.

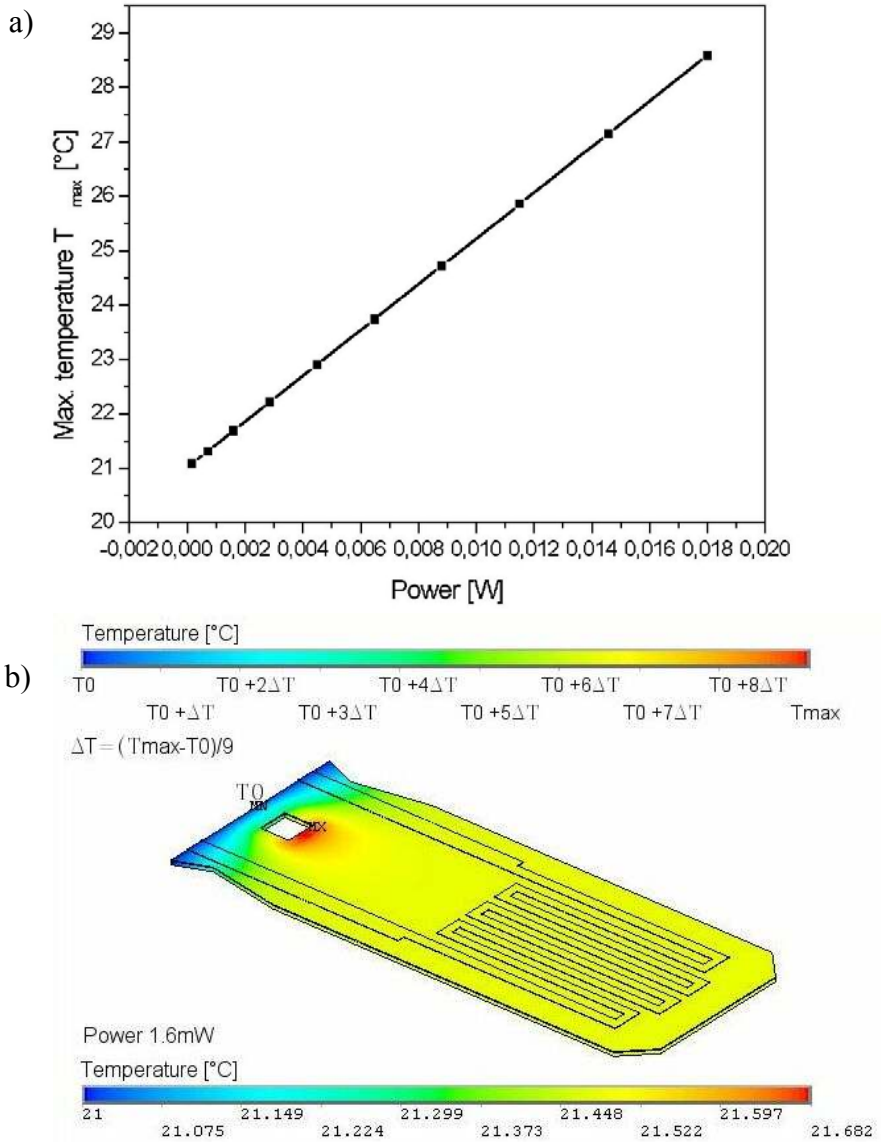

Figure 6.18 a) Maximal temperature as a function on the power dissipating in the Wheatstone bridge b) The temperature distribution of the cantilever -T_{max} has to be taken from a).

The resistance shift can be calculated from the following relation:

$$\Delta R = \Delta T \times R \times TCR_{Si}\,, \tag{6-56}$$

where, TCR is a temperature coefficient of resistance.

The piezoresistors were placed in Wheatstone bridge configurations to provide simple signal amplification and first order temperature compensation as it can be seen from the following analysis:

$$\begin{aligned}\Delta R_2 = \Delta R_4 &= \int_0^{L_r} TCR_{Si}\left[\frac{x\left(T_{R3}-T_{R1}\right)}{L_r}+T_{R1}\right]\frac{\rho_r}{A_r}dx = \\ &= TCR_{Si}T_{R3}\frac{\rho_r}{A_r}\frac{L_r}{2}+TCR_{Si}T_{R1}\frac{\rho_r}{A_r}\left(L_r-\frac{L_r}{2}\right)=\frac{\Delta R_3}{2}+\frac{\Delta R_1}{2},\end{aligned} \tag{6-57}$$

where, T_{R1} and T_{R3} are the temperature of the transversal piezoresistors. However, we have assumed that the temperature is linearly distributed along the longitudinal piezoresistors and it's value increases from T_{R1} to T_{R3}.

Using equation (6-53) we can see that the above configuration of the Wheatstone bridge really enables a first order temperature compensation. In reality the piezoresitors have different TCRs [76], which of course lead to additional fluctuations in the output voltages. As it can be seen from the FEM calculations presented in *Figure 6.18*, for piezoresistors with nominal $2K\Omega$ and typically used input voltage $0.7V$ (dissipating power is $250\mu W$), the maximal temperature increase is less than one Kelvin.

Chapter 7
Fundamental limitation of sensitivity by Noise

During the weak signal measurement experiments, the measured signal is always limited by the spontaneous fluctuation in the physical variables of the system called noise. The presence of the noise is a significant problem in every precise weak signal measurement, therefore the study of its phenomenological behaviour is very important. For that reason, the estimation and reduction of the noise is one of the most important issues for determination and improvement of the piezoresistive AFM sensors ultimate sensitivity. Since the piezoresistors are the crucial component of the sensors, they also will be examined for their noise characteristics.
In this chapter we will study the noise in cantilever-based sensors.

7.1 Introduction and basic mathematical methods

Noise is a stochastic process consisting of a randomly time varying function. In such way the single system need to be discussed statistically. One can define different quantities for time and ensemble average. In noise time averages theory the exploitation quantities are: mean (first order average), mean square (second order average), and autocorrelation function, which are defined as:

$$\langle x(t) \rangle = \lim_{T \to \infty} \frac{1}{T} \int_{-T/2}^{T/2} x(t)\, dt \,, \tag{7-1}$$

$$\left\langle x(t)^2 \right\rangle = \lim_{T \to \infty} \frac{1}{T} \int_{-T/2}^{T/2} x(t)^2\, dt \,, \tag{7-2}$$

$$S(t') \equiv \langle x(t)x(t+t') \rangle = \lim_{T\to\infty} \frac{1}{T} \int_{-T/2}^{T/2} x(t)x(t+t')dt \,. \tag{7-3}$$

When $t'=0$ the autocorrelation function becomes equal to the mean square value. The power spectrum density (noise spectrum) is defined as:

$$S(\omega) = \lim_{T\to\infty} \frac{|X(i\omega)|^2}{T}, \tag{7-4}$$

where $X(i\omega)$ is the Fourier transform of the function $x(t)$:

$$X(i\omega) = \int_{-\infty}^{\infty} x(t)e^{-i\omega t} \,. \tag{7-5}$$

The Parseval theorem [77] is given by following expression:

$$\int_{-\infty}^{\infty} x_1(t)x_2^*(t)dt = \frac{1}{2\pi} \int_{-\infty}^{\infty} X_1(i\omega)X_2^*(i\omega)d\omega \,. \tag{7-6}$$

Applying the Parseval theorem to the functions $x_1(t) = x(t)$ and $x_2(t) = x(t+\tau)$, dividing both sides of the resulting expression by T and taking a limit as $T \to \infty$, we obtain:

$$S(t') = \frac{1}{2\pi} \int_{-\infty}^{\infty} S(\omega)e^{\omega t'}d\omega \,. \tag{7-7}$$

The given relation between the autocorrelation function and the noise spectrum is known as Wiener-Khintchine theorem [78] and it is widely used in the noise theory. The importance of this theorem is, that the autocorrelation function can be expressed as an inverse Fourier transform of the power spectral density:

7.2 Thermal Noise

There are two types of intrinsic noise in every physical system: thermal noise and quantum noise. These two types of noise cannot be eliminated even when the system is perfectly constructed and operated. However we will not consider the quantum noise since for the cantilever modes the relation $\hbar\omega \ll k_B T$ is satisfied.

A conductor is the simplest physical system, which produces intrinsic noises. The physical origin of thermal noise in a macroscopic conductor is a "Random-walk" of thermally-fluctuated electrons. An electron undergoes a Brownian motion via collisions with the lattices in the conductor. A. Einstein first studied the statistical properties of such a Brownian particle. His explanation of the thermal noise in the conductors is based on a microscopic approach.

Nyquist employed a completely different approach to this problem [79]. He introduced the concept of a mode for the system by using a transmission line cavity terminated by two conductors, and then applied the equipartition theorem of thermodynamics to these transmission line modes. In this way he was able to explain the thermal noise without going into the details of a microscopic electron transport process. Nyquist's approach is very general and it can be easily extended to include quantum noise, which is important for high frequency and low temperature case.

Similarly to the electrons in the conductor, the micromechanical cantilevers are susceptible to thermo-mechanical noise resulting from molecular excitation. As the microcantilever sensors are designed for small signal measurements, the thermo-mechanical noise could set the limit on the lowest measurable displacement of the micro beam. The thermo-mechanical noise arises due to the Brownian motion of the particles in the surrounding medium, that is, agitation of the floating-element structure due to collisions from the particles in the surrounding gas. The collisions caused displacement, which sets the limit on the smallest detectable force induced displacement.

Based on equipartition theorem, in the same way like Nyquist, we will demonstrate the minimum detectible force by the cantilever-based sensors.

According to equation (6-29), the cantilever behaviour can be modelled as a simple harmonic oscillator of frequency $\omega_j = \sqrt{k/m}$. The expectation value for the total energy of the quantized harmonic oscillator of frequency ω is [80]:

$$\frac{\hbar\omega}{e^{\hbar\omega/k_BT}-1} \overset{\hbar\omega<<k_BT}{\approx} k_BT\,. \tag{7-8}$$

As the expected value of the potential energy is a half of the expected value of total energy, we have:

$$\frac{1}{2}k\left\langle \tau(t)^2 \right\rangle = \frac{1}{2}k_BT\,. \tag{7-9}$$

Taking into account, that the mean square is given by equation (7-7) for $t' = 0$, using the Parseval theorem, going from displacement noise spectrum $S_\tau(\omega)$ to the force noise spectrum $S_F(\omega)$ according to equations (7-4) and (6-40) and assuming that the force noise spectrum is white, finally we obtain:

$$S_F = \frac{2\pi k_BT}{\int_{-\infty}^{\infty} \left|H(\omega)\right|^2 d\omega}, \tag{7-10}$$

$$S_F = 2k_BT\gamma = 2k_BT\frac{k}{Q\omega_r}\,. \tag{7-11}$$

In many experiments our measurements have been taken over a limited frequency bandwidth $\Delta\omega$, however, for a small frequency interval $\Delta\omega$ around the resonance, we have for the force noise:

$$\left\langle F^2 \right\rangle = \int_{\omega_r-\Delta\omega}^{\omega_r+\Delta\omega} S_F\, d\omega = 2S_F\Delta\omega\,. \tag{7-12}$$

Thus the force noise spectrum results in a thermal force noise $\sqrt{2S_F\Delta\omega}$ and the minimum detectable force can be expressed as:

$$F_{\min} = \sqrt{4\frac{kk_B T\Delta\omega}{Q\omega}}\,. \tag{7-13}$$

The above presented theory is a particular case of most general fluctuation dissipation theorem (FDT), established by Callen [12]. FDT gives the relationship between the spectrum of the thermal noise and the dissipation of systems as $S(\omega) = 2k_B T\,\mathrm{Im}(H_\omega)/\omega$ [80]. In such manner, the thermal noise is related to the dissipation. The physical origin of the dissipation channels have to be studied in order to obtain an optimal cantilever beam geometry. Several kinds of the dissipation, which can limit the minimum detectable force, will be introduced in the following sections. Sources of the loss are classified into the two categories: in the first category, the sources of the loss are external and in the second category, the sources of the dissipation are inside in the cantilever itself (internal losses).

7.3 Energy dissipation

The energy dissipation can be parameterised by the quality factor-Q, which is defined as a ratio between the stored vibrational energy E_{stored} and the total energy loss per cycle ΔE_{diss}:

$$Q = \frac{1}{2\pi}\frac{\Delta E_{diss}}{E_{stored}}\,. \tag{7-14}$$

As can be seen from the previous section, the thermo-mechanical noise is related to the quality factor of the cantilever. Therefore a high quality factor is needed to reduce the noise level. For sensor applications resonance frequency shifting can be determined very precisely if the resonator has a higher quality factor, leading to greater sensitivity.
The energy dissipation represents the loss due to the various dissipation mechanisms. In such a way the Q factor is determined from the contribution of individual quality factors which characterize the different dissipations (energy losses), according to the following relation:

$$\frac{1}{Q} = \sum_i \frac{1}{Q_i} . \tag{7-15}$$

The loss mechanisms can be classified as extrinsic and intrinsic losses. The extrinsic losses are independent from the material itself, but they are influenced by the design of the structure. In a properly chosen environment conditions the extrinsic losses can be made a negligibly low. Thus the dissipation is dominated by the intrinsic losses in the material of the cantilever.

The extrinsic losses are expressed as viscous damping, which can be described by the forces proportional to the velocity. In order to describe the intrinsic losses, the complex spring constant model [81] is frequently used. This model is an extension to the Hooke's law. This extended Hooke's law expresses the fact, that the strain phase of the spring lags behind that of the restoring force. The material property causing the phase lag is called anelasticity.

7.3.1 Air damping

According to *Blom* [82], the air damping can be separated into an intrinsic, a molecular, and a viscous region. In the intrinsic region, the air friction is not a significant source of energy loss and the dominant dissipation mechanisms will be described in the next subsections.

Generally, the interaction of the surroundings with the beam can be summarized by a drag force F_{drag}, which is pressure depending. At low pressure, the collisions of the air molecules with the cantilever surface can be considered independent of each other. This region is also known as a Knudsen region. The energy losses due to the drag force depend on the cantilever geometry, operation eigenmode and pressure. The quality factor increase linear by a pressure decrease. However, it also depends on cantilever width, reciprocal cantilever length and wave number like a squared power law. The

experimental study of the Knudsen effect and its influence on micro-cantilever operation can be found in reference [83].

For higher pressure, in the viscous region, the gas acts as a viscous fluid. Assuming that the air is incompressible and that the Reynolds number is small (no turbulences) the force on the surface can be calculated using the Navier-Stokes and the continuity equations [84]. The beam will be approximated with a row of spheres vibrating independently of each other [85], because it is difficult to determine the velocity field of the air around the vibrating beam. The results of this theory are that the quality factor increases with reducing the cantilever length. Therefore, shorter cantilevers are preferable to be used for AFM in air and liquid environments [86].

According to Hoummady, [87], an additional improving of the sensitivity to the force gradient is possible when the cantilever operates at a higher resonant mode. Completely theoretical and experimental researches also confirm the enhancement of the quality factor for higher order vibration modes [88].

For the cantilevers operating in vacuum, the experiment shows a reduction of the quality factor at higher resonance modes [89]. The most important dissipation mechanisms in intrinsic region (pressure less than 1mTorr) are: clamping losses, thermoelastic losses and losses connected with cantilever surface.

7.3.2 Clamping losses

Since the real elements are never been perfectly rigid, the energy can be dissipated from the vibrating cantilever to the supporting structure, where local deformations can occur. At the contact area between the beam and the clamp, a slide occurs when the beam bends [90]. Using the result from Hosaka [91], the quality factor for clamping losses can be expressed as $2.17 l^3/t^3$. When the ratio between the length and thickness of the cantilevers is about 50, the quality factor due to the clamping losses will be more than 2.5×10^5. This value is two orders of magnitude greater than the

experimentally measurement values. Thus we can conclude that, the clamping losses do not limit Q of the cantilevers.

7.3.3 Thermoelastic losses

Similarly like the interaction of the cantilever with the thermal bath of the environment, the interacting of the cantilever vibration with the bath of the thermally exited elastic modes will produce energy dissipation and therefore noise. Thus such energy dissipation is called thermoelastic damping (TED). The thermally exited elastic modes are caused by an inhomogeneous strain of an elastic body. Since the thermal expansion coefficient is not equal to zero, the strain changes the temperature in the elastic body. If the strain is inhomogeneous, a gradient of temperature occurs, however, heat flows to compensate this gradient of temperature. The elastic energy is dissipated due to this heat flow. The details of the process of the thermoelastic damping for anelastic solids are described in the original work of Zener [92 , 93]. Further research is given in [94]. Roszhart [95] observed experimentally the thermoelastic damping in single-crystal silicon microresonators at room temperature

The physical model for the thermoelastic coupling in case of cantilever beam is based on the following equations:

$$\rho A \frac{\partial^2}{\partial t^2}\xi(x,t) + \frac{\partial^2}{\partial x^2}\left(YI \frac{\partial^2}{\partial x^2}\xi(x,t) + Y\alpha I_T \right) = 0 , \tag{7-16}$$

$$\frac{\partial \theta}{\partial t} = D\nabla^2\theta - \frac{Y\alpha T}{(1-2\nu)C\rho}\frac{\partial}{\partial t}\sum_j S_{jj} . \tag{7-17}$$

where $I_T \equiv \int_A zTdA$.

The first equation follows from the equation of the cantilever motion (6-19). The axial force is due to the temperature fluctuations. The second equation is the rewritten heat equation (6-51) in presence of thermoelastic coupling. The power of the thermal source is equal to the change of the inside energy of the medium $T_{ij}dS_{ij}$ for time dt.

The solutions of the beam motion equation coupled with the thermoelastic equation are given in [96]. As a result the losses due to the thermoelastic dumping can be described with the following quality factor:

$$Q_{TED} = \left[\frac{YT\alpha^2}{C\rho} \left(\frac{6}{\zeta^2} - \frac{6}{\zeta^3} \frac{\sinh\zeta + \sin\zeta}{\cosh\zeta + \cos\zeta} \right) \right]^{-1}, \tag{7-18}$$

where the dimensionless variable depends on thermal diffusivity, cantilever thickness and cantilever resonance frequency and is expressed as: $\zeta \equiv t\sqrt{\omega_n / 2D}$.

According to equation (7-18), *Figure 7.1* shows the quality factor due to the thermoelastic losses as a function of the cantilever thickness. The cantilever length was $562\mu m$. The Q factor of the very thin cantilevers (under $5\mu m$), which are operating at one of the first three eigenmodes is not limited by TED. For shorter cantilevers, the increase of the resonance frequency leads to shift of the curves to wards the down left corner. Therefore for shorter and relatively thick cantilevers we can expect than the TED will limit the Q factor under 10^4.

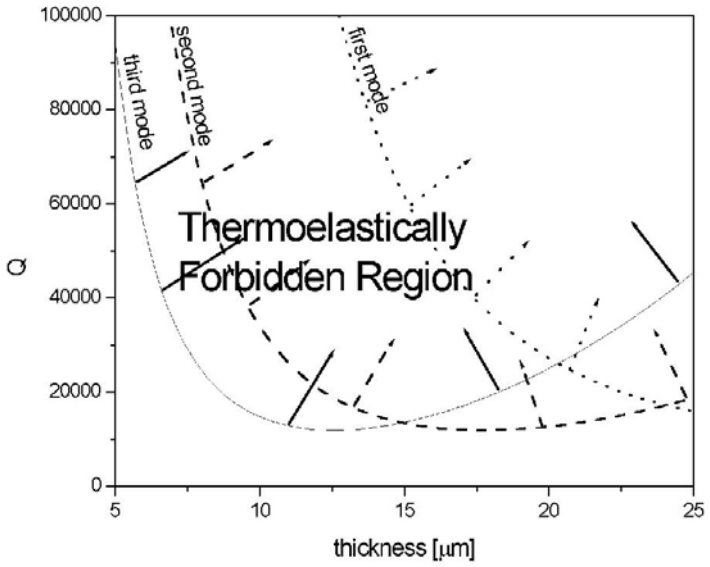

Figure 7.1 The thermoelastically limed quality factor for the first three modes as a function of the cantilever thickness

As a consequence of the above analysis we can conclude, that for thinner cantilevers there is another loss mechanism, which limits the quality factor below 10^4.

7.3.4 Losses connected with the surface

Changes between the properties of the bulk material and the environment are occurred in interface regions. It can be expected that for micro-cantilevers, where the volume of the interface region and the volume of the bulk are of the same order, the influence of the surface properties will take also an important place. Yasumura *et al.* stated in a literature review that the Q-factor decreases with decreasing oscillator dimensions [16]. This suggests that the dominant loss mechanisms in thin cantilevers are surface related. Unfortunately, loss mechanisms at the surface are still not well understood, but the experimental trend is that the Q-factor decreases with the scaling of the cantilever dimensions.
The surface imperfections such as: oxide layer [97], nature water layer [98] and metal coating [99] can be significant loss channels in the ultra-thin cantilevers. An additional treatment of the cantilever surface can reduce surface losses [100].

7.4 Piezoresistor detection noise

The noise sources, which were studied in the previous section, are connected to the mechanical cantilever response. In order to detect this response we have to transform the mechanical signal to an electrical one. As was discussed before, this transducers are piezoresistors configured in an Wheatstone bridge. The electrical noise due to the piezoresistive detection method contributes to the noise following from the detecting mechanical noise. Hence the electrical noise can reduce additionally cantilever's sensitivity and it is important to study the possible noise sources in piezoresistors.

The observed voltage and applied force are connected through equations (6-5), (6-9) and (6-54). In the frequency domain the connection between the output voltage and the applied force is:

$$\tilde{U}_{out}(\omega) = 3U_{in}\frac{(\pi_l - \pi_t)}{R}\frac{k_n H_n(\omega)\tilde{F}(\omega)l}{wt^2}. \tag{7-19}$$

This equation is valid for the case of thin surface piezoresistors, placed at the cantilever base and the force applied at the cantilever end.

7.4.1 Johnson noise

In 1927, Johnson [101] discovered that the noise power spectrum of a conductor is independent of its material and the measurement frequency. Under thermal equilibrium the noise properties are determined only by the temperature T and the electrical resistance R:

$$S_{U-JN}(\omega) = \left\langle \tilde{U}_{out}(\omega)^2 \right\rangle = 4k_B TR. \tag{7-20}$$

For measurements on the resonance this noise limits the minimum detecting force, in the frequency interval $\Delta\omega$, to the following value:

$$F_{\min-Jh} = \frac{2wt^2}{3(\pi_l - \pi_t)lQ}\sqrt{\frac{k_B T\Delta\omega}{P}}. \tag{7-21}$$

According to equation (7-19) if we increase the bridge supply voltage U_{in}, the voltage output will increase linearly. However, it has to be noted that the increasing power dissipation $P = {U_{in}}^2/R$ will increase linearly the resistors' temperature $T = T_0 + aP$, (*Figure 6.18*). Thus the Johnson noise level will be independent on the power for the low temperature operation $T_0 \to 0$ and will be reduced for room temperature operation

of the cantilever. On the other hand the temperature of the cantilever will also rise and the force resolution will be decreased. As a result the TED will increase and the noise level will rise linearly with the temperature. But if the TED is not the dominant dissipation mechanism (for example cantilever operating in air) the increase of the bridge voltage will also increase the noise level (due to the increasing temperature of the surrounding gas) as a square root of the temperature and thus we can expect better signal to noise ratio.

7.4.2 1/f noise

Practically in all electronic and optical devices, in addition to the Johnson noise, there exist noise, which obeys the inverse frequency power law. Since its spectral density is inversely proportional to the frequency the noise is known as 1/f noise. After the first observation of this noise in an electronic system, made by Johnson [102], an enormous amount of experimental data has been accumulated on 1/f noise in various materials and systems. The 1/f noise is ubiquitous but no universal physical mechanism has been proved definitively as the cause for it.

In 1969 Hooge [103] has proposed an empirical relation for the 1/f noise in homogeneous samples:

$$S_{U-1/f}(\omega) = \frac{\alpha_H}{N_e}\frac{1}{f}U^2, \qquad (7\text{-}22)$$

where U is the bias voltage across a resistor with a total number of carriers N_e and α_H is a dimensionless parameter. Thus the model contains empirical parameter unlike thermal noise. In other words, 1/f noise can be modelled empirically but cannot be predicted *a priori*.

If the 1/f noise is the dominant noise source for measurements on the resonance, the minimum detecting force in the frequency interval $\Delta\omega$, has the following value:

$$F_{\min -1/f} = \frac{wt^2}{3(\pi_l - \pi_t) lQ} \sqrt{\frac{2\pi\alpha_H \Delta\omega}{N_e \omega}} . \qquad (7\text{-}23)$$

Thus the 1/f spectrum makes measurements at low frequencies more difficult. It can also be seen that the increase of doping concentration can improve the force resolution. Usually, the physical explanation of the 1/f noise is based on charge trapping behaviour of defects and impurities at the Si/SiO_2 interface. An other mechanism proposed includes a temperature fluctuation model [104] and a quantum mechanical model [105]. A new physical model was developed by Aldert van der Ziel [106] for explaining the dependence of the Hooge noise in a MOSFET. Long channel MOSFETs exhibit less 1/f noise since larger gate oxide capacitances smooth the fluctuations in the channel charge [107].
The dimensionless parameter α_H is process dependent and therefore surface treatments and an appropriate anneal must be chosen to minimize the noise [108].

7.5 Force resolution optimisation

All the noise sources mentioned above are incoherent. Therefore the total random noise is calculated by taking the square root of the sum of the squares of all the incoherent noise sources. From this viewpoint, the cantilever resolution can be improved by the optimisation of the following parameters: cantilever geometry, properties and operation conditions of the piezoresistors, as well as the choice at which eigen frequency mode the cantilever should operate.

Geometry: Cantilevers for high force resolution should be as narrow as the technology limitations allow. The cantilever thickness has to be reduced. For cantilever operated under air conditions, the length should be minimal. Cantilevers, operating in vacuum, have to be extended to the length at which the cantilever resonance frequency will be equal to the minimum possible operation frequency with respect to noise.
Piezoresistors: At high dopant concentrations there are many carriers, and therefore the Hooge noise is reduced. At low concentrations the sensitivity is highest, which gives the

best resolution for cantilevers limited by Johnson noise. Hence, we prefer low doped piezoresistors, which are high voltage biased in order to improve the signal to noise ratio.

Operation frequency: A cantilever optimised in such a way has a low fundamental eigen frequency, which limits the measurement speed (see Chapter 6.3). Thus we prefer the measurements in higher eigenfrequency modes. Another benefit is the improved coupling between the mechanical system and the piezoresistors following from the fact that the slope of the cantilever near the base is higher. This can give a higher stress and improves the signal from the Wheatstone bridge.

Table 7 gives examples of the minimum detectable force by cantilevers with different geometry. All calculations were done for the mode independent quality factor $Q = 420$, Hooge parameter $\alpha_H = 10^{-9}$ and doping concentration for the piezoresistors was $n_e = 10^{22} m^{-3}$. The oscillation amplitude was $10nm$.

It can be seen that the 1/f and Johnson noise contributions are negligible compared with the thermo-mechanical noise. For all type of cantilevers the thermo-mechanical noise increase for higher modes, and this is due to the fact that the possibility of the increasing of the quality factor for the higher modes was not taken into account.

In this work cantilevers with geometry corresponding to the type 1 were fabricated. The typical measured noise spectrum of a cantilever is shown in *Figure 7.2* (the measurements were performed with SPM-1000 control system manufactured by RHK). The experiment was done for two cases: i) the supply voltage U_{in}=0V and ii) the supply voltage U_{in}=1V. In such way it was easy to distinguish the contribution of every noise source. The experimentally estimated level of the Johnson noise was $1.5 \times 10^{-8} V/\sqrt{Hz}$. This value is in good agreement with the theoretical value for the Wheatstone bridge with four equivalent resistors - $\sqrt{4 \times 4 k_B T R} \approx 1.29 \times 10^{-8} V/\sqrt{Hz}$ (T=300K, R=2.5KΩ). The $1/f$ noise is significant up to a few hundred Hertz. For higher frequencies the dominant noise source for measurements in air is the thermo-mechanical cantilever noise, which can limit the minimum detectible force (for theoretically estimated value see *Table 7*).

The cantilevers of type 2,3 and 4, which are with improved geometry, have to be done in future work.

№	Geometry l	w	t	eigen mode	f_{res}	k	Temp. T_0	T_{pr}	F_{min} th.	Jh.	1/f	sum	$(dF/dz)_{min}$ sum
	$[\mu m]$				$[KHz]$	$[N/m]$	$[K]$		$\left[fN/\sqrt{Hz}\right]$				$\left[\mu N/m\sqrt{Hz}\right]$
1	562	220	5	1	22.378	6.58	293	303	43	5.4	3.5	43.5	4.35
				2	140.23	258	293	303	107	5.4	1.4	107	10.7
				3	392.70	2026	293	303	180	5.4	0.8	180	18.0
2	562	60	5	1	22.378	1.79	293	303	22	1.5	0.9	22	2.2
				2	140.23	70.3	293	303	55	1.5	0.4	55	5.5
				3	392.70	551	293	303	92	1.5	0.2	92	9.2
3	562	60	0.5	1	2.237	0.002	293	303	2.3	0.015	0.03	2.3	0.23
				2	14.023	0.078	293	303	5.5	0.015	0.01	5.5	0.55
				3	39.270	0.62	293	303	9.2	0.015	0.01	9.2	0.92
4	350	60	0.5	1	5.769	0.007	293	303	2.8	0.024	0.03	2.8	0.28
				2	36.157	0.27	293	303	7.1	0.024	0.01	7.1	0.71
				3	101.25	2.16	293	303	12	0.024	0.01	12	1.2
				3	101.25	2.16	293	323	12	0.013	0.01	12	1.2
				3	101.25	2.16	273	303	11	0.023	0.01	11	1.1

Table 7 Minimum force and force gradient limited by different noise sources.

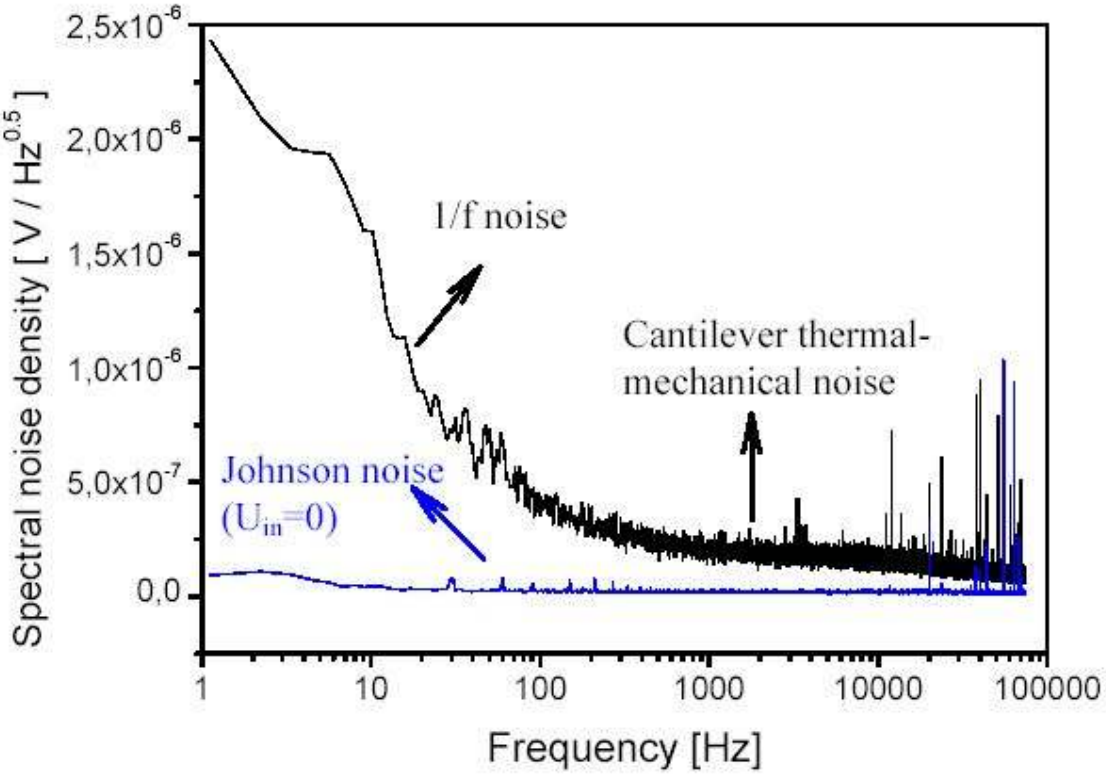

Figure 7.2 Noise spectrum from the cantilever.

Chapter 8
Fabrication process and applications of the cantilever-based sensors

In this chapter the scenario of the piezoresistive cantilever fabrication will be given. After that a few applications of the cantilever based sensors will be demonstrated.

8.1 Fabrication process

The microbeam fabrication process is based on a double side micromachining concept [109 , 110]. The developed sequence is conceived to enable fabrication of different micro-beam MEMS devices by simple modification of the lithography masks, with the general procedure remaining basically the same. $2-5$ Ωcm n-type, <100> silicon wafers were used as a starting material. After initial cleaning, surface oxidation and 100 nm LPCVD silicon nitride deposition, first photolithography was performed to define a mask dot in the future tip area (*Figure 8.1,* step1.) The diameter of this dot determines the future tip height. Furthermore, the sharp tip for AFM applications was formed by anisotropic under-etching of silicon in hot TMAH or KOH solution (*Figure 8.1*, step 2.) [57 , 111]. In a second lithography step (*Figure 8.1*, step 3.) p^+ diffusion windows were opened and afterwards heavily doped p^+ connections were created by high concentration boron diffusion, followed by high temperature drive-in. Silicon dioxide grown in this process protected against bare silicon surface exposed for the diffusion. In the subsequent processing step piezoresistors were formed by photolithography followed by moderate boron diffusion or alternatively, by 20 KeV boron implantation and thermal annealing (*Figure 8.1*, step 4.). Doping conditions as well as annealing

parameters were optimised to obtain high sensitivity of the piezoresistors. In the fourth lithography step contact holes were defined and etched in the oxide, to allow for connection of p+ diffusion regions with metal paths (*Figure 8.1*, step 5.). Then, a 1.0 μm Al film was deposited using magnetron sputtering where electrical connections and the microheater were defined in the next lithography and metal etching (*Figure 8.1*, step 6.) step. This microheater can also be formed by specially developed thin film high expansion coefficient Cu/Au/Ta-alloy (two times higher than Al). In this way a basic electrical structure was formed in silicon. The sixth lithography was performed at the backside of the wafers to define the membrane area. It has to be noted however, that this backside pattern was aligned to the front side structure already formed in silicon, to ensure required future cantilever shape and proper location of the piezoresistors. Then a window with corner compensation structures was plasma etched in silicon nitride and oxide films at the backside of the wafer while the front side was protected by photoresist layer. A deep, anisotropic silicon etching (bulk micromachining) was done in hot 30% KOH solution, to create 15 μm thick silicon membrane in the future beam area (*Figure 8.1*, step 7). In the most simple experimental set-up, the front side of the wafer with electronic structure already formed, was protected by placing the wafer in a chuck. Alternatively, we used boron doped silicon glass/refractory metal film double layer or KOH resistant polymer film for front side protection. The etching was stopped when the membrane thickness has reached the desired thickness of the cantilever. Finally, in the last step, the shape of the cantilever was cut in the membrane and the whole microprobe structure was formed by front side lithography, followed by silicon plasma etching with gas chopping technique [112] (*Figure 8.1*, step 8) and removing of photoresist in oxygen plasma (*Figure 8.1*, step 9). It has to be noted that after formation of the tip for AFM applications, a thickness of the photoresist has to be chosen carefully throughout the processing sequence, to protect the high tip during specific processes (e.g. front side silicon etching – step 8).

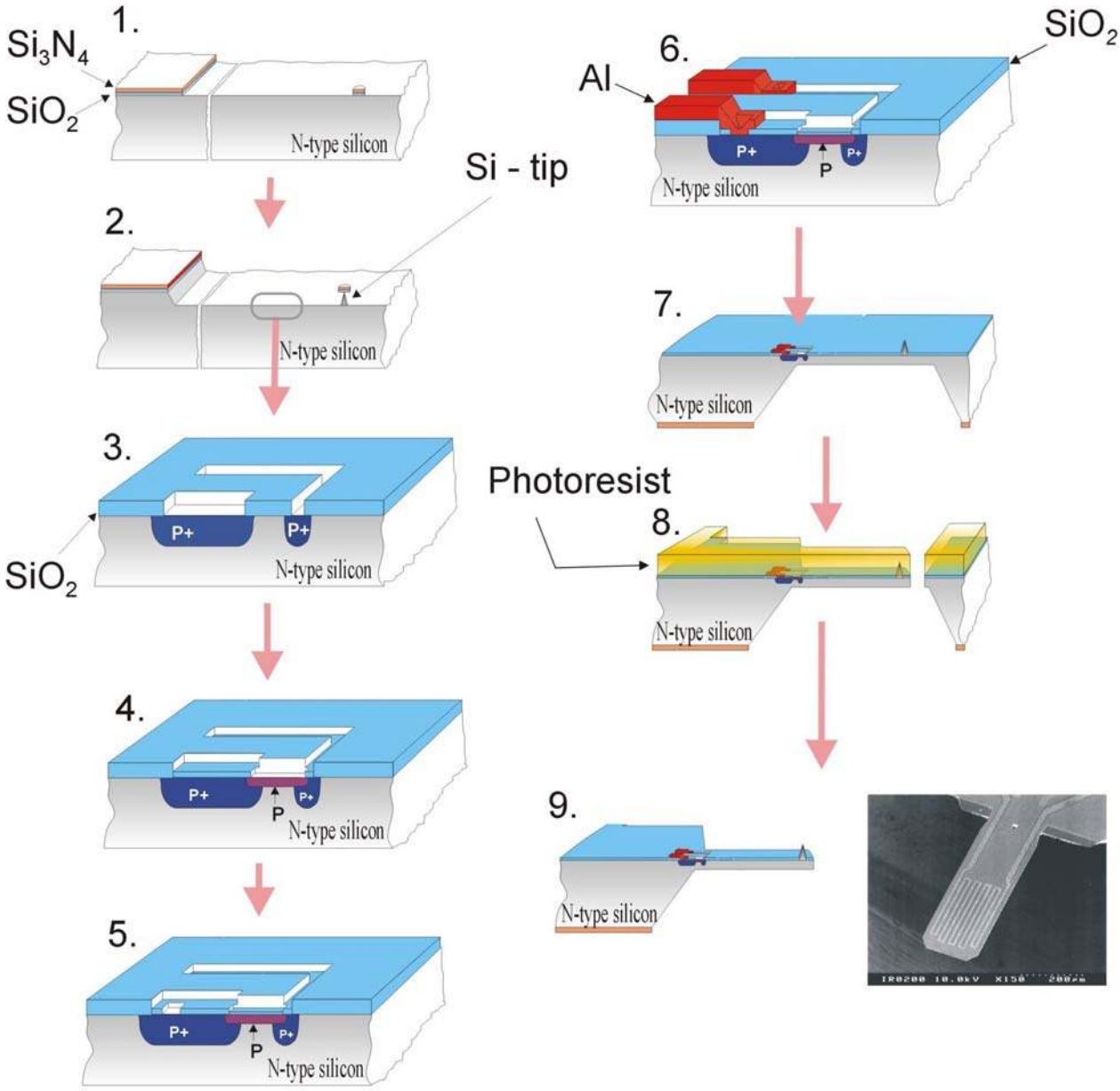

Figure 8.1 Fabrication flow chart of Si-micro-beam.

8.2 Cantilever beam with porous silicon element as a sensor

Recently, increasing effort has been spent into the development of cantilever-based chemical sensors [113]. As it was already discussed, the main motivation for the application of cantilevers as chemical sensors is based on the advantages, which are offered by their small size, high sensitivity and the possibility of integration of transducer, actuator and read-out unit on the same chip. For the application as a chemical sensor we developed a cantilever with porous silicon element *Figure 8.2a.* Porous silicon has a number of interesting features, which makes it a promising material for micro- and nanofabrication. The most important features are its large inner surface and high chemical activity.

The cantilever has been mounted on a piezoelectric actuator and placed in the chamber with controlled atmosphere. Resonance curves of the cantilever have been measured by sweeping the excitation frequency of the piezoelectric actuator and monitoring the resulting beam deflection. The deflection has been measured by use of a piezoresistive circuit located at the support of the cantilever and additionally by monitoring of a laser beam reflected from the device.

The resonance curves for relative humidity of 10% and 80% are shown in *Figure 8.2b.* It may be noted, that the quality factor of the beam (which is inversely proportional to the width of the resonance curve) first decreases with humidity then increases after reaching a minimum. This effect may be related to mechanical behavior of water inside the pores. For medium humidity relatively large water droplets can move inside pores dissipating mechanical energy. For low humidity the energy dissipation is smaller due to the small amount of water. For large humidity considerable filling of the pores hinders movement of water droplets inside pores and thus decreases energy dissipation.

A comparison of our results with those reported for cantilever coated with other materials (like gelatin, gold [61] or carbon nitride [114]) proves that the application of the porous silicon dramatically enhances the absorption efficiency. The most obvious explanation of this observation is a very high specific surface of this adsorbent. Applications of such a device include humidity and gas detection.

When characterizing a piezoresistive cantilever beam with a porous silicon element we has obtained a more complicated frequency spectrum with more than one resonance peak in the frequency range up to 100 KHz, in comparison with the simple cantilever beam. This behaviour can be explained with the fact that for the given cantilever geometry the fundamental and higher eigenmodes for both transversal (bending) and share (torsion) modes fall in the working frequency range. For our method of piezoresistive detection of the cantilever bending it was not possible for us to identify the various peaks with regard to their oscillation modes. In order to identify the experimental peaks a FEM simulation were used. From the obtained results it was possible to explain the experiment and identify very correctly all peaks in the frequency spectrum range with the corresponding oscillation modes (*Figure 8.2b*) [119].

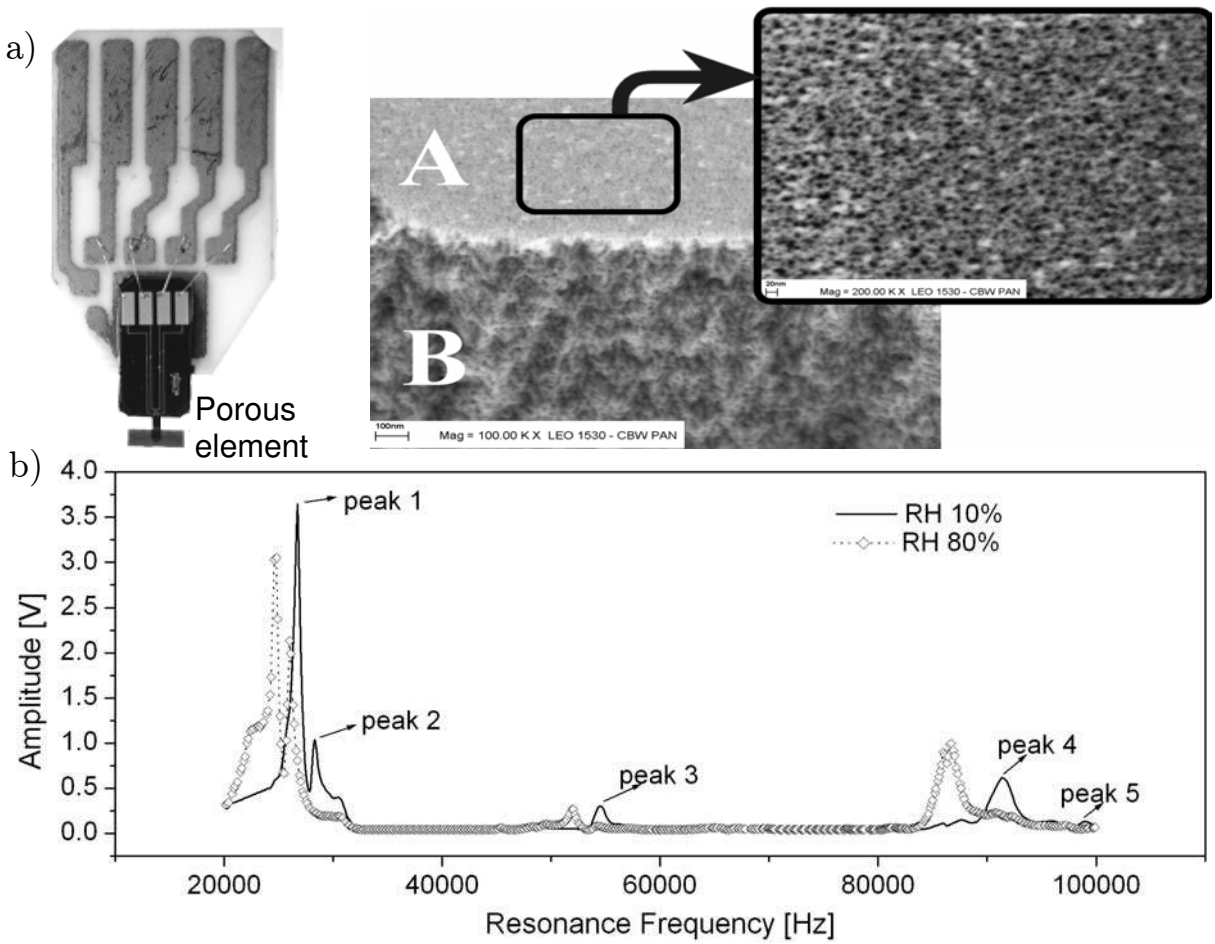

Figure 8.2 a) The T-shaped cantilever with a porous silicon element and the SEM view of a porous silicon layer (A - surface, B - cross-section) b) Frequency spectrum of a cantilever beam with porous silicon element for different humidity (10% and 80%).

8.3 Cantilever beam for high speed AFM in higher eigenmodes

In this section we will present a micromachined AFM cantilever with an integrated piezoresistive sensor and thermal bimorph actuator for high-speed tapping-mode AFM phase-imaging in higher eigenmodes. Tapping Mode Atomic Force Microscopy (TM-AFM) allows imaging with nanometer-scale resolution, where the tip strikes the surface with negligible force. This technique is a promising candidate in non-contact and damage free sub 50nm Critical Dimension (CD) measurement applications. In TM-AFM [19] the cantilever is excited to oscillate close to its resonance. The topography information is collected from the phase lag between vibration excitation and response of the cantilever deflection sensor. This phase lag is related to the energy dissipated in the tip-sample interaction. The cantilever with an integrated piezoresistive sensor and thermal bimorph actuator offers two advantages for such a kind of measurements. First, cantilever probes based on the piezoresistive sensing principle, which was discussed in Chapter 4, provide a simple and convenient technique enabling easy access to novel applications of force microscopy. Second, due to the bimorph actuator, described in Chapter 6, a high deflection can be achieved.

Figure 8.3 shows a piezoresistive cantilever with a thermal bimorph actuator and experimentally obtained piezoresistor response vs. drive frequency of the bimorph actuator for a free cantilever. It was possible to obtain the fundamental (f_0=19kHz) and the next 3 natural modes (f_1=162kHz, f_2=348kHz, and f_3=716kHz).

In our set-up the cantilever is driven by thermal actuation at its resonant frequency (f_{res}) by an AC current with frequency ($f_{res}/2$), while applying a DC current provides a z-axis actuation. The magnitude of the DC current determinates the deflection of the cantilever, controlled by the PID feedback loop - *Figure 8.4a.* The DC biasing causes a shift in the resonance frequency - *Figure 8.4b*. This can be explained by the fact that due to the increase of the DC bias the temperature of the cantilever will increase and this will increase the compressive stress. The total AC driving power is below 1μW [120]. In this manner, a stable actuator and a soft cantilever for probing of the surface of the sample are provided.

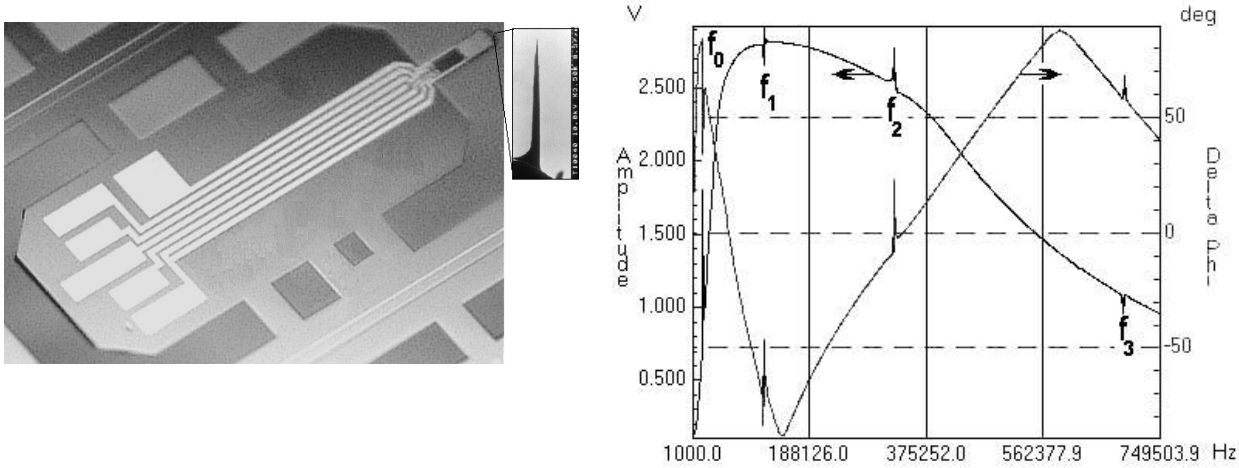

Figure 8.3 Micromachined TM-AFM probe with integrated bimorph actuator, piezoresistive deflection sensor and Si-tip; Piezoresistor response vs. drive frequency of the bimorph actuator for a free cantilever.

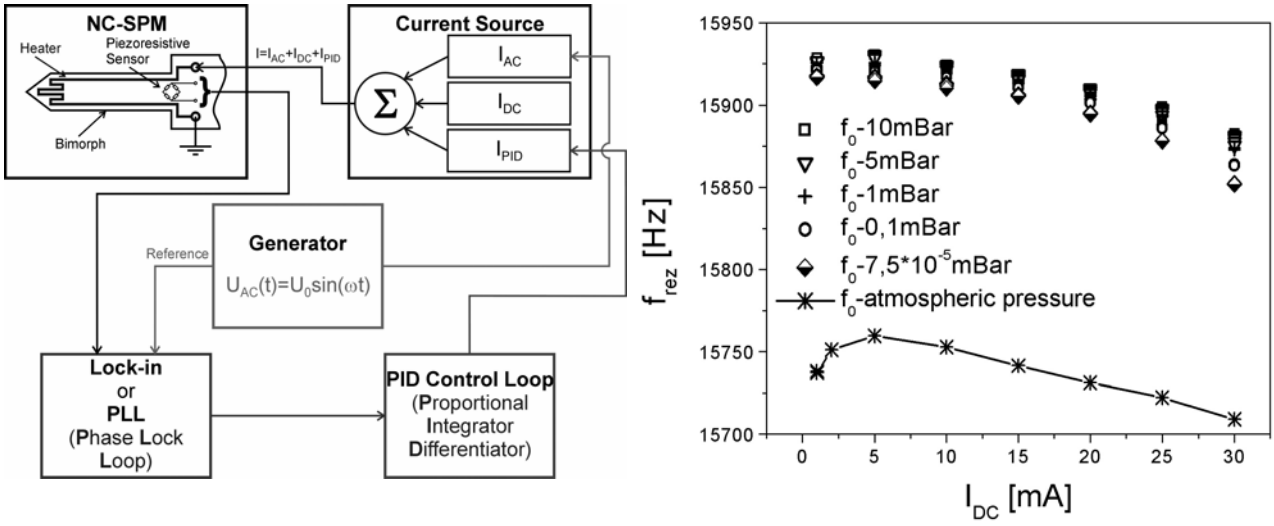

Figure 8.4 a) Schematic diagram of the experimental set-up and PLL PID feedback electronics b) Resonance frequency shift (first mode) vs. actuator DC bias for different pressures.

Employing TM-AFM in higher eigenmodes we found, that the most sensitive mode of flexural vibration for an AFM cantilever is the first mode. However, the high-order vibration modes are more sensitive than the first mode when the contact stiffness is greater. These results are compatible with the theoretical results obtained by [121]. *Figure 8.5a* shows the measured topography of a chromium pattern on quartz with deposited a 5nm Pt film recorded with 5Hz and 10Hz. The height contrast between the

top of the Cr pattern (bright) and the quartz substrate between the features (dark) is 40nm, as expected. The TM-AFM image reveals a cluster structure of the deposited Pt onto the Cr-pattern. From this observation one can conclude, that the Cr pattern is perfectly reproduced and in particular, some residual resist is present on the patterns. The vibration amplitude was 10nm, which means that the tip provides a complete approach-contact retraction cycle during each period of oscillation. *Figure 8.5b* depicts the tapping mode image of a Cr grating with a period of 1μm. The Cr-patterns are 40nm high. The image was taken at 10Hz scan speed at the mechanical resonance frequency 716kHz. Images presented in *Figure 8.5* were obtained employing the phase signal for distance regulation.

The magnitude of cross coupling from actuator to sensor is an essential issue, since they are closely spaced due to their integration on the cantilever. We have evaluated the signal cross coupling from the thermal-actuator input to the piesoresistive sensor output.

As was discussed in chapter 6.6, the heat used for actuation can induce a temperature gradient at the location of the Wheatstone bridge sensor and can lead to a large offset or signal drift of the sensor output. The sensor signal was measured as a function of the frequency at which the thermal-actuator was driven using a lock-in technique. At DC-current level, the amount of cross coupling for a given actuator power is about 3nV/mA. This relatively low cross-coupling shows that the full Wheatstone bridge configuration provides a good temperature compensation and confirms the theoretical results obtained in chapter 6.6.

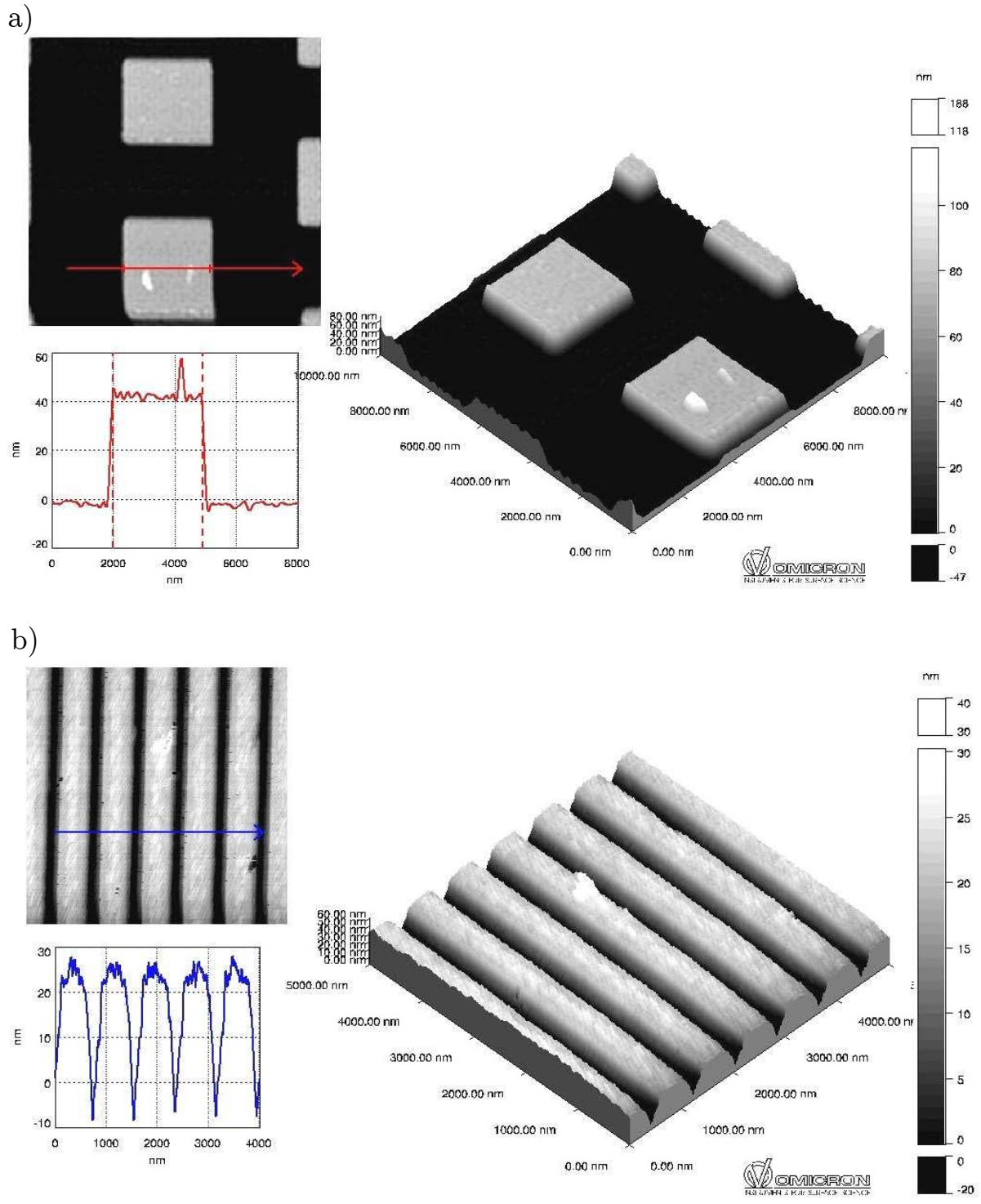

Figure 8.5 a) Typical image of profile measurements obtained with 5 Hz for Cr features of optical mask b) CD measurements with 10 Hz done on Cr features.

8.4 Piezoresistive cantilever as a tool for maskless lithography

In the previous section it was discussed the imaging technique with the piezoresistive cantilever with an integrated actuator. In this section will be demonstrated the possibility of the bimorph actuated cantilever to be used as a tool for high resolution nanolitography.

The Proximal Probe Nano-Lithography System (P2NLS) is a high resolution patterning technique that uses a sharp tip in close proximity to a sample to pattern nanometer-scale features. The P2NLS may be used as a nanolithography tool for high resolution patterning of various materials where the field emission electrons emitted from a sharp tip are used to induce localized chemical changes or ablation in an organic polymer resist. P2NLS has a wide exposure latitude and high linearity in the dot-pixel-writing mode, and negligible proximity effects.

For the sample preparation thin PMMA and calixaren [122] films on sputter deposed Au film on a silicon substrate are used. A micromachined AFM cantilever with an integrated silicon probe tip acts as a field emitter source of electrons. During the exposure process the field emission current from the tip was kept constant by a current feedback regulator. Moreover, to eliminate the problems of tip wear the atomic force microscopy principle based on the pizoresistive cantilever also was used for the distance control.

Feature sizes below 25nm (see *Figure 8.6*) have been patterned in 100nm-thick organic resist. It can be seen that by patterning lines with P2NLS all individual features are ablative formed.

In addition, in order to improve the throughput, this lithography technique can be easily adapted to multiple-tip arrays [123] where each cantilever has an integrated bimorph actuator to adjust the probe height. In such way, the P2NLS can provide an attractive alternative for high-resolution lithography because of its ability to maintain exact CD and alignment control.

It was demonstrated that the atomic force microscope AFM operating in air may be used to pattern narrow features in resists or organic monolayers in a noncontact (maximum 100nm to the surface) lithography mode. The advanced features of P2NLS make it an ideal for sub 50nm lithography. Also, for many basic research applications,

the capabilities of P2NLS make it the preferred instrument, as shown by the fact that Proximal Probe Nano-Lithography can be used for the fabrication of a wide variety of nano-devices. Research areas include: quantum structures, optical structures, electro-mechanical structures, such as M(N)EMS devices and ultra-small sensor fabrication. The noncontact mode AFM configuration allows extending the tip lifetime while retaining the high resolution and fast imaging capabilities of the AFM for alignment registration.

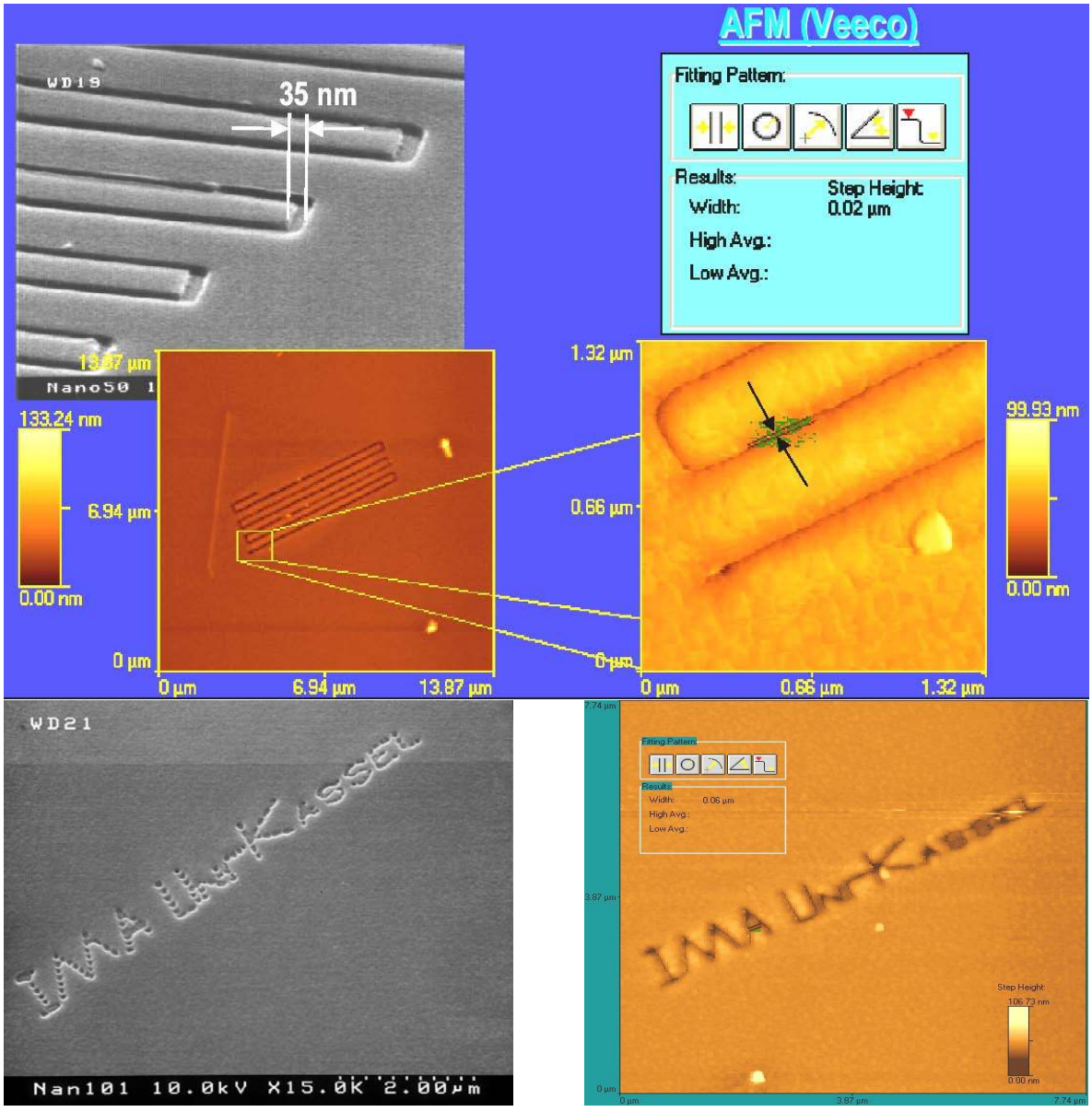

Figure 8.6 SEM and AFM micrographs of features written by the Proximal Probe Nano-Lithography System in a 50nm thick PMMA.

Conclusions

The major goal of the work described in this thesis has been to develop very sensitive force gradient sensors, which allow mapping of the sample surface topology at high speed. This problem involves two tasks. First, the integrated deflection sensor has to fulfil the requirements for high z-resolution. The second task to be addressed is an integrated actuating mechanism for high-speed imaging.
In the context of the aims listed above, the following key results can be summarised.

i) The piezoresistive deflection sensor has been chosen in order to replace the external laser detecting techniques and the resulting limits of the cantilever operation. Theoretical studies of the piezoresistive effect both in n- and in p-type bulk silicon have been conducted using the kp theory to obtain the band structure near the band edges with and without stress. As a result it was possible to obtain the piezoresisitive coefficients, which are in good agreement with published experimental data. Following the tendency of continuous improvement of the micro-fabrication technology, the model has been adapted for the calculation of the piezoresisitive coefficients in extremely thin surface ion-implanted piezoresistors (2D case). Combining the **kp** method with the model of the carrier localisation, considerable progress have been achieved in the understanding of the piezoresistive effect in case of 2D. It has been found that the values of the n-type piezoresistive coefficients decrease with the degree of electron localisation. Moreover, for p-type piezoresistivity, which has a more complicated origin, the predicted values of the piezoresistive coefficients are higher (approximately two times for a 9nm quantum well) in the case of localised holes, than in the bulk.

ii) Actuator integration into the cantilever is an essential issue in the development of AFM sensors for fast imaging. The idea of cantilevers with an integrated actuator,

based on the bimorph effect has been theoretically and experimentally investigated. The bimorph actuation efficiency depends on the thickness ratio of the layers. Moreover, the efficiency increases with decreasing of the cantilever thickness. Therefore, the cantilevers have to be thin in order to allow a sufficient bimorph actuation. In this manner DC actuations allow imaging of the sample topography.

iii) The dynamics of the vibrating cantilever (AC actuation) was studied in detail in order to ensure proper integration of the actuator into the cantilever. The existing detecting techniques for the dynamic imaging of the sample surface were discussed. It has been found that due to the bimorph DC actuation the resonance frequency shifts. For this reason a resonance frequency shift detection technique cannot be used for AFM imaging with this type of actuation. Thus the detection method chosen in this work was based on the amplitude modulation or phase shift detection.

iv) With respect to the cross-coupling between the bimorph actuator and the piezoresistive sensor, it has been found that the Wheatstone bridge configuration provides good enough temperature compensation. Observed coupling is based on electronic (capacitance) signal transfer from the actuator to the Wheatstone bridge.

v) The optimal cantilever design with respect to the force sensitivity was discussed, developed and presented. It has been demonstrated that for imaging in ambient conditions the force sensitivity is limited by the thermo-mechanical cantilever noise. Additional noise sources, connected with the piezoresistive detection (1/f and Johnson noises), are negligible.

vi) The proposed piezoresisive cantilevers with integrated bimorph actuators have been designed and fabricated considering the available theoretical knowledge.
Experimentally, the fabricated piezoresistive AFM cantilevers have been successfully employed in critical dimension (CD) measurements of lithographic chromium masks. Furthermore, the obtained experimental results with this cantilever show that utilizing TM-AFM in higher eigenmodes is a suitable technique for realizing high-speed topography imaging. The method we have used for a constant force imaging is based

on the constant phase lag at higher eigenmodes of the cantilever. At higher eigenmodes, we can increase the bandwidth of imaging. The use of higher eigenmodes allows obtaining topographic images with high sensitivity and improves the force resolution. Thus, for reliable CD measurement and pattern imaging at higher eigenmodes, the use of a phase locked loop (PLL) phase shift detector is very suitable techniques.

vii) It has been demonstrated that the fabricated cantilevers in the presented framework can be used in proximal probe lithography to pattern narrow (20nm) features in resists or organic monolayers in a noncontact (max. 100nm to the surface) lithography mode in air. Moreover, a new concept for high throughput based on array of bimorph actuated cantilevers was demonstrated [123].

Zusammenfassung

Das Hauptziel der in dieser Dissertation beschriebenen Arbeit war die Entwicklung hoch-empfindlicher Kraft-Gradienten-Sensoren, die es erlauben, die Oberflächen-topologie mit hoher Geschwindigkeit abzubilden. Dieses Problem besteht aus zwei Aufgaben. Erstens, der integrierte Auslenkungs-Sensor muß die Anforderungen für hohe z-Auflösung erfüllen. Die zweite Aufgabe besteht in der Entwicklung eines integrierten Aktuationsmechanismus für Hochgeschwindigkeits- Abbildungen.
Im Rahmen der oben aufgelisteten Ziele können die folgenden Schlüsselresultate zusammengefasst werden.

i) Der piezoresistive Auslenkungssensor wurde ausgewählt, um die externe Laser-Detektions-Technik und die damit einhergehenden Grenzen des Cantilever-Betriebs zu ersetzen. Theoretische Untersuchungen des piezoresistiven Effekts sowohl in n- als auch in p-dotiertem Volumen-Silizium wurden mittels der kp-Theorie durchgeführt, um die Bandstruktur in der Umgebung der Bandkanten mit und ohne mechanische Spannungen zu erhalten. Als Ergebnis wurden die piezoresistiven Koeffizienten in guter Übereinstimmung mit publizierten experimentellen Daten erhalten. Entsprechend dem Trend der kontinuierlichen Verbesserung der Mikrofabrikations-Technologie wurde das Modell für die Berechnung der piezoresistiven Koeffizienten in extrem dünnen oberflächen-ionenimplantierten Piezoresistoren angepasst (2D-Fall). Durch Kombination der kp-Methode mit dem Modell der Ladungsträgerlokalisation wurde ein beträchtlicher Fortschritt im Verständnis des piezoresistiven Effekts im zweidimensionalen Fall erzielt. Es wurde gefunden, dass die Werte der piezoresistiven Koeffizienten für n-dotiertes Silizium mit dem Grad der Elektronenlokalisation fallen. Darüber hinaus sind die vorhergesagten piezoresitiven Koeffizienten für p-dotiertes

Silizium, die eine kompliziertere Ursache haben, im Fall lokalisierter Löcher höher (etwa Faktor 2 für einen 9nm Quantentrog) als für das Volumen.

ii) Die Integration des Aktuators in den Cantilever ist ein wesentlicher Punkt in der Entwicklung von AFM-Sensoren für schnelle Abbildungen. Das Konzept von Cantilevern mit integrierten auf dem Bimorph-Effekt basierenden Aktuatoren wurde theoretisch und experimentell untersucht. Die Effizienz des Bimorph-Aktuators hängt von dem Dickenverhältnis der Schichten ab. Darüber hinaus nimmt die Effizienz mit abnehmender Cantileverdicke zu. Deswegen müssen die Cantilever dünn sein, um eine ausreichende Aktuation nach dem Bimorph-Prinzip zu ermöglichen. In dieser Weise erlauben DC-Aktuationen die Abbildung der Probentopologie.

iii) Die Dynamik der Cantilevervibration (AC-Aktuation) wurde detailliert untersucht, um die geeignete Integration des Aktuators in den Cantilever sicherzustellen. Die existierenden Detektions-Techniken für dynamisches Abbilden der Probenoberfläche wurden diskutiert. Es wurde herausgefunden, dass wegen der bimorphen DC-Aktuation, sich die Resonanzfrequenz verschiebt. Aus diesem Grund kann eine Detektion der Verschiebung der Resonanzfrequenz nicht zur AFM- Abbildung mit dieser Art von Aktuation verwendet werden. Deshalb basiert die Detektionsmethode, die in dieser Arbeit gewählt wurde, auf dem Prinzip der Amplitudenmodulation oder der Phasenverschiebungs-Detektion.

iv) Im Hinblick auf ein Übersprechen zwischen der bimorphen Aktuation und dem piezoresistiven Sensor wurde herausgefunden, dass eine Wheatstone-Brückenkonfiguration eine ausreichende Temperaturkompensation bietet. Das beobachtete Übersprechen stammt aus der elektronischen (kapazitiven) Signalkopplung vom Aktuator zur Wheatstone-Brücke.

v) Der optimale Cantilever-Aufbau im Hinblick auf die Kraftempfindlichkeit wurde diskutiert, entwickelt und präsentiert. Es wurde gezeigt, dass für Abbildungen in normaler Umgebung die Kraftempfindlichkeit durch das thermo-mechanische

Cantileverrauschen begrenzt wird. Weitere Rauschquellen, die mit der piezoresistiven Detektion (1/f- und Johnson-Rauschen) sind vernachlässigbar.

vi) Die vorgeschlagenen piezoresistiven Cantilever mit integrierten bimorphen Aktuatoren wurden unter Berücksichtigung der theoretischen Erkenntnisse entworfen und hergestellt.
Die hergestellten piezoresistiven AFM-Cantilever wurden experimentell erfolgreich bei der Messung kritischer Dimensionen (CD - "critical dimensions") von lithographischen Chrommasken eingesetzt. Weiterhin zeigen die mit diesen Cantilevern erzielten experimentellen Resultate, dass der Einsatz von TM-AFM in höheren Eigenmoden eine geeignete Technik für die Verwirklichung von Hochgeschwindigkeits-Topographieabbildungen ist. Die von uns verwendete Methode für eine Abbildung bei konstanter Kraft basiert auf der konstanten Phasenverschiebung bei höheren Eigenmoden des Cantilevers. Die Bandbreite der Abbildung kann bei höheren Eigenmoden erhöht werden. Die Verwendung höherer Eigenmoden erlaubt es, Topographieabbildungen mit hoher Empfindlichkeit zu erhalten und erhöht die Kraftauflösung. Daher ist die Verwendung eines Phase-Locked-Loop (PLL) Phasenverschiebungs-Detektors für die zuverlässige Messung kritischer Dimensionen ("CD measurements") und Abbildung bei höheren Eigenmoden eine geeignete Technik.

vii) Es wurde gezeigt, dass die im Rahmen dieser Arbeit hergestellten Cantilever für die "proximal probe" - Lithographie zur Strukturierung von schmalen (20nm) Strukturen in Photoresist oder organischen Monolagen in einem berührungslosen (maximal 100nm Abstand zur Oberfläche) Lithographiemodus an normaler Luft verwendet werden können. Darüberhinaus wurde ein neues auf einem Array von bimorph aktuierten Cantilevern basierendes Konzept für hohen Durchsatz vorgestellt [123].

Appendix

In the table below are presented the values of the silicon and aluminium properties used in this work.

Material Property	Value	Unit	Ref.
SILICON			
Crystal structure	diamond		[115]
Lattice constant	5.43	Å	[116]
Density	2300	kg/m^3	[116]
Compliance coefficients			[115]
s_{11}	0.768	$10^{-11}\ m^2/N$	
s_{12}	-0.214	$10^{-11}\ m^2/N$	
s_{44}	1.26	$10^{-11}\ m^2/N$	
Energy gap	1.17	eV	[115]
Phosphorus donor energy level	45	meV	
Boron acceptor energy level	45	meV	
Dielectric constant	11.9		
Valence band parameters			[116]
L	-5.53	$\hbar^2/(2m_e)$	
M	-3.64	$\hbar^2/(2m_e)$	
N	-8.62	$\hbar^2/(2m_e)$	
Spin-orbit splitting	44	meV	[116]
Deformation potential-VB			[32]
$a=(l+2m)/3$	-5	eV	
$b=(l-m)/3$	-1.92÷-4.84	eV	
$d=n/\sqrt{3}$	-5.1	eV	

Deformation potential-CB			[116]
dilatation Ξ_d	1.1	eV	
share Ξ_u	10.5	eV	
Conduction band parameter Ξ_m	71.58	$\hbar^2/(2m_e)$	[117]
Conduction band effective mass			[115]
transversal m_t	0.1905	m_e	
longitudinal m_l	0.9163	m_e	
Piezoresistive coefficients n-type			[115]
π_{11}	-102.2	$10^{-11}\ m^2/N$	
π_{12}	53.4	$10^{-11}\ m^2/N$	
π_{44}	-13.6	$10^{-11}\ m^2/N$	
Piezoresistive coefficients p-type			[115]
π_{11}	6.6	$10^{-11}\ m^2/N$	
π_{12}	-1.1	$10^{-11}\ m^2/N$	
π_{44}	138.1	$10^{-11}\ m^2/N$	
Coefficient of thermal expansion at 300K	2.616	$10^{-6}K^{-1}$	[115]
Thermal Conductivity at 300K	156	$Wm^{-1}K^{-1}$	[115]
Specific heat at 300K	713	$J/(kgK)$	[115]
Poisson's ratio	0.27		
Young's modulus [110]			[118]
$Y(T) = 0.1681873\,T^4$-449.0539 T^3+464875.9 T^2 $-2.319830\times10^8 T + 2.061456\times10^{11}$			
ALUMINUM			
Density	2694	kg/m^3	
Coefficient of thermal expansion at 300K	23.3	$10^{-6}K^{-1}$	
Thermal Conductivity at 300K	236	$Wm^{-1}K^{-1}$	
Specific heat at 300K	901	$J/(kgK)$	
Poisson's ratio	0.33		
Young's modulus	70	GPa	

Table 8 Material parameters employed in this work.

References

[1] R. Feynman, Engineering and Science 23 22 (1960)

[2] G. Binnig, C.F. Quate, Ch. Geber, Atomic Force Microscope, Phys. Rev. Letters, Vol. 56, No 9, 1986 p 930

[3] Binnig, G. and Rohrer, H. (1982). Scanning tunneling microscopy *Helvetica Physica Acta* 55, 726-735.

[4] G. Meyer and N.M. Amer, Appl. Phys. Lett. 53, p.1045, (1988).

[5] M. Tortonese, H. Yamada, R.C. Barett, C.F. Quate, IEEE, 91CH2817-5, p. 448, (1991); M.Tortonese, R. C. Barrett, and C. F. Quate, Appl. Phys. Lett. 62, 834 (1993)

[6] A. N. Cleland and M. L. Roukes, Appl. Phys. Lett. 69 (18), (1996), p. 2653

[7] P. Mohanty, D. A. Harrington, M. L. Roukes, Physica B 284-288 (2000) p.2143

[8] T. Thundat, P.L.Oden, and R J Warmack, Proceedings of the Third International Symposium on Microstructures and Microfabricated Systems, pp. 179-189, Pennington, NJ, (1997).

[9] Gil U Lee, Linda A. Chrisey, and Richard J. Colton, *Science* 266, p.771, (1994).

[10] T.Powers, G.Daubresse and H.F.Noller, J. Mol. Biol. 232, p.362, (1993).

[11] T. D. Stowe, K. Yasumura, T. W. Kenny, D. Botkin, K. Wago, and D. Rugar, Appl. Phys. Lett. 71(2), p. 288, (1997).

[12] H.B. Callen and T.A. Welton, Phys. Rev. 83 (1951) 34.

[13] R.F. Greene and H.B. Callen, Phys. Rev. 83 (1951) 1231.

[14] H.B. Callen and R.F. Greene, Phys. Rev. 86 (1952) 702.

[15] R.F. Greene and H.B. Callen, Phys. Rev. 88 (1952) 1387.

[16] Kevin Y. Yasumura, Timothy D. Stowe, Eugene M. Chow, Timothy Pfafman, Thomas W. Kenny, Barry C. Stipe and Daniel Rugar, Journal of Microelectromechanical Systems 9 (1), p.117, (2000)

[17] T.R. Albrecht, P. Grütter, D. Horne, and D. Rugar. Frequency modulation detection using high-Q cantilevers for enhanced force microscope sensitivity. *J. Appl. Phys.*, 69:668, (1991).

[18] J.A. Harley and T.W. Kenny, Applied Physics Letters 75 (2), p. 289, (1999).

[19] Q. Zhong, D. Imniss, K. Kjoller, and V. B. Elings, Surf. Sci. 290, L688, (1993).

[20] S. H. Leuba, G. Yang, C. Robert, B. Samori, K. van Holde, J. Zlatanova, and C. Bustamante, Proc. Natl. Acad. Sci. USA **91**, p.11621, (1994).

[21] K. E. Petersen, IBM J. Res. Develop.,vol. 24, p.631, (1980).
[22] T.Itoh, T. Ohashi, and T. Suga, J.V.Sci. Technol. B 14(3), p.1577, (1996).
[23] S. Timoshenko, "Analysis of bi-metal thermosensors", J.Opt. Soc Amer. 11, p.233, (1925)
[24] J.F. Nye, "Physical Properties of Crystals", Oxford Science, N.Y., (1985)
[25] D.R.Lovett, "Tensor properties of crystals", IOP Publishing, Philadelphia, (1994).
[26] L. D. Landau and E. M. Lifshitz, "*Quantum Mechanics*", Pergamon Press, (1976).
[27] S.G. Lekhnitskii, "*Theory of Elasticity of an Anisotropic Body*", MIR, Moscow, (1981).
[28] C.S. Smith, Phys. Rev. 94, 42 (1954).
[29] L. H. Thomas, "The Kinematics of an Electron with an Axis", Phil. Mag. 3, p.1, (1927).
[30] J. D. Jackson, "*Classical Electrodynamics*" Third Edition, Wiley, New York, (1998).
[31] E.Wigner, "Group Theory and its Application to the Quantum Mechanics of Atomic Spectra", Academic, New York, (1959).
[32] E.L. Ivchenko and G.E. Pikus, "Superlattices and Other Heterostructures. Symmetry and Optical Phenomena", Springer, Berlin, (1997).
[33] S. M. Sze, "*Physics of semiconductor devices*", 2nd ed., John Willey & Sons, ISBN 0-471-05661-8, (1981).
[34] C. Herring and E. Vogt, Phys. Rev. 101, 944 (1956).
[35] J.C. Hensel, Phys. Rev. 138, p.A225, (1965).
[36] G. Bir and G. Pikus, "*Symmetry and Strain-Induced Effects in Semiconductors*", Wiley, New York, (1974).
[37] K.V. Shalimova, "Physics of semiconductor", Moscow Energoatomizdat, (1985).
[38] A. I. Anselm, Introduction to Semiconductor Theory, Mir-Moscow, Prentice-Hall, Englewood Cli's, NJ, (1981).
[39] J. E. Dijstra, and W. Th. Wenckebach, Journal of Appl. Phys. 81, p. 1259, (1997).
[40] P. Kleimann, B. Semmache, M. Le Berre, D. Brbier, Phys. Rev. B 57 (15), p.8966, (1998).
[41] Tzv.Ivanov, T.Gotszalk, T.Sulzbach and I.W.Rangelow, Ultramicroscopy 97 (1-4), p. 377, (2003).
[42] H. M. van Driel, "Optical effective mass of high density carriers in silicon", Appl. Phys. Lett. 44, p.617, (1984).
[43] Y. Kanda, "A graphical representation of the piezoresistance coefficients in silicon," *IEEE Trans Electron Devices* 29 (1), p.64, (1982).
[44] C. Kittel and H. Kroemer, *Thermal Physics*, 2nd Edition, Freeman, New York, (1980).
[45] John P. McKelvey, "Solid State and Semiconductor Physics", Robert E. Krieger Publishing Company, Malabar, Florida, (1982).
[46] Karl W. Böer, "Survey of Semiconductor Physics", Van Nostrand Reinhold, New York, (1990).
[47] Peter Y. Yu, Manuel Cardona, "Fundamentals Of Semiconductors", Springer-Verlag, Berlin, (1996).

[48] C. Erginsoy, "Neutral Impurity Scattering in Semiconductors", Physical Review 79, p.1013.
[49] N. Sclar, "Neutral Impurity Scattering in Semiconductors", Physical Review104 (6), p.1559, (1956).
[50] Gerald Bastard, "Wave Mechanics Applied to Semiconductor Heterostructures", Halsted Pr, (1991).
[51] I.Yamada, J. Matsuo, Mat. Sci. Semicond. Proc. 1, p.27, (1998).
[52] V. N. Popok, S. V. Prasalovich, M. Samuelsson, and E. E. B. Campbell, Review of Scientific Instruments 73 (12), p.4283, (2002).
[53] http://www.ansys.com
[54] Jr.W.Weaver , S.P.Timoshenko and D.H.Young, *Vibration Problems in Engineering,* John Wiley & Sons, Inc., New York, Fifth Edition, (1990).
[55] E. Liu, B. Blanpain and J. P. Celis, Wear 192 (1-2), pp. 141-150, (1996).
[56] R. Linnemann, T. Gotszalk, L. Hadjiiski, I.W. Rangelow, Thin Solid Films 264, p.159. (1995).
[57] R. Linnemann, T. Gotszalk, I.W. Rangelow, P. Dumania and E. Oesterschulze, J. Vac. Sci. Technol. B 14, p.856, (1996).
[58] F. J. Von Preissig, J. Appl. Phys. 66, 4262 (1989).
[59] G. C. Stoney, Proc. R. Soc. London, Ser. A 32, 172 (1909).
[60] Y.Martin, C.C. Williams and H.K. Wickramasinghe, J.Appl.Phys. 61, p.4723, (1987).
[61] G. Y. Chen, T. Thundat, E. A. Wachter, and R. J. Warmack, J. Appl. Phys. 77 (8), pp.3618, (1995).
[62] Suman Cherian and Thomas Thundat, Appl. Phys. Lett., Vol. 80, No. 12, pp.2219, (2002).
[63] Franz-Josef Elmer and Markus Dreier, J. Appl. Phys. 81 (12), pp.7709, (1997).
[64] R. Garcia, A. San Paulo, Ultramicroscopy, Vol: 82 (1-4), pp. 79-83, (2000).
[65] Joseph A. Turner, Sigrun Hirsekorn, Ute Rabe and Walter Arnold, J. Appl. Phys. 82 (3), pp.966, (1997).
[66] S. Bouwstra and B. Geijselaers, ″On the resonance frequencies of microbridges″*Dig. of Technical Papers, 6th Int. Conf. of Solid-State Sensors and Actuators*, San Francisco, CA, June 24-27, p.538, (1991).
[67] J. A. Harley, E. M. Chow and T. W. Kenny, Proceedings of the 1998 ASME International Mechanical Engineering Congress and Exposition, p. 247, Anaheim, CA, (1998).
[68] Harley, J. A., Stowe, T. D., and Kenny, T. W., "Piezoresistive Cantilevers with Femtonewton Force Resolution," *The 10th international conference on solid-state sensors and actuators*, vol. 2, p.1628, Sendai, Japan, (1999).
[69] M. V. Salapaka, H. S. Bergh, J. Lai, A. Majumdar, and E. McFarland, J. Appl. Phys. 81 (6), pp.2480, (1997).
[70] M. L. Boas,″Mathematical Methods in the Physical Sciences", Sec. Edition Wiley, (1983).
[71] T. Sulchek, R. Hsieh, J. D. Adams, G. G. Yaralioglu, S. C. Minne, C. F. Quate, J. P. Cleveland, A. Atalar, and D. M. Adderton, Appl. Phys. Lett. 76, pp.1473, (2000).

[72] T. Sulchek, G. G. Yaralioglu, C. F. Quate, and S. C. Minne, Rev. Sci. Instrum 73 (8), pp.2928 (2002).
[73] R. W. Stark, T. Drobek, and W. M. Heckl, Appl. Phys. Lett. 74, p.3296 (1999).
[74] D.A. Anderson, J.C. Tannehill and R.H. Pletcher, *Computational Fluid Mechanics and Heat Transfer*, McGraw-Hill, (1984).
[75] M. Moldover, J. Mehl, and M. Greenspan, *Journal of the Acoustical Society of America* 79, p.253, (1986).
[76] A. Boukabache, P. Pons, G. Blasquez, Z. Dibi, Sensors and Actuators 84, p.292, (2000).
[77] Brigham, E. Oren, *The Fast Fourier Transform and Its Applications*, Englewood Cliffs, NJ: Prentice-Hall, Inc., (1988).
[78] C. Kittel, Elementary Statistical Physics , John Wiley & Sons, New York, (1958).
[79] H. Nyquist, Phys. Rev. 32, 110 (1928).
[80] L. D. Landau and E. M. Lifshitz, "*Statistical Physics*", (Pergamon Press, 1980).
[81] P.R. Saulson, Phys. Rev. D 42, p.2437, (1990).
[82] F. R. Blom, S. Bouwstra, M. Elwenspoek, and J. H. J. Fluitman, J. Vac. Sci. Technol. B 10, 19 (1992).
[83] A. Passian; R.J. Warmack, A. Wig, R.H. Farahi, F. Meriaudeau, T.L. Ferrell, T. Thundat, Ultramicroscopy 97 (1-4), p.401, (2003).
[84] Franz-Josef Elmer and Markus Dreier, J. Appl. Phys. 81 (12), p.7709, (1997).
[85] Stefan Weigert, Markus Dreier and Martin Hegner, Appl. Phys. Lett. 69, p.2834, (1996).
[86] D. A. Walters, J. P. Cleveland, N. H. Thomson, P. K. Hansma, M. A. Wendman, G. Gurley, and V. Elings, Rev. Sci. Instrum. 67 (10), p.3583, (1996).
[87] M. Houmm˙ady˙, E. Farnault, Appl. Phys. A 66, p.S361, (1998).
[88] U. Rabe, K. Janser, and W. Arnold, Rev. Sci. Instrum. 67 (9), p.3281, (1996).
[89] S. Rast, C. Wattinger, U. Gysin and E. Meyer, Nanotechnology 11, 169, (2000).
[90] S.S. Lee, R. Kazinczi, J.R. Mollinger, M.J. Vellekoop and A. Bossche, Proceedings of SeSens , December 1, (2000).
[91] H. Hosaka, K. Itao, S. Kuroda, Sens. and Actuators A 49, p.87, (1995).
[92] C. Zener, Phys. Rev. 52, 230 (1937).
[93] C. Zener, Phys. Rev. 53, 90 (1938).
[94] A.N.Cleland, M.L.Roukes, J. Appl. Phys. 92 (5), p.2758, (2002).
[95] T. V. Roszhart, Tech. Dig. Solid-State Sens. Actuator Workshop, Hilton Head, SC, 13 (1990).
[96] R. Lifshitz, M. L. Roukes, Phys. Rev. B. 61, 5600 (2000).
[97] J. Yang, T. Ono, M. Esashi, J. Vac. Sci. Technol. B 19, p.551 (2001).
[98] M. Scherge, X. Li, J. A. Schaefer, *Tribology Letters*, 63 (4), p.215, (1999).
[99] Evoy, A. Olkhovets, D.W. Carr, L. Sekaric, J. M. Parpia, and H. G. Craighead, Appl.Phys Lett. 77, 2397 (2000).
[100] Jinling Yang, Takahito Ono, Masayoshi Esashi, Sensors and Actuators 82, p.102, (2000).

[101] J. B. Johnson, "Thermal agitation of electricity in conduction", *Physical Review* 32, p. 97, (1928).
[102] J. B. Johnson, "The Schottky Effect in Low Frequency Circuits", *Physical Review* 26, p.71, (1925).
[103] F.N. Hooge, Phys. Lett. A 29, p.139 (1969).
[104] P.H. Handel: "Nature of 1/f Phase Noise", Phys. Rev. Letters 34, p.1495, (1975).
[105] P.H. Handel: "Quantum Theory of 1/f Noise", Physics Letters 53A, p.438 (1975).
[106] A.van der Ziel: "Generalized Semiclassical quantum 1/f Noise Theory, I: Acceleration 1/f Noise in Semiconductors", J. Appl. Phys. 64, p.903, (1988).
[107] Q. Peng, A. N. Birbas, A. van der Ziel, A. D. van Rheenen, and K. Amberiadis, J. Appl. Phys. 64, p.907, (1988).
[108] Jonah A. Harley and Thomas W. Kenny, Journal of Microelectromechanical Systems 9 (2), p.226, (2000).
[109] I.W. Rangelow, S.Skocki, P. Dumania, Microelectronic Engineering 23, p.365, (1994).
[110] T. Gotszalk, R. Linnemann, and I. W. Rangelow, Thin Solid Films 264 (2), p.159, (1995).
[111] I.W. Rangelow, F. Shi, P. Hudek, T. Gotszalk, P. Grabiec and P. Dumania, SPIE 2879, p.56, (1996).
[112] I. W. Rangelow, J. Vac. Sci. Technol. A 21 (4), p.1, (2003).
[113] F.M. Battiston, J.-P. Ramseyer, H.P. Lang, M.K. Baller, Ch. Gerber, J.K. Gimzewski, E. Mayer, H.-J. Güntherord, Sens. Act. B 77, p.122, (2001)
[114] Zambow, C. Popov, M. F. Plass, W. Kulisch, T. Gotszalk, P. Grabiec, I.W. Rangelow, R. Kassing, , Advanced Materials 12 (9), p.6, (2000).
[115] R. Hull, "*Properties of Crystalline Silicon*", INSPEC, London, (1999).
[116] M.V.Fishetti, S.E.Laux, J. Appl. Phys. 80 (4), p.2234, (1996).
[117] J.M. Lysko, Proceedings of SPIE Volume 4516, Optoelectronic and Electronic Sensors IV, Jerzy Fraczek, Editor, p.1, (2001).
[118] N. Ono, K. Kitamura, K. Nakajima and Y. Shimanuki, Jpn. J. Appl. Phys. 39, p.368, (2000).
[119] K. Domanski, P. Grabiec, J. Marczewski, T. Gotszalk, Tz. Ivanov, N. Abedinov , I.W. Rangelow , J. Vac. Sci. Technology B21 (1), p.48, (2003).
[120] Tzv. Ivanov, T. Gotszalk, P. Grabiec, E. Tomerov, and I.W.Rangelow, Microelectronic Engineering, 67-68C p.550, (2003).
[121] Win-Jin Chang, Nanotechnology 13 (4), p.510, (2002).
[122] A. Tilke, M. Vogel, F. Simmel, A. Kriele, R. H. Blick, H. Lorenz, D. A. Wharam and J. P. Kotthaus, J. Vac. Sci. Technol. B 17 (4), p.1594, (1999).
[123] I.W.Rangelow, Tz. Ivanov, P.Hudek, O. Fortagne, "Device and Method for maskless AFM microlithography", PCT, WO 03/081171, 02.10.2003.

List of patents and publications

Patents:

1. I.W.Rangelow, **Tz. Ivanov**, St. Biehl, *"Verfahren zur Herstellung von mikrostrukturierten Bauelementen",* German Patent Applications, **DE 101 00 439**, 18.07.2002.

2. I.W.Rangelow, **Tz. Ivanov**, St. Biehl, "*Method for producing microstructured components*", PCT, **WO 02/053489**, 11.07.2002.

3. I.W.Rangelow, **Tz. Ivanov**, P.Hudek, O. Fortagne, "*Vorrichtung und Verfahren zur maskenlosen Mikrolithographie*", German Patent Applications, **DE 103 03 040 A1,** 02.10.2003.

4. I.W.Rangelow, **Tz. Ivanov**, P.Hudek, O. Fortagne, "Device and Method for maskless AFM microlithography", PCT, **WO 03/081171**, 02.10.2003.

Publications:

1. V.Donchev, **Tzv. Ivanov**, K.Germanova, "Electronic structure of AlAs/GaAs superlattices with an embedded centered GaAs quantum well", "*Advanced Electronic Technologies and Systems Based on Low-Dimensional quantum Devices*" (ed. M.Balkanski), NATO ASI Series, 3 High Technology - vol. 42, Kluwer Academic, Publishers, Dordrecht, p.51, (1997).

2. V. Donchev, **Tzv. Ivanov**, I. Ivanov, M. Angelov, and K. Germanova, "*High-temperature excitons in GaAs quantum wells embedded in AlAs/GaAs superlattices*", **Vacuum 58**, p.478, (2000).

3. V. Donchev, N. Shtinkov, K. Germanova, I. Ivanov, H. Brachkov, and **Tzv. Ivanov**, "*Photoluminescence lineshape analysis in quantum wells embedded in superlattices*", **Mat. Sci. Eng. C 15**, p.75, (2001).

4. N. Abedinov, P. Grabiec, T. Gotszalk, **Tz. Ivanov**, J. Voigt, and I. W. Rangelow "*Micromachined piezoresistive cantilever array with integrated resistive microheater for calorimetry and mass detection*", **J. Vac. Sci. Technology B19 (6)**, p.2884, (2001)

5. W. Barth, T. Debski, N. Abedinov, **Tz. Ivanov**, K. Torkar, K. Fritzenwallner, P. Grabiec, B. Volland, P. Hudek, I. Kostic, and I. W. Rangelow *"Evaluation and Fabrication of AFM array for ESA-Midas/Rosetta Space Mission",* **Microelectronic Engineering 57-58**, p.825, (2000).

6. **Tz. Ivanov**, I. W. Rangelow and S. Biehl "Field Emission Emitter Array with Self-Aligned Volcano Type Gate: Fabrication and Characterization", **J. Vac. Sci. Technology**, **B19 (6)**, p.2789, (2001).

7. B.E. Volland, **Tz. Ivanov** and I.W. Rangelow, *"Profile Simulation of Gas Chopping Based Etching Processes"*, **J. Vac. Sci. Technology B20 (6)**, p.3111, (2002).

8. K. Domanski, P. Grabiec, J. Marczewski, T. Gotszalk, **Tz. Ivanov**, N. Abedinov , I.W. Rangelow Fabrication and properties of piezoresistive cantilever beam with porous silicon element, **J. Vac. Sci. Technology B21 (1)**, p.48, (2003).

9. **Tzv. Ivanov**, T.Gotszalk, T.Sulzbach and I.W.Rangelow *"Quantum size aspects of the piezorestive effect in ultra thin piezoresistors",* **Ultramicroscopy 97 (1-4)**, p. 377*,* (2003).

10. **Tzv. Ivanov**, T. Gotszalk, T. Sulzbach, I. Chakarov, and I.W.Rangelow *"AFM cantilever with ultra thin transistor-channel piezoresistor: Quantum confinement"*, **Microelectronic Engineering, 67-68C**, p. 534, (2003).

11. **Tzv. Ivanov**, T. Gotszalk, P. Grabiec, E. Tomerov, and I.W.Rangelow *" Thermally driven micromechanical beam with piezoresistive deflection readout",* **Microelectronic Engineering, 67-68C**, p. 550, (2003).

12. Y. Sarov, I. Kostic, P. Hrkut, L. Matay, **Tz. Ivanov** and I. Rangelow *"Fabrication of diffraction gratings for microfluidic analysis",* **Bulgarian Journal of Physics 28-29**, (2003).

13. Y. Sarov, I. Kostic, R. Andok, **Tz. Ivanov** , I. W. Rangelow, "*Fabrication of large-area gratings by e-beam lithography and examples of their applications*", Proceedings of the 7th International Conference on Electron Beam Technologies (EBT), p.485, (2003).

14. N. Abedinov, C. Popov, Jh. Jordanov, **Tzv. Ivanov**, T. Gotszalk, P. Grabiec, D. Filenko, Yu. Shirshov and I. W. Rangelow, *"Chemical recognition based on micromachined silicon cantilever array",* **J. Vac. Sci. Technology B 21 (6)**, p.2931, (2003).

15. R. Pedrak, **Tzv. Ivanov**, K. Ivanova, T. Gotszalk, N.Abedinov, I. W. Rangelow, K. Edinger, E. Tomerov, T. Schenkel and P. Hudek , "*Micromachined AFM sensor with integrated piezoresistive sensor and thermal bimorph actuator for high-speed tapping-mode AFM and phase-imaging in higher eigenmodes*", **J. Vac. Sci. Technology B 21 (6)**, p.3102, (2003).

Curriculum vitae

Name	Tzvetan Ivanov
Date of Birth	9 March 1973, Russe, Bulgaria
Family Status	Married Wife: Katerina Ivanova Child: Denitsa Borisova (24.06.99)
Nationality	Bulgarian
09.1987-05.1991	High School in Russe, Bulgaria, profiling in Mathematics.
09.1991-07.1996	University of Sofia, Physics department.
07.1996	M.Sc. degree in Physics from the University of Sofia, profiling in Solid State Physics
01.2000	Institute of Technological Physics, University of Kassel

Acknowledgements

This thesis is based on work carried out at the Institute of Microstructure Technologies and Analytics (IMA) at the University of Kassel. I am grateful to the head of the institute, Prof. Dr. R. Kassing, for giving me the opportunity to work there and his steady support.

I would like to thank the Otto-Braun-Fonds for providing resources and funding for my research during this PhD.

There are many people to thank for their support and encouragement.

When I started working in the field of micromechanic, I had only very vague ideas about the point of it. It is to the credit of my supervisor, Dr. Iwo Rangelow, if this has changed. Thank you for many stimulating conversations. His ability to listen to my ideas and hypotheses is really admirable.

I would like to acknowledge Dr. K.Edinger from NaWoTec GmbH for the attendant technical discussions and support.

I am grateful to Dr. N.Abedinov and B.Volland for useful comments and discussions.

I would like to thank Dr. I.Chakalov from Silvaco Internation-Santa Clara for energetic discussions about the shallow junctions formation.

I thank very much to Dr. T.Schenkel from University of California, Berkeley for enthusiastic consultation and constructive critic.

In additional, I would like to thank Robert Pedrak and Dr. Teodor Gotszalk from Wroclaw University of Technology for the fruitful collaborative experimental work.

When doing research, many practical, time-consuming problems evolve, and only a rather small part of the time actually remains for scientific work. For this I would like to express my gratitude to A. Malkomes and M. Plaetzer.

Last but not least, I would like to thank my wife Katerina and my daughter Denitsa for their patience!

Declaration:

I confirm that I wrote this dissertation by myself and without illegal assistance. I have not used resources other than quoted. All materials taken verbally or logically from published or unpublished scripts are identified. No part of this work is related to another dissertation or habilitation.

Erklärung:

Hiermit versichere ich, dass ich die vorliegende Dissertation selbständig und ohne unerlaubte Hilfe angefertigt und andere als die in der Dissertation angegebenen Hilfsmittel nicht benutzt habe. Alle Stellen, die wörtlich oder sinngemäß aus veröffentlichten oder unveröffentlichten Schriften entnommen sind, habe ich als solche kenntlich gemacht. Kein Teil dieser Arbeit ist in einem anderen Promotions- oder Habilitationsverfahren verwandt worden.